UNIVERSITÀ DEGLI STUDI DI PADOVA

SCUOLA DI SCIENZE
Dipartimento di Geoscienze
Direttore Prof. Nicola Surian

TESI DI LAUREA MAGISTRALE IN ENVIRONMENTAL GEOLOGY AND EARTH DYNAMICS

ALKALI ACTIVATION OF LUNAR REGOLITH SIMULANTS: A SUSTAINABLE APPROACH FOR IN-SITU RESOURCE UTILIZATION

Relatore: Prof. Luca Valentini
Correlatore: Prof. Maria Chiara Dalconi

Laureando: Ahmad Goudarzi
Matricola: 2085107

ANNO ACCADEMICO 2023-2024

DEDICATION

I dedicate this thesis to my family, who have always supported me unconditionally and believed in my potential, providing me with the opportunities and encouragement to pursue my dreams.

To my spouse, Sara, whose love, patience, and understanding have been a constant source of strength and inspiration throughout this journey.

To my esteemed professors, Dr. Luca Valentini and Dr. Maria Chiara Dalconi, for their invaluable guidance, wisdom, and unwavering support throughout the research process.

To my friends, especially Anas Driouich, who have supported and encouraged me when I needed it most.

Finally, to anyone who has contributed to the completion of this work.

ABSTRACT

Space agencies worldwide are currently developing initiatives aimed at building human habitats on the Moon. Prioritizing environmental and economic sustainability is crucial for the successful establishment of Lunar settlements while meeting the unique requirements of the Moon. One method to achieve sustainable construction is by optimizing the utilization of raw materials obtained from the Moon for 3D printing.

The in-situ resource utilization (ISRU) concept envisages the use of raw materials available on the Moon (or other planetary bodies) for the local manufacture of processed materials or infrastructure. Based on the ISRU approach, Lunar regolith can be used as a locally sourced raw material to produce alkali-activated binders, which are suitable for the manufacture of building components. To facilitate the development of Lunar infrastructure and habitats, the alkali-activated regolith-based material must withstand the harsh Lunar environment, including significant temperature fluctuations, freeze-thaw cycles, high radiation levels, and frequent micrometeorite impacts. Furthermore, the material's rheological properties in the fresh state and the kinetics of setting and hardening are critical factors that must be compatible with its efficient extrusion during the initial phase of the 3D printing process.

The first part of this study involves using X-ray powder diffraction (XRPD) analysis and energy dispersive spectroscopy scanning electron microscopy (EDS-SEM) to identify the present mineral phases and elemental composition of the LMS-1D Lunar regolith simulant, as well as its reactivity in the alkali activation process. The next step is to use the design of experiments (DOE) approach to optimize the formulation of an alkali-activated regolith simulant-based material. This involves understanding the impact of critical factors, including the type and quantity of alkaline activator, the addition of reactive powders, and the curing temperature, on the system's rheological and mechanical properties.

The results of the DoE model are then validated by formulating a set of control samples and analyzing their mechanical strength, rheological properties, mineralogical composition, and micro structural features. Finally, an optimal formulation is se-

lected as a reference material for the realization of 3D printed building units to be used in the construction of Lunar habitable facilities.

RIASSUNTO

Le agenzie spaziali di tutto il mondo stanno attualmente sviluppando iniziative volte a costruire habitat umani sulla Luna. Dare priorità alla sostenibilità ambientale ed economica è fondamentale per il successo della creazione di insediamenti lunari, soddisfacendo al tempo stesso i requisiti unici della luna. Un approccio sostenibile alla costruzione in ambiente lunare implica un approvvigionamento in loco delle materie prime da utilizzare per la produzione di leganti.

Il concetto di utilizzo delle risorse in situ (ISRU – In Situ Resource Utilization) prevede l'utilizzo di materie prime disponibili sulla Luna (o su altri corpi planetari) per la produzione locale di materiali lavorati o infrastrutture. Sulla base dell'approccio ISRU, la regolite lunare può essere utilizzata come materia prima di provenienza locale per produrre leganti ad attivazione alcalina, adatti alla produzione di materiali da costruzione. Per facilitare lo sviluppo di infrastrutture e habitat lunari, il materiale a base di regolite ad attivazione alcalina deve essere compatibile alle condizioni ambientali presenti sulla luna, comprese le significative fluttuazioni di temperatura, i cicli di gelo-disgelo, gli alti livelli di radiazioni e i frequenti impatti di micrometeoriti. Inoltre, le proprietà reologiche del materiale allo stato fresco e la cinetica di presa e indurimento sono fattori critici che devono essere compatibili con una sua efficiente estrusione durante la fase iniziale del processo di stampa 3D da utilizzare per la messa in posto delle unità strutturali.

La prima parte di questo studio prevede l'utilizzo della diffrazione dei raggi X su polveri (XRPD) e della spettroscopia a dispersione di energia al microscopio elettronico a scansione (EDS-SEM) per identificare le fasi minerali presenti e la composizione elementare del simulante della regolite lunare LMS-1D, nonché la sua reattività durante processo di attivazione alcalina. Il passo successivo consiste nell'utilizzare l'approccio di Design of Experiments (DOE) per ottimizzare la formulazione di regolite ad attivazione alcalina. Ciò implica l'analisi dell'impatto di

fattori critici, tra cui il tipo e la quantità di attivatore alcalino, l'aggiunta di polveri reattive e la temperatura di maturazione, sulle proprietà reologiche e meccaniche del sistema.

I risultati del modello DoE vengono quindi convalidati formulando una serie di campioni di controllo e analizzandone la resistenza meccanica, le proprietà reologiche, la composizione mineralogica e le caratteristiche microstrutturali. Infine, viene selezionata una formulazione ottimale come materiale di riferimento per la realizzazione di unità strutturali mediante stampa 3D, da utilizzare nella costruzione di habitat lunari.

ACKNOWLEDGMENTS

This research was conducted under the GLAMS (Geopolymers for Lunar Additive Manufacturing and Sensing) project, which is funded by the ASI (Italian Space Agency) grant "Research Day" 2023-6-U.0 F93C23000200005.

I am deeply grateful to the GLAMS research group for providing me with the opportunity to be a part of such an innovative and impactful project.

CONTENTS

LIST OF FIGURES

LIST OF TABLES

1 INTRODUCTION

1.1 MOTIVATION AND BACKGROUND

The Moon, being the closest celestial body to Earth, serves as a stepping stone for future space exploration endeavors. The Lunar exploration mission enhances scientific understanding of Earth and the formation of the solar system by studying Lunar geology and chemistry. Moreover, it is the optimal location to conduct trials of space technology for forthcoming expeditions into our solar system. The opposite side of the Moon serves as an advantageous location for doing radio astronomy. An extended duration of human stay on the Moon will serve as a stepping stone for the initial human mission to Mars, which will be the most remarkable accomplishment in engineering and exploration ever witnessed by humanity. The Moon exploration plan is comprised of three distinct phases: an unmanned Lunar probe, a manned Lunar landing, and the establishment of a Lunar outpost. Thus far, the initial two stages have been accomplished. Presently, the primary objective of extraterrestrial exploration is to create a Lunar base and exploit its resources to support future exploration endeavors [116]. Both federal bodies (NASA, ESA, ISRO, etc.) and private firms (SpaceX (Figure 1.1a), Blue Origin (Figure 1.1b), Virgin Galactic, etc.) show a great interest in expanding towards the design and construction of Lunar structures, habitats, and outposts [61]. ESA-NASA's Artemis programs (Figure 1.1d) aim to improve our understanding of the Moon and establish a long-term human presence on and around it. To achieve these aims, space agencies are focusing on landing sites near the South Pole (Figure 1.1c), constructing the Gateway Lunar orbiting platform, and expanding surface expedition lengths [54]. The Chinese Lunar exploration project shares the same objective and aims to establish a Lunar base by 2030 [71].

1.1.1 *Applications and need for Lunar in-Situ construction*

Utilizing in-situ construction is crucial for achieving sustainable Lunar development as it enables the utilization of local resources

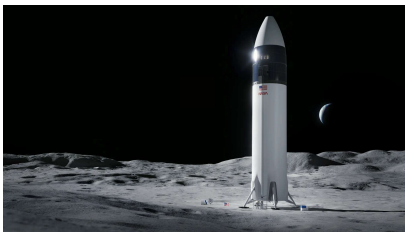

(a) SpaceX Starship human lander design concept.

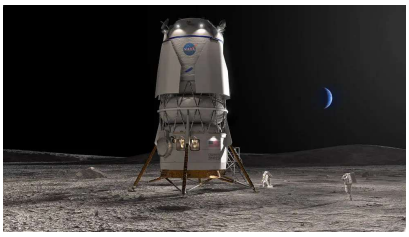

(b) Blue Origin human lander design concept.

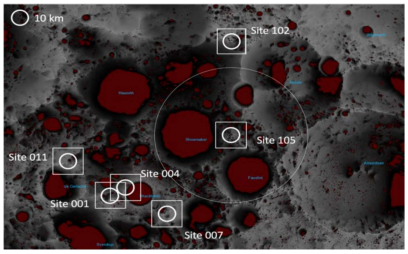

(c) Landing site of interest [54].

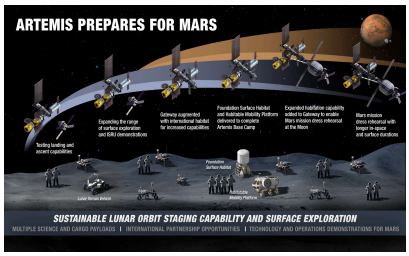

(d) NASA Artemis project landscape for Mars explorations.

Figure 1.1: The Lunar exploration programs' outlook [54],[56].

and minimizes the dependency on supplies from Earth. In-situ resource utilization (ISRU) minimizes the necessity of bringing construction materials from Earth, hence decreasing the energy consumption and pollution linked to long-distance transportation. This method allows the creation of self-sustaining settlements on the Moon by employing Lunar resources like regolith (Moon soil) and autonomous construction technologies such as 3D printing to build structures. Until now, the cost of transporting material from the Earth has been extremely high. The cost of launching 27,500 kg to the Low Earth Orbit (LEO) with NASA's space shuttle was around 1.5 billion dollars, resulting in a cost of 54,500 dollars per kilogram. In 2018, SpaceX's Falcon 9 offered a launch cost of 62 million dollars for sending 22,800 kg into low Earth orbit. This translates to a cost of 2,720 dollars per kilogram [60]. Therefore, the commercial deployment of large quantities of terrestrial matter remains costly. Through the utilization of in-situ construction techniques, we may effectively decrease the expenses and logistical obstacles associated with constructing on the Moon. Additionally, this approach can provide the groundwork for the establishment of sustainable space colonization and exploration. Although in-situ construction on the Moon offers certain benefits, it also presents notable hurdles and potential downsides. When considering

construction materials, the Lunar environment poses numerous substantial challenges. These problems include extreme temperatures, vacuum conditions, radiation exposure, microgravity, Lunar dust, and the lack of water and atmosphere. To tackle these intricate issues, NASA has initiated a synchronized endeavor to investigate the production of oxygen, the extraction of metals from the Lunar soil, and ultimately fabricate bricks and cement using the Lunar soil [75].

1.1.2 *Possible construction methods*

The design of an extraterrestrial structure is still in its early stages. Many researchers have proposed several structural systems, but there are many uncertainties regarding natural hazards, construction methods, and systems. Based on the habitat architectural criteria, the 1997 NASA Habitats and Surface Construction Roadmap defined three classes of Lunar and planetary architectures, ranging from the ones that were built completely on Earth to those that were completely built on the extraterrestrial surface. First idea entails the complete landing of pre-integrated structures on the Lunar surface. The second type consists of pre-fabricated structures that may be assembled, deployed, or inflated on the surface, and the third general category is in-situ resource construction [82].

Inflatable constructions take up little room during transportation from the Earth and can successfully endure high tensile forces when inflated, hence they appear to be the most frequently proposed structural method. Figure 1.2 depicts the inside view of the international space station Transhub [63]. Figure 1.3 depicts the Surface Endoskeletal Inflatable Module (SEIM), a hybrid inflatable module that shares similarities with the Transhub design [2].

Deployable structures have the advantage of being easily packed during transportation and taking up little space. Figure 1.4 depicts a deployable 7m diameter space reflector [76].

Due to the high cost and complexity of transporting large amounts of materials to space, the in-situ resource utilization (ISRU) framework suggests using regolith and robotics to construct the Lunar structures [61]. Figure 1.5 shows a dome structure made using the contour crafting method [65].

Figure 1.2: A schematic illustration of the Transhub internal view [63].

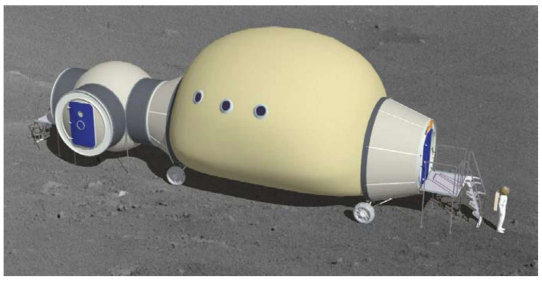

Figure 1.3: Surface Endoskeletal Inflatable Module [2].

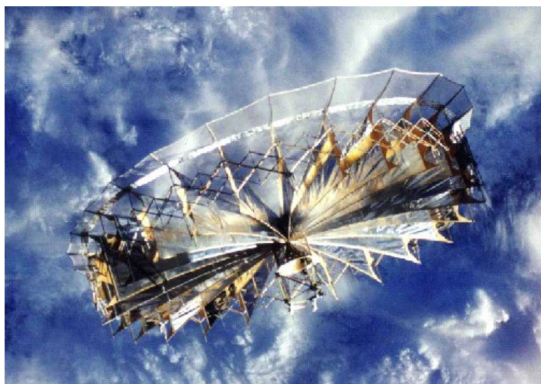

Figure 1.4: Space reflector tested aboard the "Mir" orbital station [76].

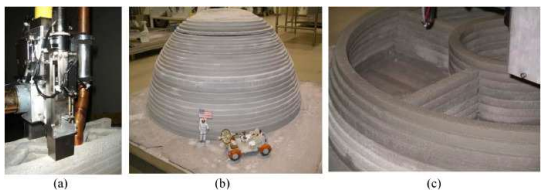

Figure 1.5: Dome structures built by contour crafting method [65].

1.2 THE SIGNIFICANCE OF THE LUNAR REGOLITH

The Lunar surface is divided into two major regions: the Lunar Mare, which refers to the dark, flat plains, and the Lunar Highlands. Figure 1.6 shows a detailed photograph of the Moon, with labeled areas of its surface.

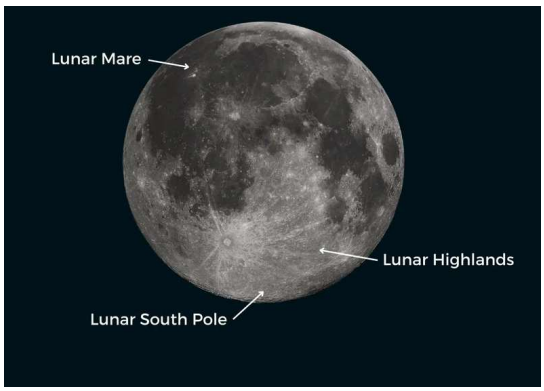

Figure 1.6: A close-up image of the Lunar Mare, south pole, and Highlands [72].

The Lunar Highlands are primarily composed of anorthositic rocks, and the dominant mineralogy is anorthite, with a small amount of iron and magnesium-bearing minerals such as pyroxene and olivine. Chemically, the Lunar Highlands are rich in calcium, aluminum, silicon, and oxygen but low in magnesium and iron (Figure 1.7). On the other hand, the Lunar Mare region consists of basaltic lava flows. Plagioclase, anorthite, orthopyroxene, clinopyroxene, olivine, and ilmenite primarily make up its mineralogy. Thus, these basalts are richer in magnesium, iron, and titanium and poorer in calcium and aluminum [27].

Up until now, researchers have collected all the physical and chemical properties of Lunar material from the Lunar regolith. The regolith is expected to serve as the primary material for constructing Lunar bases [18, 21, 81, 88, 89, 112] and extraction of oxygen and metals [103] [50]. Furthermore, the hydrogen signals on the Lunar south pole (Figure 1.8) suggest the presence of

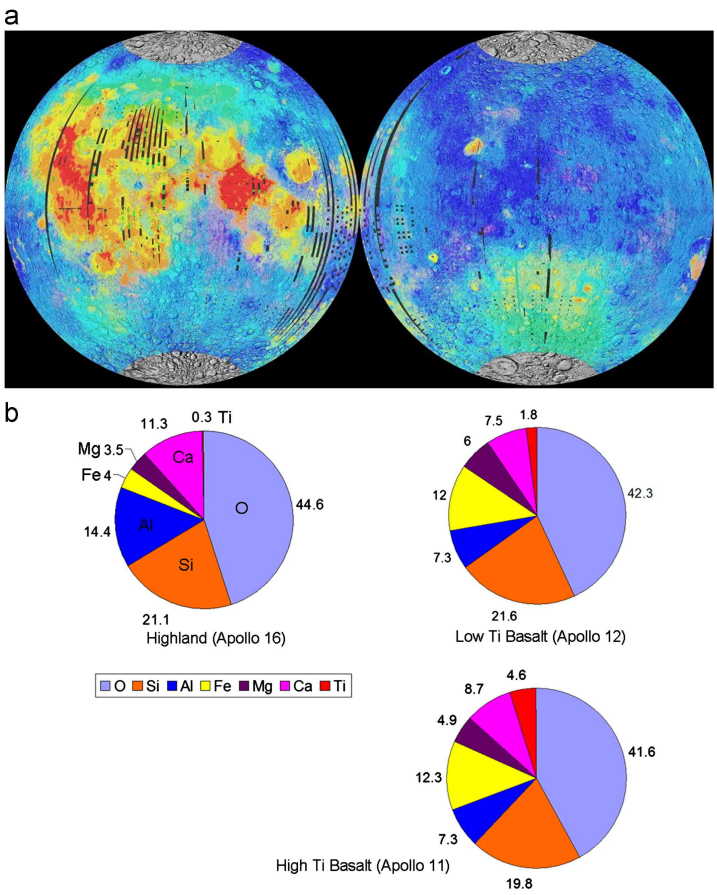

Figure 1.7: (a) Rock type distribution on the Moon's near side (left) and far side (right) Blue: anorthositic Highlands; yellow: low-Ti basalts; red: high-Ti basalts. (b) Chemical compositions of Lunar Highland minerals (Apollo 16), low-Ti basalts (Apollo 12), and high-Ti basalts (Apollo 11) [103].

water in either the form of liquid water or minerals that contain water molecules [40]. The Lunar regolith also contains valuable information about the composition of the Moon's solid surface, as well as the energy dynamics within the solar system.

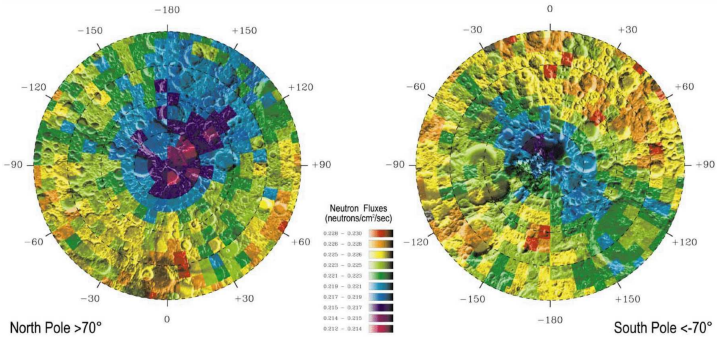

Figure 1.8: Neutron emissions detected at the Lunar poles [40].

1.3 ALKALI-ACTIVATED CEMENTITIOUS MATERIALS (AACMS)

Geopolymers and alkali-activated materials (AAMs) in general are promising materials for use as an alternative binder to ordinary Portland cement (OPC) in the construction industry. Producing a geopolymer, an alkaline solution dissolves an aluminum silicate source, leading to the formation of insoluble phases which conveys cohesive properties [115]. Alkali activated material has various advantages, including lower carbon footprint in comparison with ordinary Portland cement, high durability, quick strength development [124], and raw material flexibility, making it an appealing solution for sustainable and high-performance construction applications. One of the significant benefits of alkali activation is its smaller environmental impact compared to OPC [37], [114]. Alkali activation typically utilizes industrial by-products, reducing the need for energy-intensive clinker production. While OPC relies primarily on limestone as a precursor, alkali-activated materials can be synthesized using a wide range of industrial by-products, including fly ash, slag, metakaolin, and rice husk ash [52]. As a result, alkali-activated materials produce fewer carbon dioxide emissions, helping to mitigate climate change and promote sustainability in construction practices.

1.3.0.1 *Advantages and suitability for Lunar applications*

Considerable amounts of sodium, potassium, silicon, and aluminum are present in the Lunar regolith that can be used for alkali activation [42]. Therefore, alkali activation attracts extensive research interest in the domain of extraterrestrial in-situ fabrication [44]. Alkali-activated materials can be tailored to exhibit superior durability properties [98], freeze-thaw and acid attack resistance [110] , radiation shielding [79], and low thermal conductivity [43] making them ideal for applications in aggressive Lunar environments. Several activation systems, including sodium hydroxide [89] and sodium silicate [44], have been feasible to prepare alkali-activated Lunar regolith simulants. Thus, the utilization of Lunar regolith and alkali metals as components of geopolymer composites can facilitate Lunar construction. Compared to conventional binders, this method can significantly reduce the amount of transported material. However, a 100% ISRU approach would require sourcing liquid water and alkali solutions, which is not straightforward but potentially achievable.

1.4 RESEARCH OBJECTIVES AND SCOPE

This study aims to utilize the design of experiments (DoE) technique to optimize the formulation of an alkali-activated regolith simulant and comprehend the impact of critical factors on the system's rheological and mechanical properties. The factors under investigation include the type and quantity of alkaline activator, the addition of reactive powders, and the curing temperature.

- Characterization of Lunar regolith simulant (LMS-1D):

  We employed X-ray powder diffraction (XRPD) analysis and energy dispersive spectroscopy scanning electron microscopy (EDS-SEM) to identify the present mineral phases and elemental composition of the LMS-1D Lunar regolith simulant.

- Experimental design and modeling:

  A total of 26 experiments were conducted to build empirical models that correlate the formulation parameters with the rheological properties and compressive strength of the alkali-activated regolith simulant. The DoE approach al-

lows for efficient exploration of the parameter space and identification of optimal formulations.

- Verification and validation:

  Three additional experiments were performed using the optimized formulations to verify the accuracy of the empirical models in predicting the yield stress and compressive strength of the solidified product. This validation step ensures the reliability and applicability of the developed models.

- Characterization of final products:

  The final products resulting from the optimized formulations were subjected to XRPD analysis and EDS-SEM for phase identification, elemental analysis, and mapping, respectively. This comprehensive characterization provides insights into the microstructural changes and chemical composition of the alkali-activated Lunar regolith simulants.

- Conclusion and implications:

  By achieving optimization of the formulation parameters and understanding their impact on the properties of alkali-activated regolith simulants, this research contributes to advancing the feasibility and sustainability of in-situ resource utilization for future space exploration missions.

2

LUNAR GEOLOGY

2.1 THE LUNAR ENVIRONMENT'S CHALLENGES

The Lunar environment poses significant challenges and hazards to astronauts' well-being, survival, and security, as well as construction materials. Therefore, establishing a Lunar base is a complex task [12].

- Severe temperature fluctuations

  The temperature on the Lunar surface experiences substantial changes (Figure 2.1). The Lunar day has a duration of 29.53 Earth days, leading to alternating periods of intense sunlight and cold nights. The temperature on the Moon's surface exhibits a wide variation, varying from scorching hot to freezing cold [61]. Extreme temperatures can cause construction materials to expand and compress, as well as become brittle, leading to structural instability [59].

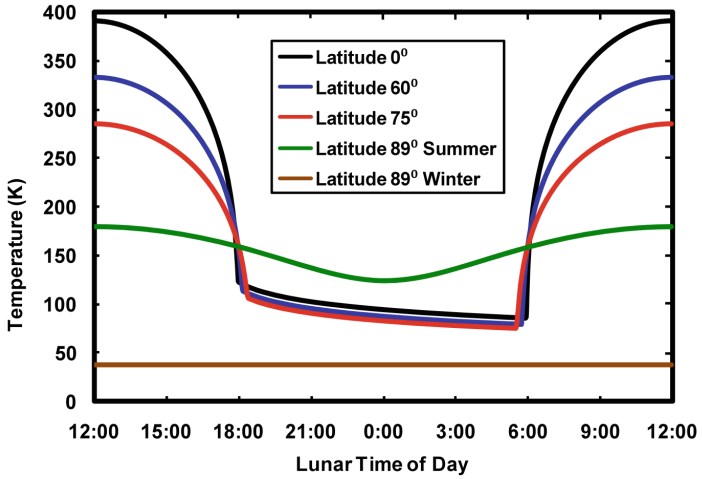

Figure 2.1: Lunar surface temperature variation at different latitudes. Diurnal temperature variations at 89 degrees latitude are shown at summer and winter solstices. Local time is expressed in Lunar hours, which correspond to 1/24 of a Lunar month [83].

  The polar regions are a good choice for establishing settlements and infrastructure because they receive less insola-

tion than equatorial and lower latitude regions, resulting in milder diurnal thermal cycling [64].

- Lack of water and atmosphere

  The Moon's lack of water and atmosphere restricts the availability of resources for construction materials. Although the Air Force's Clementine and, consequently, the NASA-Ames Lunar Prospector missions detected water ice at the north pole, the concentration and availability are challenging. The lack of an atmosphere results in a vacuum that can affect the behavior and durability of construction materials[24].

- Radiation exposure

  The Sun and cosmic rays expose the Moon's surface to high levels of radiation. Galactic cosmic rays (GCR) or solar energetic particles (SEO) cause hazardous radiation that poses a great threat to the subsystems of any Lunar structure and electronics[85]. This radiation exposure may reach seven times the Earth's allowable amount and can degrade and damage construction materials over time, compromising their structural integrity. Some data show that the Lunar regolith cover for the habitats should be at least 1 meter to properly shield the radiation[24].

- Microgravity

  The Moon has a significantly lower acceleration of gravity. Compared to Earth, the gravity experienced on the Moon is about 1/6 of that on Earth [51]. This microgravity environment poses challenges for construction materials, as their behavior and structural strength may be different without the gravitational forces experienced on Earth.

- Lunar dust

  Micrometeorites constantly hit the Lunar surface; thus, the Moon's surface is covered in a layer of fine dust that is continually charged by the solar wind. This Lunar dust can diminish visibility and pose challenges for construction materials. Moreover, Lunar dust is abrasive and can infiltrate equipment and structures, potentially causing wear and damage[59].

- Meteoroid impacts

Lacking an atmosphere, the meteorites impact the Moon's surface without slowing down or burning. Impactors have velocities that vary from 2.4 to 72 km/s[61], which is a threat to any type of construction.

- Seismicity

  The tides generated on the Moon due to the relative motions of the Sun and the Earth produce deep moonquakes, which are the most commonly classified natural sources of ground motion, ranging from 0.5 to 1.3 on the Richter scale[68]. Shallow moonquakes are the rarest and most seismically energetic phenomena observed on the Moon [61]. The shallow moonquakes' focal depths range from 0–200 km with the largest magnitudes of 4 to 5 on the Richter scale[68]. The Apollo passive seismic network has also recognized thermal moonquakes as small local events caused by temperature variations on the Lunar surface. The generation procedure for such seismic events is the fracturing or movement of the regolith in response to diurnal changes in thermal stresses [33].

2.2 LUNAR MISSIONS AND REGOLITH SAMPLES

By the end of 1972, the Apollo missions had brought a total amount of 382 kg of Lunar regolith back to Earth(Figure2.2a, 2.2b). The Luna missions between 1970 to 1976 also brought 321 grams of Lunar regolith to Earth [61].

On December 1, 2020, China's ChangE-5 sample return mission successfully touched down in the northwest corner of the Moon[119]. The lander acquired 1.7 kg of specimens via a mechanical scoop and a drill capable of penetrating 2 meters beneath the surface[126].

The chemical compositions of Lunar regolith samples indicate their various origins. However, collected regolith samples often exhibit constituents that are not typically expected at the sampling location[50]. Table2.1 shows the major element concentration of Apollo, Luna, and ChangE missions in Wt.%.

2.2.1 *Regolith*

Regolith is a terrestrial term that is also used for the Moon. Generally, regolith refers to a highly varied layer of fragmented and unconsolidated rock material that covers the land or bedrock

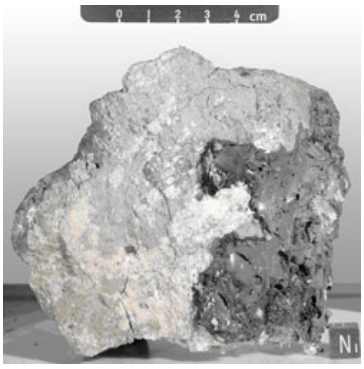

(a)

(b)

Figure 2.2: (a) The Apollo 16 breccia boulder, weighed one kilogram. The black glass on the side was created from the collision of a meteorite, and (b) an astronaut gathering a Lunar soil sample [73].

almost everywhere[9]. The ongoing collision of meteorites and the bombardment of charged atomic particles on the Moon's surface form the Lunar regolith. The regolith layer covers the entire Lunar surface, with some exception of steep crater walls and lava channels[50]. The diameter of impact craters on the Lunar surface varies from over 1000 kilometers to under 1 micrometer. These impacts generate shock waves that cause an increase in pressure and heat. This results in the melting and fusion of the pulverized Lunar material, leading to the formation of breccias and impact melt rocks. The formation processes of regolith can be categorized into two primary stages: the first stage involves the initial exposure of the bedrock to the surface and is subjected to direct impact, while the second stage entails the bedrock being overlaid with a layer of regolith. During the later stages, the smaller yet abundant impacts just disrupt and blend the upper layer of the regolith. The regolith thickness typically does not exceed 10 to 20 meters, as only a small amount of regolith is needed to provide shielding for the underlying bedrock [50].

2.2.2 *General description*

Generally, the Lunar soil is a loose material that is cohesive, ranging from dark gray to light gray. It is defined as the unconsolidated section of regolith with particle sizes smaller than 1 cm. It is also referred to as the Lunar regolith, which has the same meaning in terms of its composition and characteristics [9].

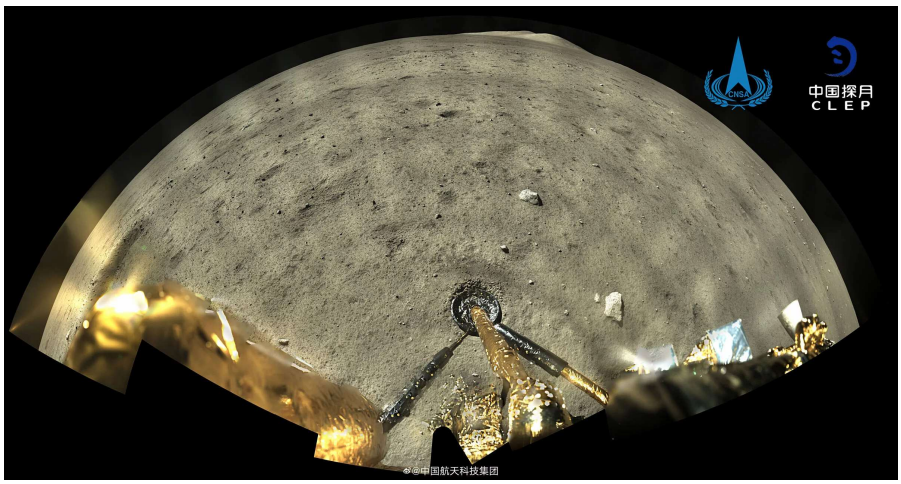

Figure 2.3: A photograph depicting the Lunar surface taken shortly after the landing in the "Ocean of Storms" on 1 December 2020. The image is credited to CNSA / CLEP[22].

Since particles less than 1mm make up the majority of regolith samples, most regolith analyses have concentrated on these fractions, while the relatively large fragments are treated as rock samples.

The Lunar soil primarily forms from the mechanical disintegration of basaltic and anorthositic rocks, with a little meteoritic component comprising around 2% of the total. The average grain size of the soils varies from around 40 μm to 800 μm, with an average range of 45 to 100 μm. The main part of Lunar soil particles is made up of agglutinates, which are glass-bonded aggregates, along with a variety of rock and mineral fragments. When the impacts are large enough, bombardment of the Lunar regolith surface reconsolidates sections of the regolith into regolith breccias [50]. While Lunar soils exhibit a significant variety in their chemical compositions, their physical qualities, including particle size, density, packing, and compressibility, are quite consistent[26].

Several consecutive impact events and chemical modifications make it difficult to define the exact chemical composition of the Lunar regolith [8]. Apart from agglutinates, which make up the largest portion of the Lunar soil, and volcanic glass, a significant percentage of Lunar soils, approximately 3–5%, consist of small irregular fragments of impact glass. These glass fragments are formed when the regolith is melted by the impacts, and the compositions of many of these glasses consist of a mixture of rock types. Another notable component of Lunar soil is ropy glass, which has a diverse range of chemical compositions and

	Apollo Missions[62]					Luna Missions[62]				ChangE [126]
	11	12	14	15	16	17	16	20	24	5
SiO_2	42.2	46.3	48.1	46.9	45	43.2	41.7	45.1	43.9	41.25
TiO_2	7.8	3	1.7	1.4	0.54	4.2	3.4	0.55	1.3	5.12
Al_2O_3	13.6	12.9	17.4	14.6	27.3	17.1	15.3	22.3	12.5	11.55
Cr_2O_3	0.3	0.34	0.23	0.36	0.33	0.33	0.28		0.32	
FeO	15.3	15.1	10.4	14.3	5.1	12.2	16.7	7	19.8	22.7
MnO	0.2	0.22	0.14	0.19	0.3	0.17	0.23	0.13	0.25	0.28
MgO	7.8	9.3	9.4	11.5	5.7	10.4	8.8	9.8	9.4	6.52
CaO	11.9	10.7	10.7	10.8	15.7	11.8	12.5	15.1	12.3	11.64
Na_2O	0.47	0.54	0.7	0.39	0.46	0.4	0.34	0.5	0.31	0.46
K_2O	0.16	0.31	0.55	0.21	0.17	0.13	0.1	0.1	0.04	0.21
P_2O_5	0.05	0.4	0.51	0.18	0.11	0.12	0.12	0.16	0.11	0.27
S	0.12			0.06	0.07	0.09	0.21	0.08	0.14	
Total	99.9	99.6	99.8	100.8	100.8	100.5	99.7	100.8	100.4	100

Table 2.1: Bulk composition of samples from Apollo, Luna, and ChangE Missions.

contains fine, dusty soil grains as inclusions. It may also contain skeletal crystals that formed during the glass's cooling and solidification. Studying the mineral and chemical composition of regolith is made more complex by the existence of shock minerals and chemical fractionation processes that can occur during impact melting. For example, the process of selectively evaporating of silicon can result in the formation of new glass compositions that do not match any Lunar bedrock[50].

2.2.3 *Petrography*

Lunar soil is made of fragments of minerals, crystalline rocks, breccia, and agglutinates. Breccias, agglutinates, and glasses are a result of meteorite impact, and the glassy fraction of the regolith comes from the groundmass of basaltic rocks and agglutinates. The finer soil fractions tend to be predominantly concentrated in minerals prone to easy fragmentation, such as plagioclase and glassy phases. The concentration is particularly evident in the portion with a size of less than 10 μm [30]. The average size of crystalline rock fragments in regolith is below 250 μm and is made up of igneous rocks, monomictic, and polymictic breccias. Polymineralic and lithic fragments dominate the coarser size fractions. The Apollo 11, Apollo 12, Luna 16, and Luna 24 missions landed in the Mare region, which is predominantly basalt. The mafic minerals in this region are py-

roxene and olivine. The Apollo 16 and Luna 20 missions landed in Highland regions in which lithic samples are predominantly anorthositic rocks and plagioclase feldspar. Apollo 15 and 17 have an intermediate character between those from the Mare and Highland regions. The bar graph (Figure2.4) shows the modal abundance of principal particle types in 14 Lunar soil samples. Soil samples are from Apollo 11 (10084), Apollo 12 (12xxx), Apollo 14 (14163), Apollo 15 (15xxx), Apollo 16 (6xxxx), Apollo 17 (7xxxx), Luna 16 (21000 and 22001), and Luna 24 (24999), numbered with the relevant mission code [105].

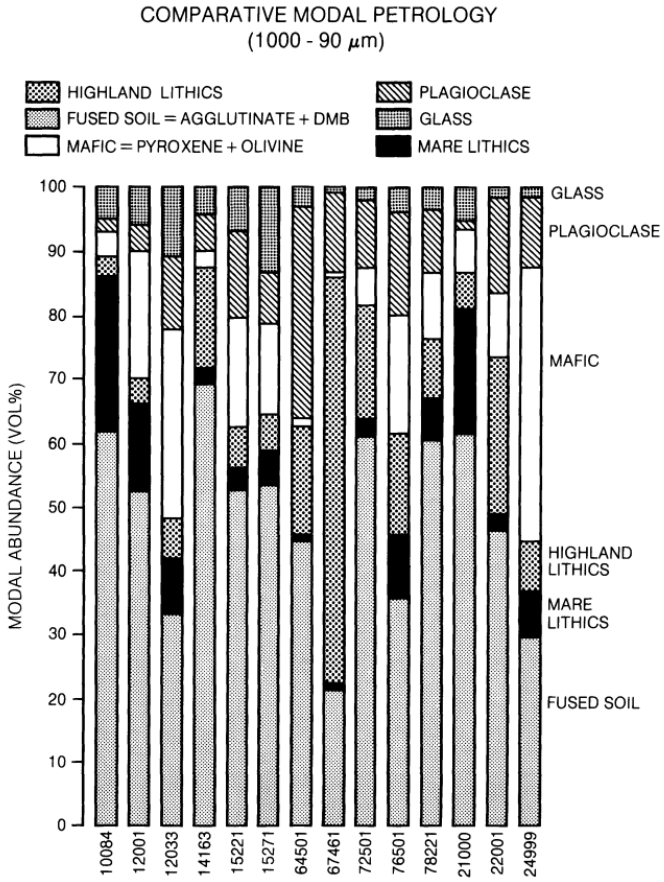

Figure 2.4: Bar graphs displaying the most common (volume) abundances of the main particle types found in 14 Lunar soil samples, "dmb" stands for dark matrix breccia [105].

2.2.4 *Agglutinates*

Agglutinates are composed of smaller Lunar soil particles such as mineral grains, glasses, and older agglutinates. These particles are held together by vesicular, flow-banded glass. Agglutinate

particles, as depicted in Figure2.5, often have a size of less than 1 mm. They consist of small droplets of Fe metal, with a significant portion being very fine-grained and single-domain Fe°, as well as troilite (FeS). The creation of these formations is most likely caused by the melting and blending that occur due to the bombardment of the Lunar surface by micrometeorites [50].

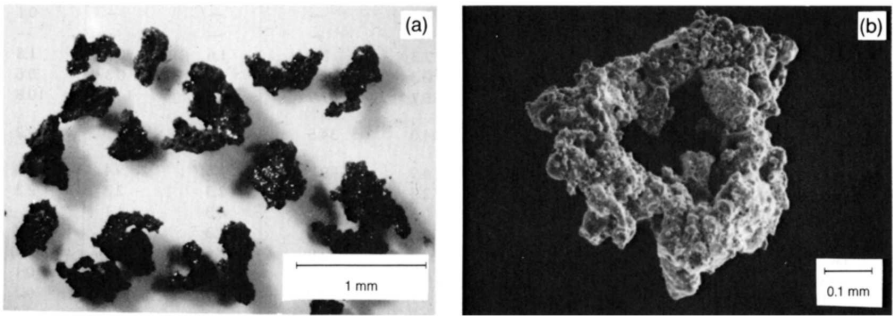

Figure 2.5: (a) Optical microscope photograph (NASA Photo S69-54827) of agglutinates and (b) Scanning electron microscopy image (NASA Photo S87-38812) of a doughnut-shaped agglutinate[50].

Agglutinates are the main constituents of Lunar soils and, on average, make up 25 to 30% of Lunar soils, but their quantity can vary from a rare 5% to 65%. Because agglutinates are continuously created by micrometeoroid bombardment at the regolith's surface, the amount of agglutinates in Lunar soil grows with time and is proportional to its cumulative exposure age. Agglutinates are distinguished by their fine-grained (300 Å), single-domain Fe° metal structure. The study of the ratio of agglutinitic glass composition to the bulk soil composition for the Luna 24 soil samples, which are highly immature and relatively pure Mare soils, shows an inclination of the chemical composition of agglutinitic glass towards the below 10 μm fraction of the initial soil (Figure2.6) [84].

2.2.5 *Grain-size characteristics*

The processes involved in creating Lunar soil are complex. Micrometeoroids striking Lunar rocks cause particles to fragment into smaller components. In the mean time, small amounts of molten material are produced that adhere to nearby particles (Figure2.7a,and2.7b) [50].

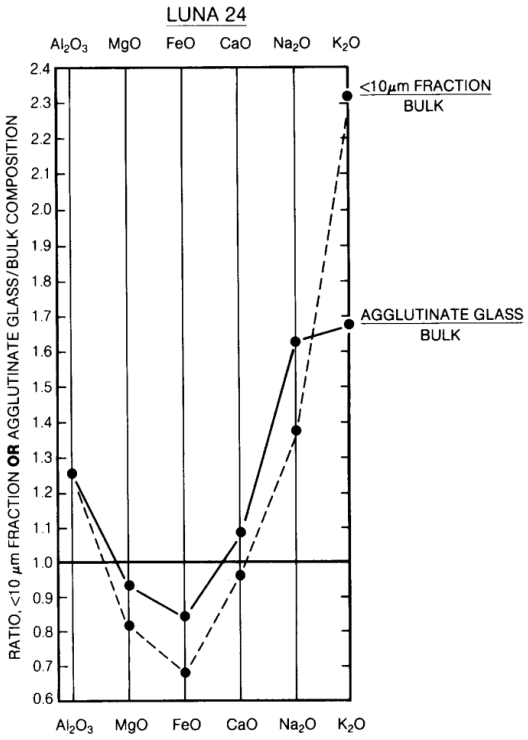

Figure 2.6: The plot illustrates the resemblances in chemical composition between agglutinate glass found in the Luna 24 soils and the proportion of Luna 24 soils that is smaller than 10 micrometers[84].

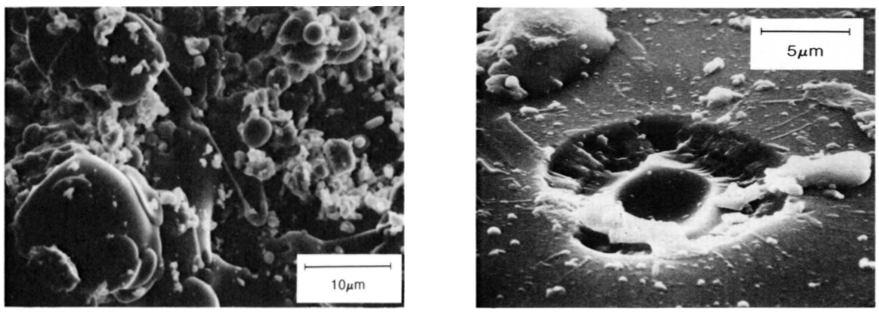

(a) (b)

Figure 2.7: (a) SEM image of a plagioclase grain from Lunar soil sample 10084 with irregular glass splashes and fine-grained bits of crystals and glass attached to them, and (b) Micrometeoroid impact crater on the surface of a Lunar soil particle [50].

In general, the average and minimum grain sizes of collected Lunar soil samples show differences between sampling locations. Most of the Lunar regolith samples would consist of silty sands with pebbles or cobbles. The Lunar soils exhibit a variety of sorting qualities, ranging from low to very low. Furthermore, samples with the highest grain size have the least amount of sorting. The soil samples collected from all the Apollo sites display a distribution that is somewhat skewed, with skewness values ranging from 0 to 0.3 (Figure2.8). The average grain size of Lunar soils varies from 40 to 800 μm, with the majority of averages falling between 45 and 100 μm [50].

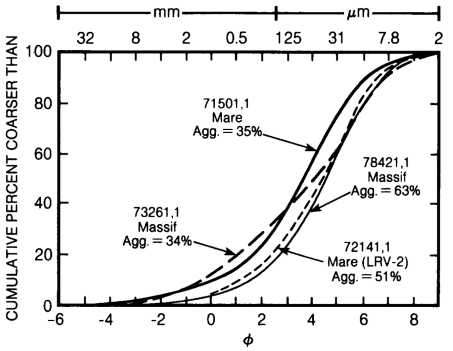

Figure 2.8: Cumulative distribution function of particle sizes in typical Lunar surface soil samples. The term "Agg" is used to describe the agglutinate content found in individual soil samples[50].

2.2.6 *Regolith density*

The minimum bulk densities of Lunar soil varies from 0.87 to 1.10 g/cm^3, while the maximum densities varied from 1.51 to 1.89 g/cm^3. The observed variations in values can be attributed to intragranular voids, particle morphology, surface texture, and grain configurations. The Lunar soil located in the plains regions of the Moon has a relatively low to medium density at the surface, which thereafter experiences a quick increase to a very high relative density at depths above 10 to 20 cm[19]. Figure2.9 illustrates the relationship between the in situ bulk density of Lunar soil and the depth below the surface. Three density-depth relations that have been calculated are: linear (shown by a solid line), power-law (represented by a heavy dashed line), and hyperbolic (represented by a light dashed line). The uppermost boxes in the plot display the suggested

bulk density values for intercrater zones in close proximity to the surface[50].

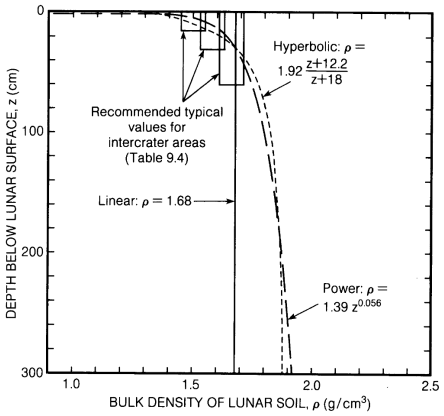

Figure 2.9: Relationship between the in situ bulk density of Lunar soil and the depth[50].

2.3 LUNAR REGOLITH SIMULANT

Obtaining Lunar soil samples is logistically challenging and expensive. While NASA and other space agencies have collected Lunar soil samples, the quantity of these samples is limited and restricted for research purposes. Lunar regolith simulants offer a cost-effective solution with consistent and reproducible properties for scientific experiments, engineering tests, and technology development. They can be customized to mimic specific properties of Lunar soil, such as grain size distribution, mineral content, and chemical composition. JSC-1 has been one of the most extensively studied Lunar simulants; however, its resources have been depleted over time. LMS-1 is a new commercially available Lunar regolith simulant that mimics the composition of Lunar Mare regolith.

2.3.1 *LMS*

LMS-1 (Figure2.10) is a Lunar simulant developed by the University of Central Florida [57]. The developers' main goal was to produce a high-fidelity mineralogical simulant for the Moon in correct mineralogical proportions. The ingredients for the extra-fine Mare region dust simulant (LMS-1D) were mixed at specific weight ratios (Table2.2) to fit the mineral distribution of the Mare Lunar regolith. The main components used are pyroxene, glass-rich basalt, anorthosite, olivine, and ilmenite.

Figure 2.10: LMS-1D Simulant, photo credit Matthew Villegas[72].

Component	weight %
Pyroxene	32.8
Glass-rich basalt	32.0
Anorthosite	19.8
Olivine	11.1
Ilmenite	4.3

Table 2.2: Mineralogy of the mixed LMS-1D Lunar simulant[72].

Oxides	LMS-1 %	LMS-1D %
SiO_2	44.2	46.9
TiO_2	3.5	3.6
Al_2O_3	11.9	12.4
FeO	11.5	8.6
MnO	0.2	0.2
MgO	17.1	16.8
CaO	8.6	7.0
Na_2O	0.9	1.7
K_2O	0.4	0.7
P_2O_5	0.9	0.2
LOI		0.9
Total	99.2	99.0

Table 2.3: LMS-1 and LMS-1D Lunar regolith simulants bulk chemistry, LOI indicates loss on ignition[72].

As reported by the producers, the main oxides in the LMS-1D are SiO_2 (46.9 %), MgO (16.8%) and Al_2O_3 (12.4%), respectively. The relative abundance of oxides in the LMS-1 and LMS-1D samples was measured using the fused bead sample preparation technique (Table2.3). The mean and median particle sizes of the LMS-1D Lunar simulant are 7 μm and 4 μm, respectively [72].

3

ALKALI ACTIVATION

3.1 INTRODUCTION

Concrete, which is essential for the construction of homes and infrastructure, relies heavily on cement as a key ingredient. Global cement production is expected to expand by 12–23% by 2050, driven by rising population and urbanization [20]. Ordinary Portland cement (OPC) is made by heating a mixture of finely ground limestone, clay, and other minor ingredients at about 1450°C in a rotary kiln[91]. Worldwide production of cement in 2023 was around 4.1 billion metric tons [77], making it one of the highest-volume commodities produced worldwide. Therefore, developing a low-carbon alternative binder is an important option to reduce anthropogenic CO2 production.

Geopolymers and alkali-activated materials (AAMs) in general are promising materials that may serve as an alternative binder to ordinary Portland cement (OPC). In contrast with pozzolanic cement that depends on the presence of calcium and calcium silicate hydrates (C-S-H) for matrix formation, geopolymers get their strong structure from linking together building blocks of silicon and aluminum in a chemical process that requires a very alkaline environment[115]. The desired properties of AAMs can be tailored to resist acid attacks and silage effluent[4], higher heat transfer rate and less cracking and spalling [99], and higher compressive strength[5]. Geopolymers can also be utilized for industrial by-product stabilization and heavy metal immobilization[115].

Kühl [67] in 1908 patented the reaction of an alkali source with a solid aluminum and silicon-containing precursor to form a Portland cement-like solid material[91]. By definition, alkali-activated material (AAM) is generally any binder system derived by the reaction of an alkali metal source with a solid aluminosilicate powder[104]. Any soluble substance that can provide alkali metal cations and accelerate the dissolution of the solid precursor by raising the pH is an alkali source. It includes alkali hydroxides, silicates, carbonates, sulfates, and aluminates. The solid can be a calcium silicate (conventional clinker) or an aluminosilicate-rich precursor such as fly ash or bottom

ash, natural pozzolan, metallurgical slag, or a combination of them. Based on the amount of calcium content of the binder material, three categories of alkali-activated materials are high-calcium alkali-activated materials, such as metallurgical slags; low-calcium alkali-activated materials, such as metakaolin; and intermediate or blended systems [91].

3.2 ACTIVATION CHEMISTRY

In general, aluminosilicate binder materials are activated by alkali hydroxides or silicates under high-pH conditions. Sodium and potassium are the most commonly used alkali activators. Due to their abundance and cost, lithium, rubidium, and cesium hydroxides have limited applications. The most important properties of hydroxide solutions are high corrosivity, heat release during alkali hydroxide dissolution, and viscosity [93]. Figure 3.1a shows the standard enthalpies of alkali metal hydroxide dissolution to infinite dilution at 25°C as a function of cation size.

Sodium hydroxide($NaOH$) is commonly used for hydroxide activation of the AAM since it's cheap and widely available. Figure3.1b shows the phase diagram for the $NaOH - H_2O$ system. The sodium hydroxide($NaOH$) solubility at 25°C is 53.3% by mass (28.57 m), but falls below 30 wt% (10.73 m) at 0°C [90].

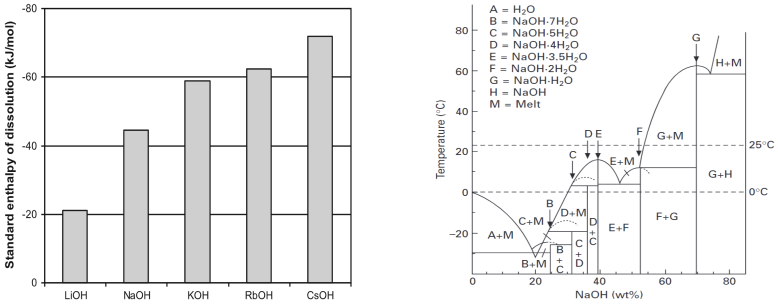

(a) (b)

Figure 3.1: (a) Standard enthalpy of dissolution to infinite dilution of the alkali hydroxides[46, 47], and (b) Phase diagram for the $NaOH - H_2O$ system [90].

Alkali silicates are mainly produced from carbonated salts and silica via calcination, then dissolved in water at the desired ratios[93]. As in the case of hydroxides, in alkali activation technology, silicates of sodium and potassium are more widely used in industry[90]. Figures 3.2a and 3.2b illustrate the sharp

increase in viscosity with the increase in molality for alkali hydroxide and sodium silicate solutions at room temperature [93].

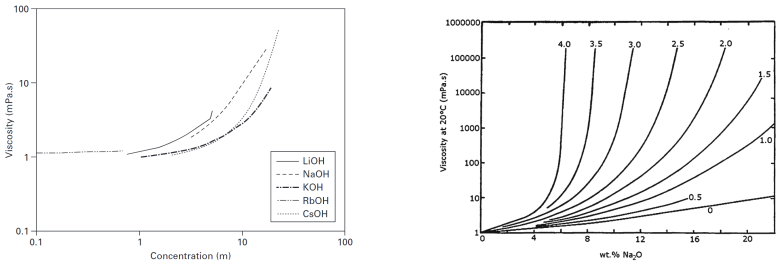

(a) (b)

Figure 3.2: (a) Viscosities of alkali hydroxide solutions as a function of molality at 25°C, and (b) Viscosities of sodium silicate solution with mass ratio SiO_2/Na_2O marked at room temperature [93].

3.3 GEOPOLYMERS

Davidovids led the early developments of low-calcium alkali-activated binders, which resulted in the formation of ceramic-like fire and acid-resistant material. The term "geopolymer" was applied to a class of solid materials that are synthesized by the reaction of an alkaline solution with an aluminosilicate powder [28].

Figure 3.3 shows a simplified graphical distinction of the concrete-forming materials. Geopolymers are generally considered a subset of the alkali-activated material with the highest aluminum and the lowest concentration of calcium concentrations. Geopolymers are mainly synthesized by combining an alkaline solution with a reactive aluminosilicate powder, in particular metakaolin or fly ash, resulting in the production of an alkali aluminosilicate gel phase known as the geopolymeric gel binder phase[91]. There are similarities between the binder structure in low-calcium alkali-activated systems and the structure of zeolites[95]. Bell et al. (2008) found similarities between the structural order of metakaolin-based $KAlSi_2O_6.5.5H_2O$ geopolymer and leucite on a length scale up to 8 Å [10],[11].

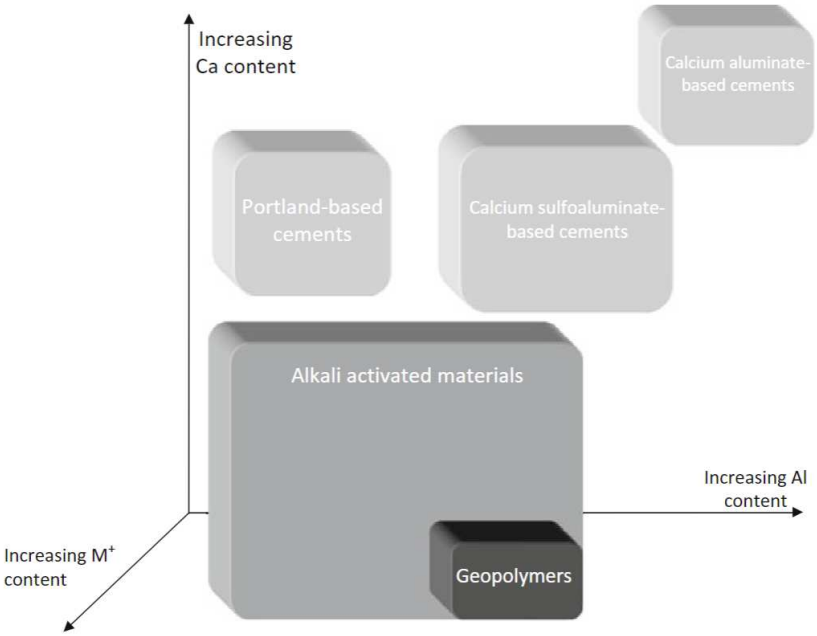

Figure 3.3: Classification of AAMs, with comparisons to OPC and calcium sulfoaluminate binder chemistry. Darker shading corresponds to higher concentrations of sodium (Na) and/or potassium (K)[91].

3.4 METAKAOLIN

Metakaolin is the product of the kaolinite clay calcination process at 500–800 °C. Kaolinite ($Al_4[Si_4O_{10}](OH)_8$ Figure3.4) is a 1:1 dioctahedral phyllosilicate and is the main component of the kaolinite group of minerals. It can be mined directly or is available in the form of industrial waste[108].

The temperature must be sufficiently high to remove the bound water from the clay structure. Since pure kaolinite does not have interlayer water, the calcination of the kaolinite is only governed by the dehydroxylation process. It is generally accepted that metakaolin is formed by a gradual loss of structural water while the aluminum coordination changes from six to four folds. The metakaolin is amorphous and appears disordered to X-ray diffraction analysis (Figure3.5)[90].

The molecular dynamics (MD) simulations show that the loss of hydroxyl groups at the surface of the inter-layer spacing governs the loss of crystallinity. The loss of the hydroxyl groups causes the migration of the aluminum into the vacant inter-layer space. Finally, this migration causes the buckling of the layers. Figure3.6 shows the molecular dynamics (MD) simulation of

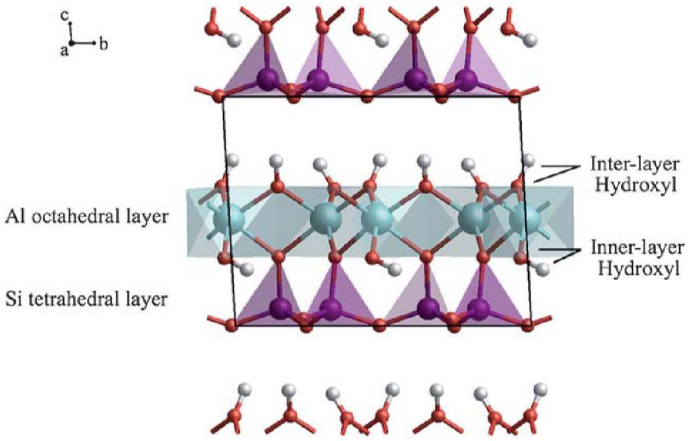

Figure 3.4: The ideal layered structure of kaolinite unit cell, vertex sharing SiO_4 tetrahedra forming six-membered silicate rings that are linked by common oxygen atoms parallel to the c-axis to a sheet of edge-sharing AlO_6 octahedra forming four-membered aluminate rings[108].

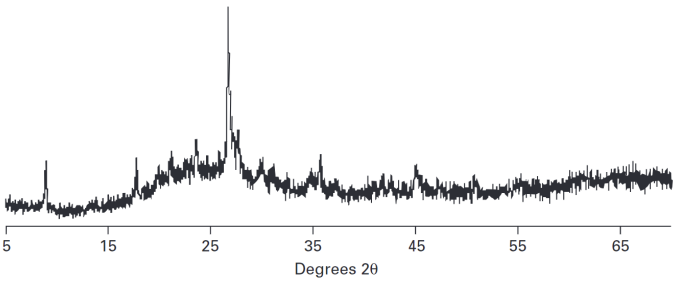

Figure 3.5: Cu Kα diffraction pattern of commercial metakaolin. The 15-35 2θ broad peaks are related to the amorphous metakaolin. Sharp peaks are related to muscovite impurity[90].

dehydroxylation process of the kaolinite (top left) along the a axis in 20% steps. Figure3.7 shows a fully dehydroxylated kaolinite structure in which 1:1 layering is still visible[108]. Since metakaolin is derived by the hydroxyl group removal from the layered kaolinite (Figure3.4), the dehydroxylation process is partially reversible[92].

3.4.1 *Metakaolin geopolymirization*

Metakaolin-based geopolymers have been among the first successfully produced geopolymers. Alkali hydroxide activation of low calcium precursors such as metakaolin is dominated by an alkali aluminosilicate gel. Depending on the reaction conditions,

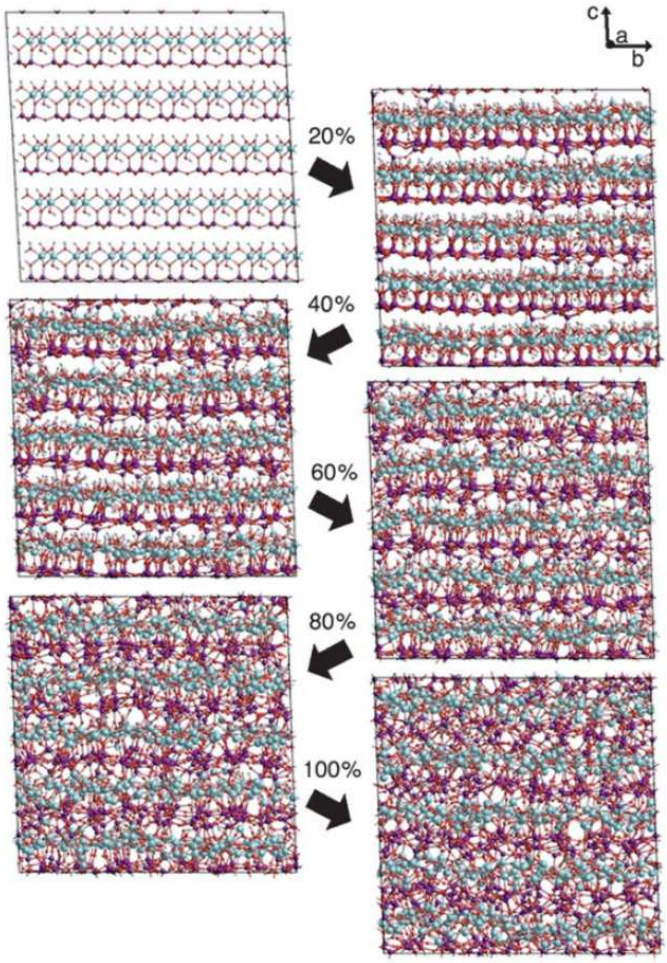

Figure 3.6: The molecular dynamics (MD) simulations of the kaolinite dehydroxylation process along the a axis in 20% steps[108].

the reaction of the metakaolin with alkalis forms one or more types of zeolites [10, 11].

Infrared spectroscopic techniques on the sodium hydroxide (NaOH)-activated fly ash identified two stages of gel evolution (Figure 3.8). 'Gel 1', which is relatively richer in $Si - O - Al$ bonding, and 'Gel 2', form at longer reaction times as the extent of silicon (Si) crosslinking within the gel increases. Crystallites that form during sodium hydroxide (NaOH) activation of metakaolin are predominantly feldspathoids in the hydro-sodalite, hydroxy-sodalite family. Some zeolitic phases (zeolite $Na - A$ or low-silica faujasites) are observed as either transient or later-developing reaction products [90, 94]. Based on the mix design, curing temperature, and contamination, geopolymer gel grows to the point where the reacting slurry solidifies almost instantaneously, or after several days.

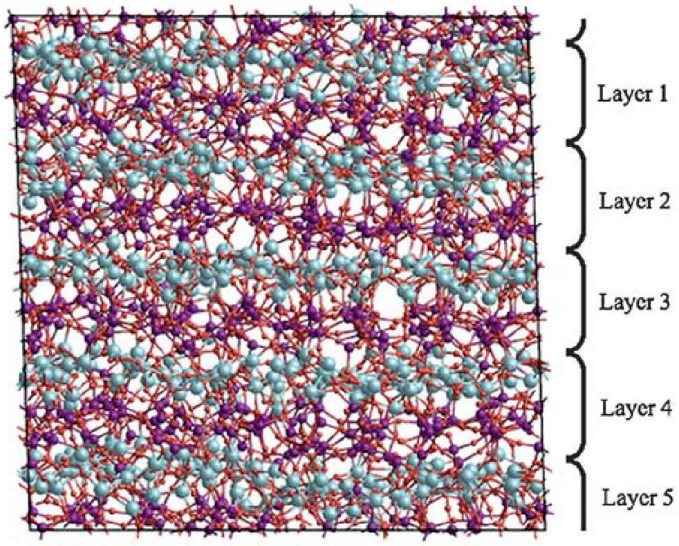

Figure 3.7: A snapshot of molecular dynamics (MD) simulation of a fully dehydroxylated kaolinite structure[108].

The SEM micrographs of the sodium hydroxide (NaOH)-activated metakaolin geopolymer ($Si/Na = 4/4$) clearly show the presence of zeolite $Na - A$ cubic crystals (Figure 3.9a). Increasing $Si/Na = 4/6$ causes the rapid crystallization (about 2.5 hours) of a very small (about 21 nm) unnamed zeolite, $Na_6[AlSiO_4]_6.4H_2O$ (Figure3.9b)[122].

The SEM image of the sample synthesized using a combination of sodium hydroxide (NaOH) and sodium-silicate activators (Figure3.10) shows no crystal morphology but appears to be of denser texture than the samples synthesized with sodium hydroxide (NaOH) only (Fig3.9a,3.9b)[122].

The binder gel structure that is formed through silicate activation with low calcium precursors such as metakaolin is similar to the binder gel structure formed through hydroxide activation. However, there are differences, at the atomic length scale, and Si/Al ratios, and there is a lower tendency toward zeolite/feldspathoid crystallization at higher Si content. Compared with hydroxide activation, metakaolin silicate activation tends to develop acceptable strength across a wider range of mix designs and curing conditions [94]. However, the addition of even a small amount of sodium silicate to the sodium hydroxide (NaOH)-activated metakaolin drastically suppresses crystallite formation[122]. Silicate activation tends to produce products with lower porosity and higher strength binder[109].

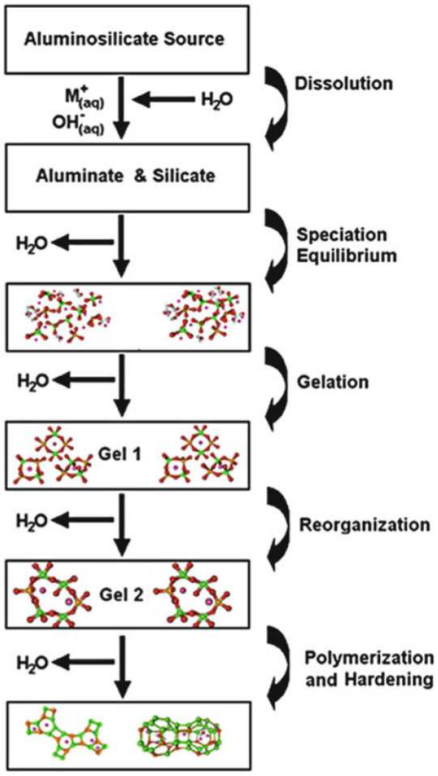

Figure 3.8: Alkali-activated binder synthesis conceptual model. Multi-step gel evolution of hydroxide activation of aluminosilicate source[34].

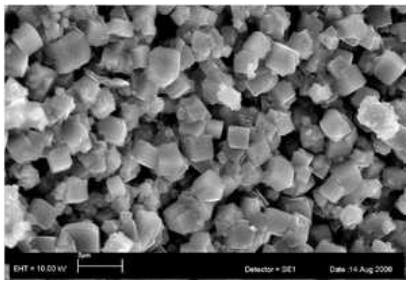

(a) SEM image of samples synthesized using sodium hydroxide (NaOH) activator with Si/Na = 4/4.

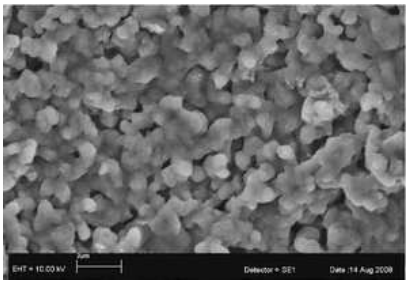

(b) SEM image of samples synthesized using sodium hydroxide (NaOH) activator with Si/Na = 4/6.

Figure 3.9: Internal pore surface SEM images of samples synthesized using sodium hydroxide (NaOH) activator with different Si/Na ratios[122].

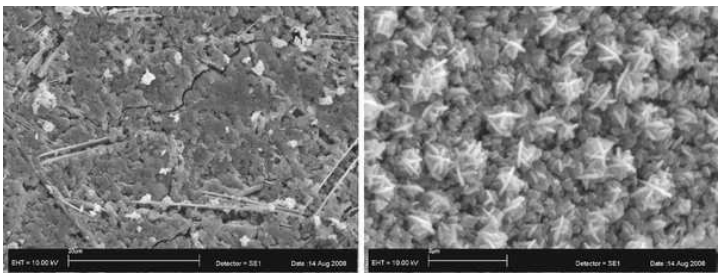

Figure 3.10: Internal pore surface SEM image of samples synthesized using a combination of sodium hydroxide (NaOH) and sodium-silicate activators[122].

3.5 EFFECTS OF CURING TIME AND TEMPERATURE

Curing time and temperature influence the compressive strength of the geopolymer concretes. Hardjito and Rangan (2005) concluded that curing for up to 24 hours improves the polymerization process and therefore results in higher compressive strength. Beyond 24 hours, the gain in compressive strength is moderate. As a result, heat curing time doesn't need to be more than 24 hours in practical applications [49].

In a study by Zhang et al. (2009), four geopolymer samples using metakaolin and sodium hydroxide (NaOH) were prepared, and the amount of crystalline phase at different times was determined using the Rietveld method (Figures3.11,3.12). Sample with $Si/Na = 4/4$ (S3) formed significant quantities of $Na-A$ Zeolite ($Na_{96}Al_{96}Si_{96}O_{384}.216H_2O$) after 1.5 days. The amount of this phase steadily increases, reaching 90% after 10 days. The sample with a lower amount of sodium, $Si/Na = 4/3$ (S2), formed smaller amounts of $Na-A$ zeolite more slowly after 3 days. Further reduction of sodium to $Si/Na = 4/2$ only produced 1.2% $Na-A$ zeolite in 10 days. Higher sodium levels ($Si/Na = 4/6$) in sample S4 caused rapid crystallization of an unnamed hydrosodalite-type zeolite ($Na_6[AlSiO_4]_6.4H_2O$). In about 2.5 hours, the amount of this crystallite reaches about 50% and remains at this level thereafter. A ratio of Si/Na =4/4 facilitates the formation of $Na-A$ Zeolite, while excess sodium hydroxide (NaOH) ($Si/Na > 4/4$, as in S4) reduces the crystallinity due to the rapid formation of large numbers of nuclei that hinder their growth into crystals. The addition of sodium silicate in small amounts in samples S5 ($Si/Na = 4/3.22$) and S6 ($Si/Na = 4/3.97$), compared with samples S3 ($Si/Na = 4/3$) and S4 ($Si/Na = 4/4$) caused the S5 and S6 samples to be about 100% amorphous (Figure3.12)[122].

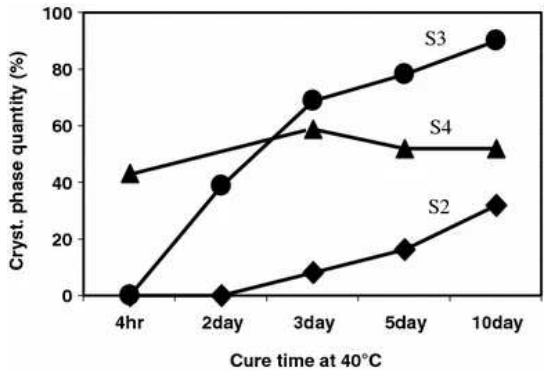

Figure 3.11: Metakaolin geopolymer curing time versus amount of crystallin phase formed with different amounts of sodium hydroxide (NaOH)[122].

3.6 COMPRESSIVE AND FLEXURAL STRENGTH

Figure3.13a illustrates the compressive and flexural strength of alkali-activated concretes of various precursors such as fly ash, blast furnace slag, metakaolin, and their combination at ages of 4 hours to one year, with the relationship based on the ordinary Portland cement specified in ACI 318-02. It is known that concretes are strong in compression but weak in flexion and tension. The American Concrete Institute standard specifies the relationship between compressive (σ_c in MPa) and flexural strength (σ_f in MPa) as a power law relationship as $\sigma_f = 0.6\sigma_c^{0.5}$[1]. Many alkali-activated materials show higher flexural strength than the specified relationship of Portland cement concretes (Figure3.13a)[92].

It is important to note that the kaolinite calcination temperature has an important effect on the metakaolin geopolymer compressive strength [115]. The compressive strength of metakaolin-based geopolymers increased for the samples that were calcined between 500 and 700 °C but dropped above 700 °C [39]. It is also important to avoid too long calcination times, as this results in grain growth transformation into mullite. Geopolymers with mullite exhibit lower compressive strength than metakaolin geopolymers [115]. Figure3.13b shows the compressive strength of the geopolymers of metakaolin. In this study, metakaolin reacted with sodium oxide(Na_2O) and silicon dioxide(SiO_2). The point on the graph with Si/Al = 1.15 is metakaolin with only sodium hydroxide (NaOH) solution, and Si/Al = 2.15 is metakaolin with a solution of composition Na_2O/SiO_2 = 2.0 ratio.

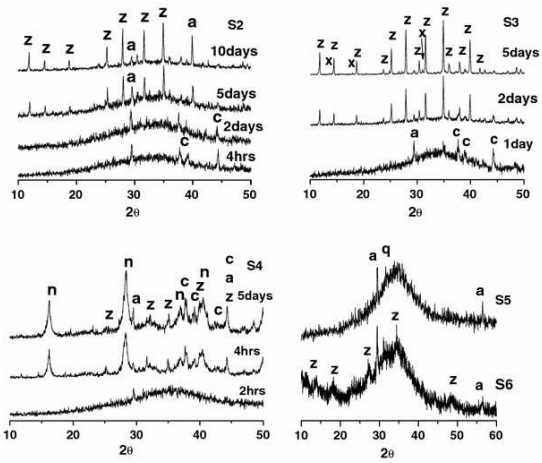

Figure 3.12: XRD pattern for metakaolin samples with different amounts of sodium hydroxide (NaOH). a (anatase) and q (quartz) are related to the impurities: z zeolite Na-A hydrate ($Na_{96}Al_{96}Si_{96}O_{384} \cdot 216H_2O$ (PDF 39-0222)), x zeolite Na-X hydrate ($(Na_{88}Al_{88}\ Si_{104}O_{384} \cdot 220H_2O)$ (PDF 39-0218)), n unnamed zeolite hydrate ($Na_6[AlSiO_4]_6 \cdot 4H_2O$ (PDF 42-0216)), c ($Na_2CO_3 \cdot H_2O$ (PDF 08-0448)) [122].

The figure shows a maximum in compressive strength at high silica content[90].

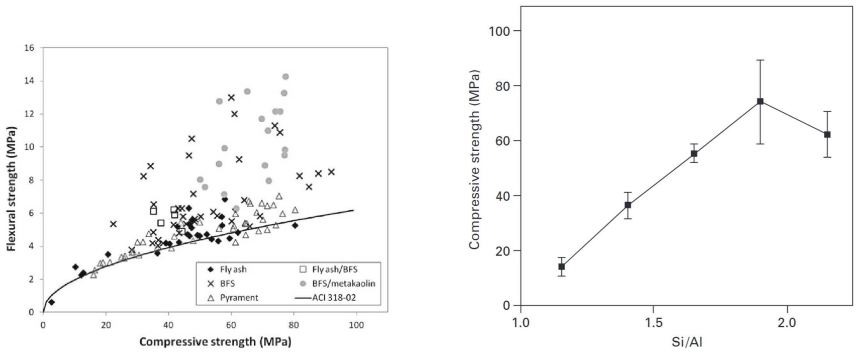

(a) (b)

Figure 3.13: (a) Comparison of compressive and flexural strength of alkali-activated concretes of various precursors, at ages of 4 hours to one year, with the relationship based on the ordinary Portland cement specified in ACI 318-02, alkali activated data from[14, 15, 17, 25, 32, 48, 55, 78, 98, 107, 118], and (b) compressive strength of metakaolin geopolymers. Metakaolin is reacted with sodium oxide (Na_2O) and silicon dioxide (SiO_2). Si/Al = 1.15 is metakaolin with sodium hydroxide (NaOH) solution, and Si/Al = 2.15 is metakaolin with a solution of composition Na_2O/SiO_2 = 2.0 ratio [90].

4

DESIGN OF THE EXPERIMENT

4.1 INTRODUCTION

Developing a model that relates important input variables to the system's responses can be used for decision-making and system improvements. A well-defined model based on experimental observations is called an empirical model. A process or system, as shown in Figure4.1, can transform inputs into outputs that have observable response variables, while some variable properties are controllable and some are not[80].

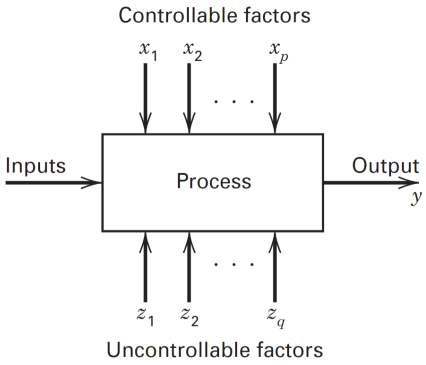

Figure 4.1: A general model of the system[80].

4.2 ONE FACTOR AT A TIME

There are different strategies for the execution of the experiments. One common practice is the One Factor at a Time (OFAT) strategy or One Variable at a Time (OVAT), in which one factor varies over its range while the other factors are held constant. This strategy not only fails to consider the interactions between the factors but also needs a lot of resources, such as time and money, to perform experiments over each factor's variability range[16]. When dealing with systems with many factors, the appropriate strategy is to use factorial or fractional factorial experiments in which factors or a subset of the factors are varied together instead of one factor at a time [80].

4.3 DESIGN OF THE EXPERIMENT

When dealing with problems that are subject to experimental errors, statistical methods are the only objective analysis approach. Since the effects of variables can be dependent, univariate statistics may fail, and instead, multivariate optimization schemes are used to overcome this shortcoming[41].

Common terms in the statistical design of the experiment are[16]:

- Factors
  Factors are the experimental independent variables whose values change during the experiment.
- Responses
  Responses are experimentally dependent variables whose values are measured during the experiment.
- Levels of the factors
  Levels are different values of a factor during an experiment.
- Experimental domain and design definition
  The experimental domain is the field that must be investigated through the experiment. A design matrix is a matrix of different combinations of factor levels.
- Residuals
  The difference between the calculated and experimental results for a set of conditions.

Usually, the main reasons to run an experiment are to screen the factors, optimize, and confirm the desired responses [80].

- Factor screening

  It is essential to narrow down the number of factors that are influencing the responses when there is a lack of in-depth understanding of the system[38]. Practically, it is impossible to identify the small contribution of many factors. Therefore, it is important to only select the variables with major effects. In factor screening, the range over which the best results are obtained should be considered relatively large[80].

- optimization

  If the main factors that influence the system are relatively known, finding the levels of the factors that lead to a desirable response value is essential[16].

- Confirmation

  To confirm the system's operation based on previous experience or theory, it might be necessary to use confirmation experiments to verify the results[80].

4.3.1 *Factorial design*

Factorial designs are the most efficient type of experiment to study the effects of two or more factors. In factorial design, in each replicate of the experiments, all possible combinations of the factors are investigated. In contrast to the OFAT experiment design strategy, the factorial design helps the investigation of interactions between the factors[74].

As shown in Figure4.2, the relative efficiency of factorial design over OFAT design increases with the increase in the number of factors. Furthermore, factorial design allows the investigation of the effects of a factor at several levels of other factors[80].

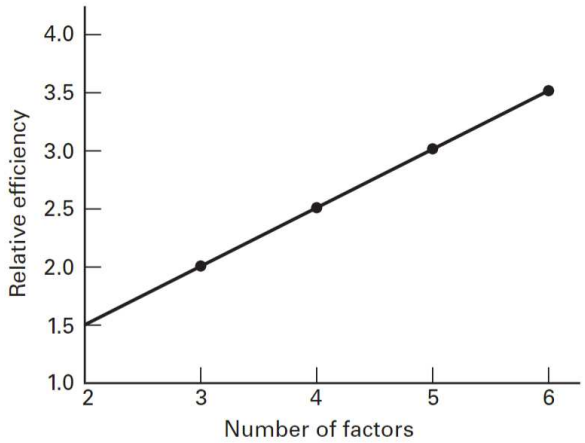

Figure 4.2: Relative efficiency of the factorial analysis to one factor at a time experiment for two level factors[80].

A special case of factorial design is called two-level factorial design, which is widely used in research. It is when the k factors have only two levels.

An assumption for using this method is that we think the response is approximately linear over the range of the chosen

factor levels. If three factors (A, B, and C) are investigated at two levels in an experiment, the design is called a 2^3 factorial design. Eight treatment combinations can be thought of as a cube, as shown in Figure4.3. The "+" and "−" are the orthogonal coding used to create the design matrix. "+" and "−" represent the high and low levels for each factor, respectively[80].

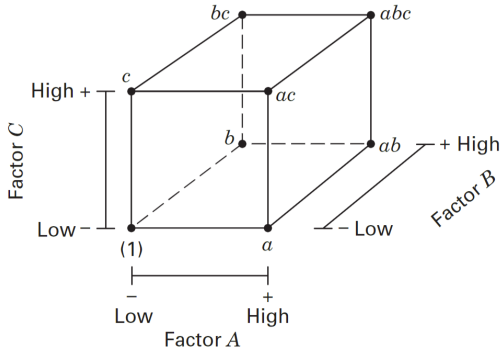

Run	Factor A	B	C
1	−	−	−
2	+	−	−
3	−	+	−
4	+	+	−
5	−	−	+
6	+	−	+
7	−	+	+
8	+	+	+

Figure 4.3: 2^3 Factorial design, left geometric view, right design matrix[80].

4.4 RESPONSE SURFACE

Response surface methodology is a multivariate technique that is used in analytical optimization. This method is a collection of statistical and mathematical techniques and tries to describe the response behavior by fitting polynomial equations to the data. Response surface methodology can be utilized when the response or responses are influenced by several factors. The most common second-order designs are the three-level factorial design, the Box-Behnken design, and the central composite design [16]. A second-order empirical model is needed to evaluate the curvature; therefore, the polynomial function must contain quadratic terms, as in the equation below.

$$y = \beta_0 + \sum_{i=1}^{k} \beta_i x_i + \sum_{i=1}^{k} \beta_{ii} x_i^2 + \sum_{1 \le i \le j}^{k} \beta_{ij} x_i x_j + \epsilon$$

In this equation, y is the dependent variable, β_0 is the intercept, x_i are the independent variables, β_i are the coefficients of the independent variables, β_{ii} are the coefficients of the squared terms of the independent variables, β_{ij} are the coefficients of the interaction terms between the independent variables, and ϵ is the error term. Using the quadratic model, maximum, minimum,

or saddle points can be calculated. Moreover, the visualization of the predicted model can be obtained by plotting the surface response (Figure 4.4).

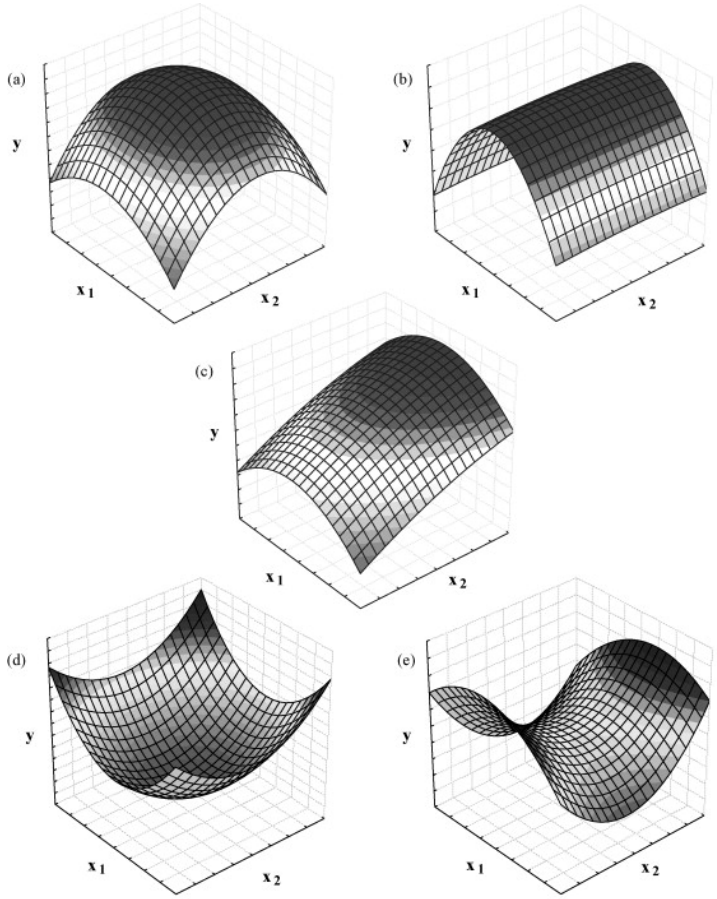

Figure 4.4: (a and b) represent surfaces where the maximum point is located inside the experimental region, while plot (c) shows that the maximum is outside the experimental region, (d) shows a minimum, and (e) shows a saddle point[16].

4.4.1 *Central composite design*

As discussed in the factorial design, there is potential concern regarding the assumption that the two-level factorial design has a linear response. To overcome this concern, the central composite design is used in response surface methodology. Central composite designs are natural extensions of two-level full or fractional factorial designs[38]. The center points will provide protection against curvature from second-order effects. In this method, center points are added to a full factorial or fractional factorial design. Figure4.5 shows geometrically the central

composite design for two and three-factor cases[69]. For the K number of factors and the C_p replicate number of center points, the number of required experiments is

$$N = K^2 + 2k + C_P$$

For this design, all factors are studied at five levels (-α, 1, 0, +1, +α), and the α value depends on the number of variables.

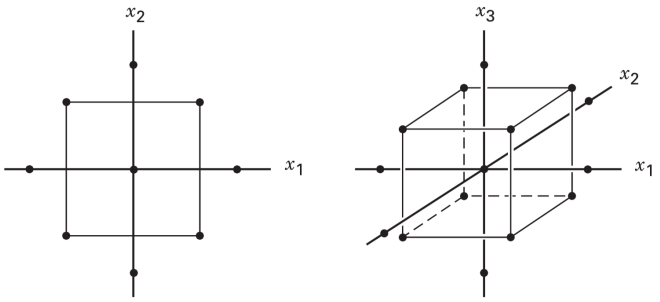

Figure 4.5: Central composite design for two factors (left) and three factors (right)[80].

4.4.2 *Desirability functions*

Using the surface response design, finding an optimal point for a single response is relatively simple. For several responses, this task is more difficult, especially if the optimal values for each response are localized in different regions or are not present under the same set of experimental conditions. The desirability function is one of the most important multi criteria methodologies used when various responses have to be considered at the same time[16]. Desirability function D was proposed by Derringer and Suich. In this method, the measured properties of each response are transformed into a dimensionless desirability scale between zero and one. The D-scale of zero is used for a completely undesirable response and one for a fully desired response. This transformation makes it possible to combine the results obtained for properties measured at different orders of magnitude [29].

4.5 HYPOTHESIS TESTING

Hypothesis testing, the empirical model, and residual analysis are important data analysis techniques in the design of the experiment. Hypothesis-testing frameworks are useful tools to

analyze the data from the design of an experiment. To measure the likely error and have a level of confidence in the results, statistical methods can provide guidelines about the reliability and validity of the results. Design selection involves selecting the empirical model, which describes the quantitative relationship between the response and design factors. First- and second-order polynomial models are among the most commonly used.

A statistical hypothesis is a statement either about the parameters of a probability distribution or the parameters of a model. To test a hypothesis, a random sample is taken, and the appropriate test statistics, including the chi-squared, t-test, and F-test, are computed. Then, based on the computed statistics, the null hypothesis is rejected or not. In this step, it is necessary to specify a set of values for the test statistic, which leads to the rejection of the null hypothesis. Usually, a certain value called the significance level is set for the error of rejecting the null hypothesis when it is true. Sometimes, using fixed significant level testing is inadequate because it doesn't give an idea of how far the computed value of the test statistic was in the rejection region; therefore, the p-value is commonly used.

The p-value is the probability that the test statistic will take on a value that is at least as extreme as the observed value of the statistic when the null hypothesis H_0 is true. In other words, it represents the likelihood of observing your results or even more extreme results, assuming that there's no real effect (the null hypothesis). In some cases, it is preferred to provide confidence intervals within which the value of the parameter in question would be expected to lie. These intervals have a frequency interpretation; that is, we do not know if the statement is true for this specific sample, but we do know that the method used to produce the confidence interval yields correct statements 100 (1-α) percent of the time. For example, if $\alpha = 0.05$, it is called a 95 percent confidence interval.

5

MATERIALS AND METHODS

5.1 MATERIAL

5.1.1 *Activators*

A commercial solution with a SiO_2/Na_2O molar ratio of 2.6 and 36% concentration was blended with sodium hydroxide (NaOH) pellets to achieve the desired SiO_2/Na_2O ratio (Figure5.1). This ratio controls specific solutions' properties, such as pH and viscosity, as well as the total amount of sodium present in the system. As a result, it is imperative to investigate the effects of variations in this ratio on the system. The solutions were prepared 24 hours prior to the tests to equilibrate the temperature with the laboratory environment.

5.2 SAMPLE PREPARATION

LMS-1D and metakaolin were used as cementitious materials (Figure5.2). For each test, the solid portion was first weighted and then dry mixed by hand, and then the solid and liquid portions were poured into the IKA Ultra-Turrax tube disperser (Figure5.3). The mixing was done for 3 minutes at 400 rpm. The paste was then directly (~1 minute) transferred to the rheometer, and the flow curves were measured.

For the purpose of preparing samples for compressive strength test, three rectangular prism molds measuring 15*15*60 mm were used for each experiment (Figure 5.4a). The experimental design subjects the samples to curing temperatures of 20, 40, and 60 °C. We cured the samples in the oven for 24 hours, subjecting them to 40 and 60 °C, before transferring them to a humid chamber at 20 °C. The samples that underwent 20 °C curing were directly transferred and cured in the humid chamber. All the samples, after 24 hours of curing at different temperatures, were maintained at 20 °C for a duration of 14 days (Figure5.4b).

(a) Sodium hydroxide pellets.

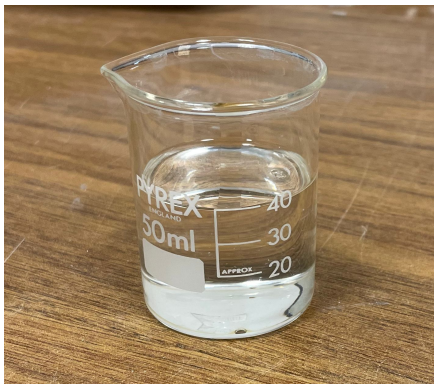

(b) Sodium silicate solution.

Figure 5.1: Raw materials for alkali activator preparation.

(a) LMS-1D sample.

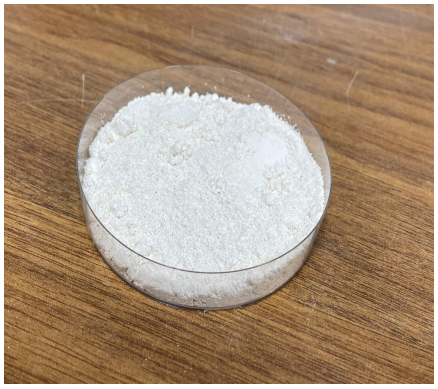

(b) Metakaolin.

Figure 5.2: Solid precursors.

5.3 DESIGN OF THE EXPERIMENT

According to the central composite design, three levels were considered for each factor. We prepared 26 samples for the rheological and compressive strength measurements. To minimize the bias, the measurements were performed in a random order. Table5.1 shows the experimental domain. The liquid-to-solid ratios were 0.4, 0.42, and 0.44. The solid part was made of 0, 7.5, and 15% metakaolin and LMS-1D Lunar regolith simulant. We used three alkali solutions with SiO_2/Na_2O ratio of 0.8, 1.2, and 1.6. The design consisted of measurements at 20, 40, and 60 °C.

Models developed in this study could predict the yield stress of the pastes and the compressive strength of the hardened alkali-activated LMS-1D Lunar regolith. To test the model's accuracy, we prepared three optimized formulations to compare the predicted values with the actual measurements in the lab.

Figure 5.3: IKA Ultra-Turrax tube disperser.

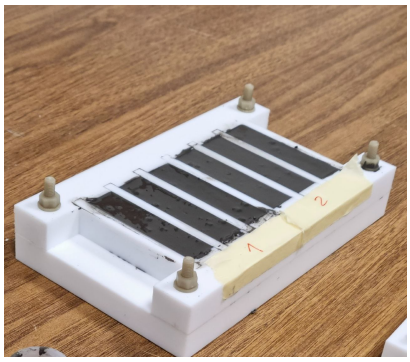

(a) Rectangular prism molds.

(b) Controls humid chamber.

Figure 5.4: Sample preparation for the compressive strength.

5.4 MEASUREMENTS

5.4.1 *Particle size characterization*

A Malvern Mastersizer Hydro EV with a dip-in centrifugal pump and stirrer was utilized for the particle size examination based on laser diffraction. The Lunar simulant sample was assessed in three replicates, and the average of all three measures was computed.

Natural Variables (x_i)	**Coded Variables**		
	-1	**0**	**1**
SiO_2/Na_2O ratio (x_1)	0.8	1.2	1.6
Liquid/Solid ratio (x_2)	0.4	0.42	0.44
Metakaolin % (x_3)	0	7.5	15
Curing temperature (°C)(x_4)	20	40	60

Table 5.1: Experimental domain.

Figure 5.5: Mastersizer Hydro EV device.

5.4.2 *X-ray powder diffraction analysis*

The electrons associated with the atoms scatter X-ray beams. This scattering causes diffraction in any crystalline material. Constructive interferences amplify the intensity of scattered radiation in particular directions, whereas destructive interferences reduce the scattered radiation in other directions. The orientation of constructive beams enables the identification of the essential characteristics of the crystalline state, including the size of the fundamental unit cell of the crystal and its symmetry. The type of atoms (atomic scattering factors) and their position in the unit cell (atomic coordinates) of a crystal dictate the intensities of diffracted rays. Atoms with a higher number of electrons demonstrate more pronounced scattering in comparison to atoms with a lower atomic number (Z). Examining the intensities of diffracted X-rays provides information on the atomic configurations within the crystal lattice. Powder diffraction is an essential technique for analyzing materials in the industrial sector. It provides a straightforward method for getting accurate experimental data. During X-ray powder diffraction investigation of multi-crystalline materials, the three-dimensional information is compressed and overlaps in one direction, resulting in a more intricate data interpretation compared to single crystal data interpretation [113]. The fundamental elements of a diffractometer in Bragg Brentano geometry consist of an X-ray source, a specimen, and an X-ray detector positioned along the

circumference of a circular structure referred to as the focusing circle (Figure 5.6a).

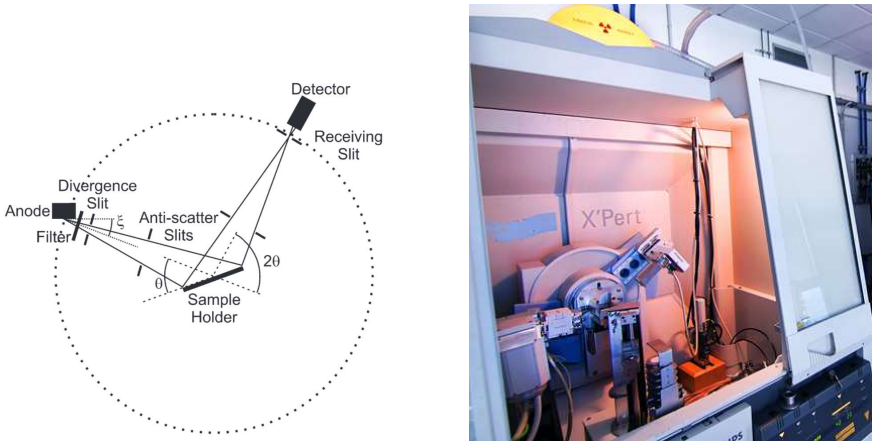

(a) (b)

Figure 5.6: (a) Bragg Brentano geometry consists of an X-ray source, a specimen, and an X-ray detector positioned along the circumference of a circular structure referred to as the focusing circle[23], and (b) PANalytical X'Pert PRO XRDP diffractometer, X-ray powder diffractometry laboratory at University of Padova.

In this study, the X-ray powder diffraction measurements were conducted by pulverizing the samples and mounting them into a 27 mm round sample holder with the inclusion of 20 weight percent zincite (ZnO) to quantify the non-crystalline component of the simulant in the Rietveld refining process. X-ray powder diffraction (XRPD) measurements were performed using a PANalytical X'Pert PRO XRDP diffractometer in Bragg Brentano geometry (Figure5.6b) equipped with a Co anode radiation tube ($K_{\alpha_1} = 1.7890, K_{\alpha_2} = 1.7929$). The diffracted beams were recorded using an X'celerator detector, and a Bragg Brentano HD optical module was used as a monochromator. The data were collected over a range of 3° to 85° 2θ with a step size of 0.017° 2θ and a nominal time per step of 100 s. Fixed divergence slits of 0.25° were used together with soller slits of 0.04 rad. All the scans were carried out in 'continuous' mode.

The Profex software[31] was utilized for both qualitative and quantitative examination of the phases. Profex serves as a user interface for interacting with the BGMN program. The profile fitting methods employed in the BGMN suite integrate the influences of X-ray's wavelengths, instrumental geometry, optics, and sample characteristics on the peak profiles throughout the

Rietveld refinement process. The BGMN software incorporates a Monte Carlo simulation method that effectively displays the aberration profiles of laboratory diffractometers [13].

5.4.3 *Scanning electron microscopy*

The primary purpose of the Scanning Electron Microscope (SEM) is to capture images at high magnification. Images are generated through the process of scanning the primary electron beam and simultaneously displaying the signal received from a secondary or backscattered electron detector. Either topographic or compositional contrast can be achieved. It is possible to attain a spatial resolution of less than 10 nm in topographic mode and less than 100 nm in compositional mode[96]. Scanning Electron Microscopes are often equipped with an X-ray spectrometer to produce certain elemental images. In the Scanning Electron Microscope (SEM), the electrons used to bombard the specimen typically have an energy of 5 to 30 kiloelectron volts (keV). This energy is dissipated through interactions with bound electrons and the lattice, collectively referred to as 'inelastic scattering'. The deceleration of electrons when they collide with solid materials is mostly caused by "inelastic" interactions with the outer atomic electrons. On the other hand, elastic interactions with atomic nuclei result in significant deflections from the original path of the electrons. However, the transfer of energy is minimal due to the substantial mass of the nucleus in comparison to the electron. Elastic scattering results in the deflection of electrons in various directions upon entering the sample, with certain electrons undergoing Bragg reflection via atomic planes within crystalline materials.

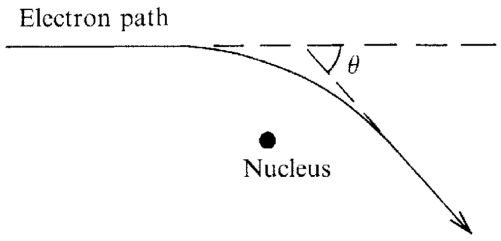

Figure 5.7: Incident electron deflection is caused by the attractive force experienced in passing close to a positively charged nucleus[96].

There is a limited chance that an electron be redirected at an angle exceeding 90 degrees and come out of the target's surface.

The proportion of incoming electrons that exit the specimen in this manner is referred to as the backscattering coefficient (η) and is heavily influenced by the atomic number. Secondary electrons, which are electrons that are expelled from the specimen, can be differentiated from backscattered electrons due to their significantly lower energy. Only electrons that originate within a few nanometers of the surface can escape as secondary electrons. Several secondary electrons are generated by incoming electrons upon entering the specimen, whereas others are produced by backscattered electrons upon emerging (Figure5.8). Both the electrons that are backscattered and the electrons that are dislodged from the surface of the sample are utilized to create an image[96].

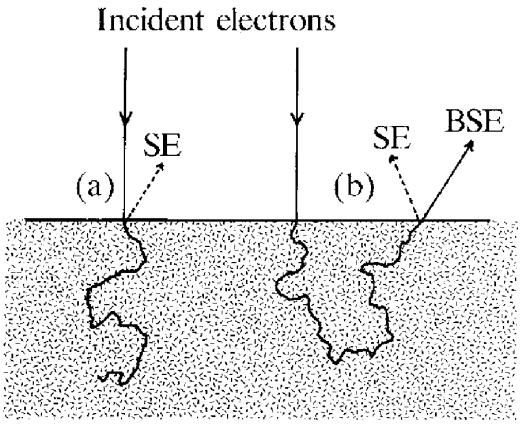

Figure 5.8: Secondary electron (SE) production: (a) via incident electrons entering the target; and (b) via backscattered electrons (BSE) exit[96].

5.4.3.1 *Electron Microprobe Analysis*

Electron Microprobe Analysis (EMPA), also known as Electron Probe Microanalysis (EPMA), is a method used to chemically analyze specific regions of solid samples. This technique involves using a concentrated electron beam to stimulate the emission of X-rays. The X-ray spectrum exhibits distinctive lines that correspond to the elements present in the sample. Therefore, it is possible to perform a qualitative chemical analysis by identifying these lines based on their wavelengths or photon energies. Quantitative determination of element concentrations can be achieved by comparing their intensities with those emitted from reference samples. It is possible to achieve accuracy close to ±1% and detection limits as low as tens of parts per million

(ppm) by weight. Typically, the spatial resolution is constrained to approximately 1 μm due to the dispersion of the beam within the sample. The spatial distributions can be documented as line profiles or two-dimensional maps, typically visualized using a false color scale to depict the concentrations of the elements. The determination of all elements with atomic numbers greater than 3 can be achieved with varied degrees of accuracy[96]. Electron bombardment in certain types of samples stimulates the emission of light, a phenomenon known as cathodoluminescence (CL). Electrons in a non-metallic material can excite other electrons by elevating them from the valence band to the typically vacant conduction band. These excited electrons then revert to their initial state through one or more steps. Excess energy can be dispersed through the release of photons (Figure5.9). The wavelengths of the light fall within the visible region, occasionally reaching into the ultraviolet or infrared ranges[96]. In

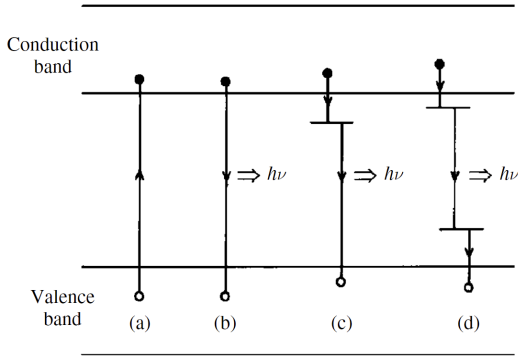

Figure 5.9: Cathodoluminescence: de-excitation (a) direct; (b) via localized levels in the band gap; (c) and (d) the photon energy (hν) difference between the initial and final levels[96].

this study, the energy dispersive spectroscopy scanning electron microscopy (EDS-SEM) measurements were conducted using a dual-beam Tescan SOLARIS scanning electron microscope equipped with an Oxford Instruments microanalytical system with 15 keV energy and 3 nanoamperes of beam current at the department of Geoscience at the University of Padova.

5.4.4 *Rheology*

Rheology explores how matter deforms and flows. It investigates how material properties and proportions influence parameters such as yield stress and viscosity. Furthermore, rheology aids in optimizing and achieving the desired flow characteristics[7].

A common method to study the rheological behavior of cementitious paste is based on the relationship between shear stress and shear rate. Due to the presence of particles with a wide range of dimensions and shapes, this task for cement-based materials is challenging. Moreover, the ongoing chemical reactions and shear history contribute to this complexity. Common measurement geometries for cement paste rheology include concentric cylinders, vane geometry, cone, and parallel plate geometries. Key rheological properties under examination encompass static and dynamic yield stress, and viscosity [121].

5.4.4.1 *Viscosity*

The fluid's resistance to an increase in flow rate is known as viscosity. Fluids that exhibit a linear relationship between shear stress and shear rate are called Newtonian fluids[121]. The dynamic viscosity of a Newtonian fluid (μ_d), such as water, at a constant temperature and pressure can be defined as the constant of proportionality of the shear stress (τ) to the shear rate ($\frac{du_x}{dy}$). Equation 5.1 shows the mathematical formulation of Newton's law of viscosity[58].

$$\tau = \mu_d \frac{du_x}{dy} \tag{5.1}$$

The viscosity of cement-based fluids depends on a combination of multiple parameters that are dominant at different scales. Viscosity is related to the solid volume fraction, which can be indirectly affected by the chemical composition and size distribution of particles and the temperature[102]. It is also dependent on time and shear history. Flow velocity increases with the decrease in viscosity; however, when the viscosity is too low, it might cause the segregation of the aggregates and cement particles during the flow[101].

5.4.4.2 *Yield Stress*

Cement-based materials are called viscoelastic materials; above the yield stress which is threshold shear stress, the material is viscous and flows, and for low strains in the order 10^{-4}, the paste behaves as ideal elastic [121]. Once the yield stress is surpassed, the cement-based material shows steady-state flow behavior [97].

Yield stress occurs because of particle interactions in the fluid and the network of cementitious particles that build up with time[101]. The static yield stress is the amount of stress needed to initiate the flow of the material and breakage of the bonds between cementitious materials. The dynamic yield stress is related to an unstructured flow of the material in which the cementitious material bonding network is already totally or partially broken down by the shearing. The dynamic yield stress determines the time when the flow of cementitious material will stop[121].

5.4.4.3 *Herschel-Bulkley behavior*

Many fluids do not exhibit a constant viscosity. For these fluids, a power law model applies(Equation5.2).

$$\tau = K\dot{\gamma}^n \tag{5.2}$$

A flow consistency factor (K) is introduced as a multiplier to the shear rate, and a consistency index (n) is the exponent of the shear rate, which describes how much the flow behavior deviates from Newtonian flow. If the viscosity is reduced with increasing shear rate, (n < 1) The corresponding flow behavior is called shear thinning. For fluids whose viscosity increases with increasing shear rate (n > 1), the flow behavior is called shear thickening [101]. Fluids with yield stress that do not have a constant viscosity coefficient are typically described by the Herschel-Bulkley law, which is described by Equation5.3.

$$\tau = \tau_0 + K\dot{\gamma}^n \tag{5.3}$$

This law is equal to the power law model relation with the yield stress(τ_0)[127]. Herschel-Bulkley can model the flow behavior of increasing and decreasing viscosities. Since most cementitious systems show yield stress, the flow behavior in these systems can be described with the Herschel-Bulkley model[101]. Figure5.10 illustrates the flow curves of Newtonian, Bingham, and Herschel-Bulkley fluids.

It is important to consider the range over which the shear rate is observed; as shown in Figure5.11 at low shear rates, van der Waals forces dominate the interactions between the particles due to surface charge interactions and short particle distances. On

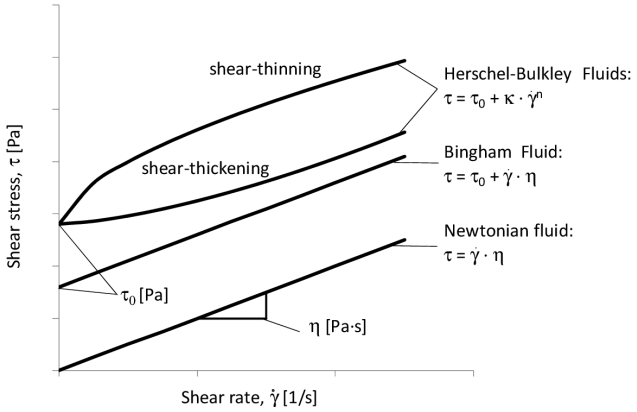

Figure 5.10: Qualitative representation of flow curve models[100].

the other hand, at high shear rates, the cement paste behaves as a Newtonian fluid, and at some point, the fluid may not be able to overcome the inertia of particles, which causes a shear thickening effect. The shear thickening effect can be prominent in concrete, in which particles have a higher volume fraction [53].

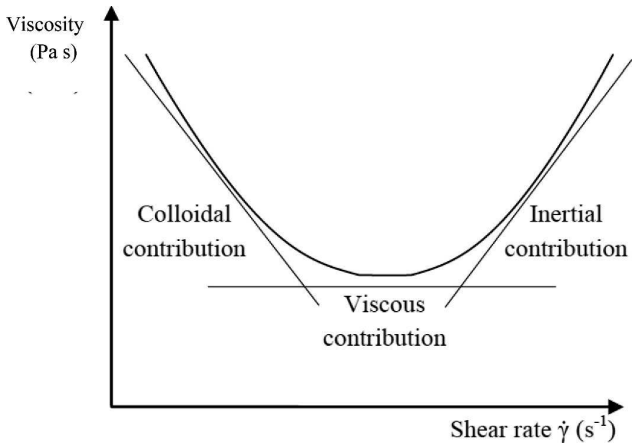

Figure 5.11: Shear rate dependency on the flow behavior of cementitious pastes[53].

5.4.4.4 *Rheometer geometry*

There is an increasing number of measurement methods available for the rheological measurement of cement-based materials, including concentric cylinders, cone-plate, plate-plate, and vane geometries. The simplest geometry would be two plates that slide over each other, but it is not practical; therefore, rotating plate rheometers were designed to approximate the shearing plane. De Lerrard et al. developed a parallel plate rheometer,

which is called BTRHEOM [127]. Parallel-plates rheological measurement is a common method used to evaluate fresh cement-based materials[70],[3]. The geometry of the parallel rotating plates is shown in the Figure5.12. The outer edge of the rheometer has a radius of R_o. The bottom plate is stationary, while the top plate rotates at angular velocity ω [rad/s] and registers the applied torque T [Nm]. The term h is the distance between the two plates[87].

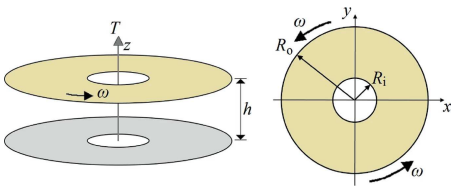

Figure 5.12: Sketch of the parallel rotating plate reometer[87].

The gap thickness value can range from 2 to 10% of the plate diameter (2R). The use of a larger gap increases the risk of edge failure. In this geometry, the shear rate is not constant across the rotating plane radius, and the circumferential velocity depends on the distance from the axis of rotation[121].

5.4.4.5 *Flow-curve measurement*

An Anton Paar MC92 device was used to perform the rheological measurements (Figure5.13). This device can operate in stress-controlled, rate-controlled, and strain-controlled modes. In this study, stress-controlled measurement was used.

To minimize the wall slip effects, a serrated plate-plate system with a 1.5 mm gap distance is used(Figure5.14). For the correct measurement, the samples were placed on the bottom plate, and then the top plate was moved to the trim position. At this stage, excess material is trimmed, and the measurement starts. Since measurements were carried out at three different temperatures, the built-in temperature device and temperature hood were used to control the temperature and minimize evaporation.

In the first step, the paste sample was pre-sheared for 30 seconds at 100 s^{-1} constant shear rate to cause structural breakdown and create a uniform condition for testing. In the second step, the sample was subjected to a constant oscillatory shear strain of 0.0001 % with a constant 1 Hz frequency for 2 minutes. in the third step, the sample was sheared from 0 to 10 s^{-1} within 2 minutes and 30 seconds to produce the up-curve of the flow test. Finally, the cement paste sample was sheared from 10 to 0 s^{-1}

Figure 5.13: Anton Paar MC92 rheometer.

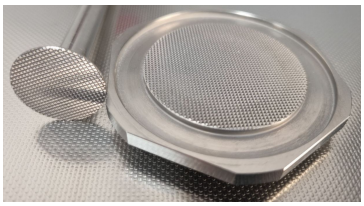

Figure 5.14: Serrated plate-plate measurement geometry.

within 2 minutes and 30 seconds to produce the down-curve of the flow test.

To model the yield stress, shear stress measurement of the shear rate ramp down from 10 to 0 s^{-1} was used. A threshold of 0.01 s^{-1} shear rate was used to exclude the very low shear rate measurements. We fitted the Herschel-Bulkley model to each measurement using Matlab software. Yield stress was calculated based on the mathematical model at a 0 shear rate value (Figure5.15).

5.4.5 *Compressive strength*

As explained in the section5.2, to measure compressive strength, each sample was polished to reduce surface irregularities, and then its width was accurately measured. Next, we mounted the samples in a special sample holder to record the compressive strength (Figure5.16b). The sample holder is made up of two upper and lower stainless steel rectangular prisms that transfer the force onto the sample. A Controls compressive strength

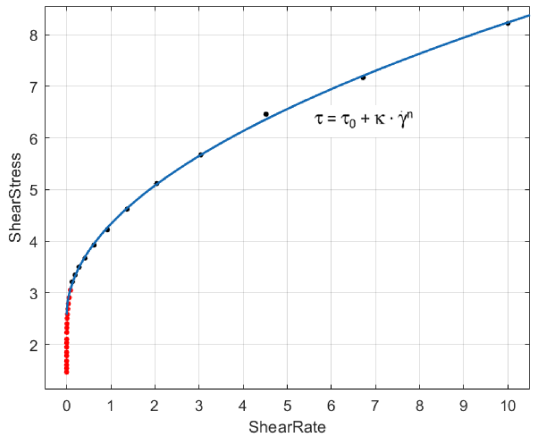

Figure 5.15: Static yield stress measurement using the Herschel-Bulkley model fitted to the experimental data.

apparatus was employed to conduct the compressive strength measurements (Figure5.16a).

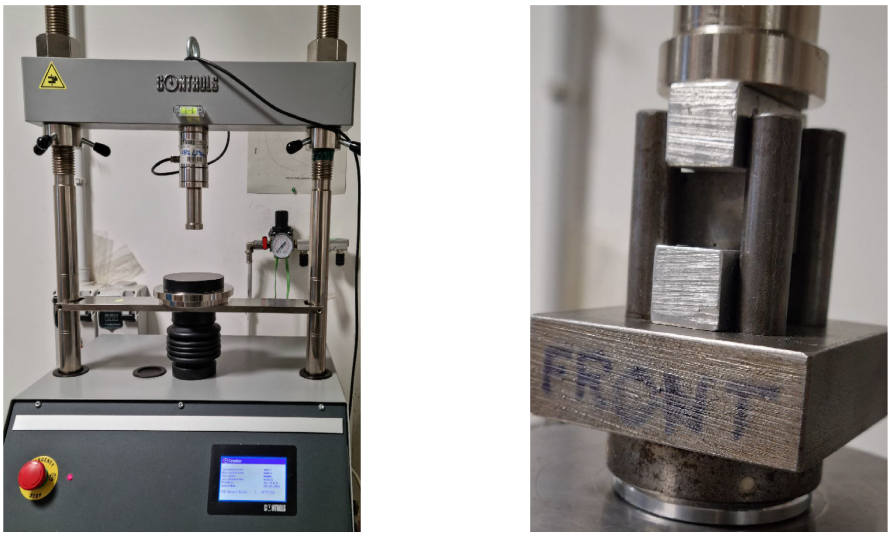

(a) (b)

Figure 5.16: Laboratory instruments (a) Controls compressive strength apparatus; (b) sample holder for compressive strength measurements.

6 RESULTS

6.1 LUNAR REGOLITH SIMULANT

6.1.1 *Particle size characterization*

The LMS-1 and LMS-1D Lunar simulant particle size analysis statistics, volume density function, and cumulative volume distribution are shown in Table6.1, Figures6.1, and 6.2, respectively. LMS-1D median particle size is about 3 μm, and the D(90) value shows that 90 % of the particles are below 22 microns. The LMS-1D volume density distribution function shows a bi-modal distribution of fine and very fine particles.

	LMS-1(μm)	LMS-1D(μm)
D [3:2]	37,4	0,1
D [4:3]	187,7	14,6
Dv (10)	18,7	0,0
Dv (50)	106,0	3,0
Dv (90)	482,6	22,3

Table 6.1: LMS-1 and LMS-1D particle size analysis.

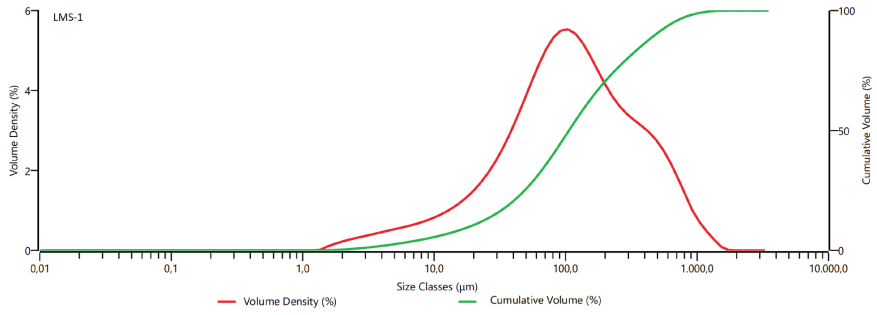

Figure 6.1: Particle size distribution of LMS-1.

6.1.2 *Chemical and mineralogical composition*

Quantitative phase analysis of the LMS-1D Lunar simulant using the Rietveld method (Figure 6.3) reveals that this sample primarily consists of plagioclase, pyroxene, and olivine. Minor

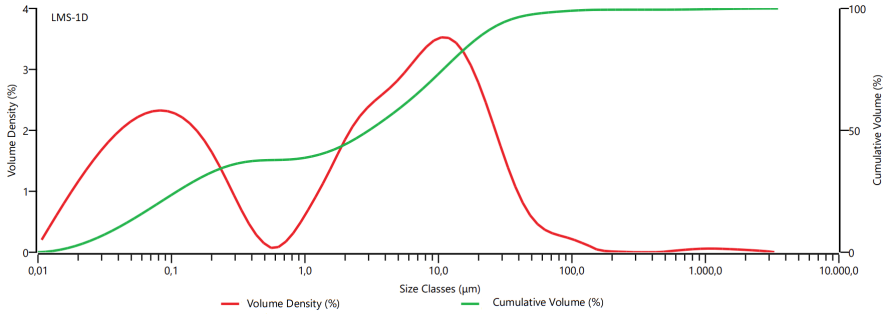

Figure 6.2: Particle size distribution of LMS-1D.

phases as talc, amphiboles, quartz, and phyllosilicates are also present (Table6.2). We estimated the amorphous content to be about 10%.

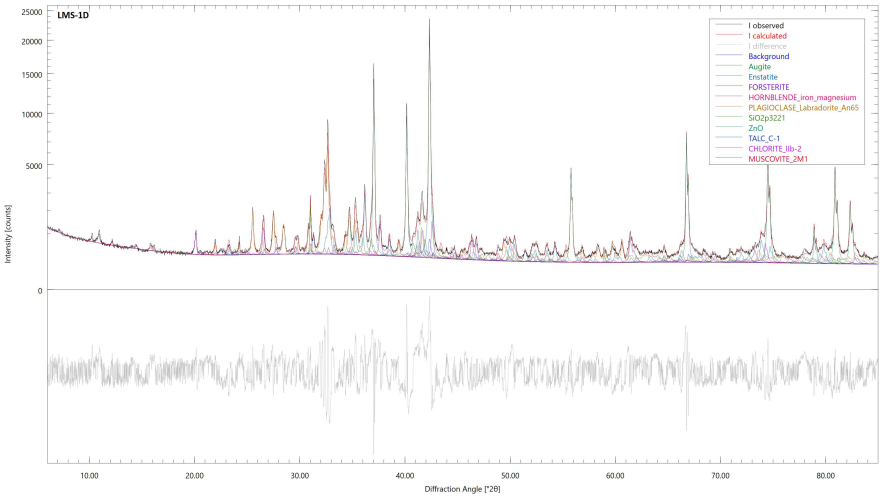

Figure 6.3: LMS-1D quantitative phase analysis using the X-ray powder diffraction analysis.

The relative abundances of oxides and trace elements in the LMS-1 and LMS-1D samples are shown in Table6.3 and 6.4, respectively. The main oxides in the extra-fine Mare region dust simulant (LMS-1D) are SiO_2 (47.24 %), MgO (15.9%) and Al_2O_3 (13.06%), respectively.

6.1.3 *Scanning electron microscopy*

To have a more detailed information of the elements distribution and to confirm the results of the XRD analysis two compositional maps were acquired for the LMS-1D Lunar regolith simulant using energy dispersive X-ray spectroscopy.

Phase	Wt. (%)	ESD. (%)
Plagioclase	34	0.5
Enstatite	21.5	0.4
Forsterite	12.1	0.3
Augite	9	0.2
Muscovite	4	0.2
Talc	3.5	0.2
Hornblende	2.6	0.2
Quartz	1.58	0.05
Chlorite	1	0.1
Amorph	10.8	0.9

Table 6.2: Detected mineral phases and estimated standard deviation in the LMS-1D Lunar regolith simulant using X-ray powder diffraction analysis.

Oxides	LMS-1 %	LMS-1D %
SiO_2	48.62	47.24
TiO_2	2.12	3.24
Al_2O_3	12.21	13.06
Fe_2O_3	9.77	9.93
MnO	0.19	0.20
MgO	17.14	15.90
CaO	7.51	7.46
Na_2O	1.49	1.72
K_2O	0.37	0.74
P_2O_5	0.21	0.19
LOI	0.64	1.07

Table 6.3: LMS-1 and LMS-1D Lunar regolith simulants bulk chemistry. LOI indicates Loss on ignition.

Elements	LMS-1 (ppm)	LMS-1D (ppm)
S	57	56
Sc	9	8
V	155	153
Cr	1795	1650
Co	52	51
Ni	592	542
Cu	46	42
Zn	209	67
Ga	6	10
Rb	12	18
Sr	313	264
Y	17	10
Zr	183	92
Nb	20	30
Ba	287	204
La	<10	<10
Ce	22	<10
Nd	21	13
Pb	<5	13
Th	<3	<3
U	3	5

Table 6.4: Amounts of trace elements in LMS-1 and LMS-1D Lunar regolith simulants.

6.1.3.1 *Site 1*

Figure6.4a shows the mid-angle back scattered electron (BSE) image taken at 1300x magnification. The main mineral phases present in LMS-1D are amphibole (Figure6.5a), olivine (Figure6.5b), feldspar (Labradorite Figure6.5c), and ilmenite (Figure6.5d) with few grains of quartz. O, Al, and Si were assigned to the red, green, and blue bands, respectively, to create a false color map. The map illustrates olivine in reddish brown, feldspars in green, and ilmenite in dark brown (Figure6.4b).

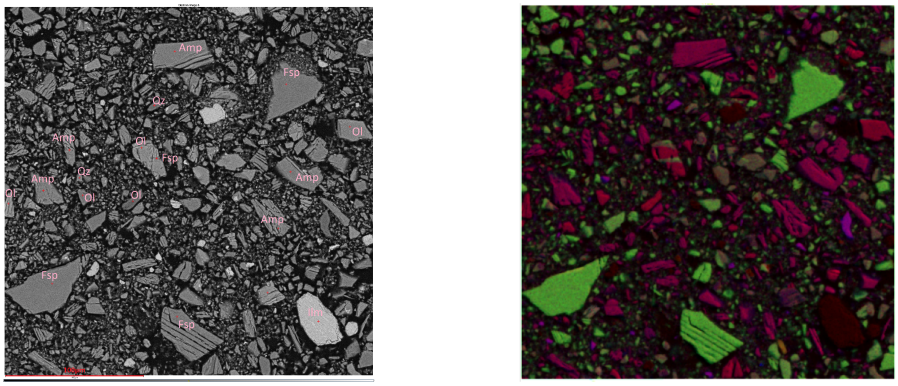

(a) (b)

Figure 6.4: (a) LMS-1D Lunar regolith mineral map Site-1; (b) false-color composite image of O, Al, and Si in red, green, and blue, respectively.

Signal intensities for the separate elements are color-mapped to distinguish the elemental variation inside the mapped site (Figure 6.6).

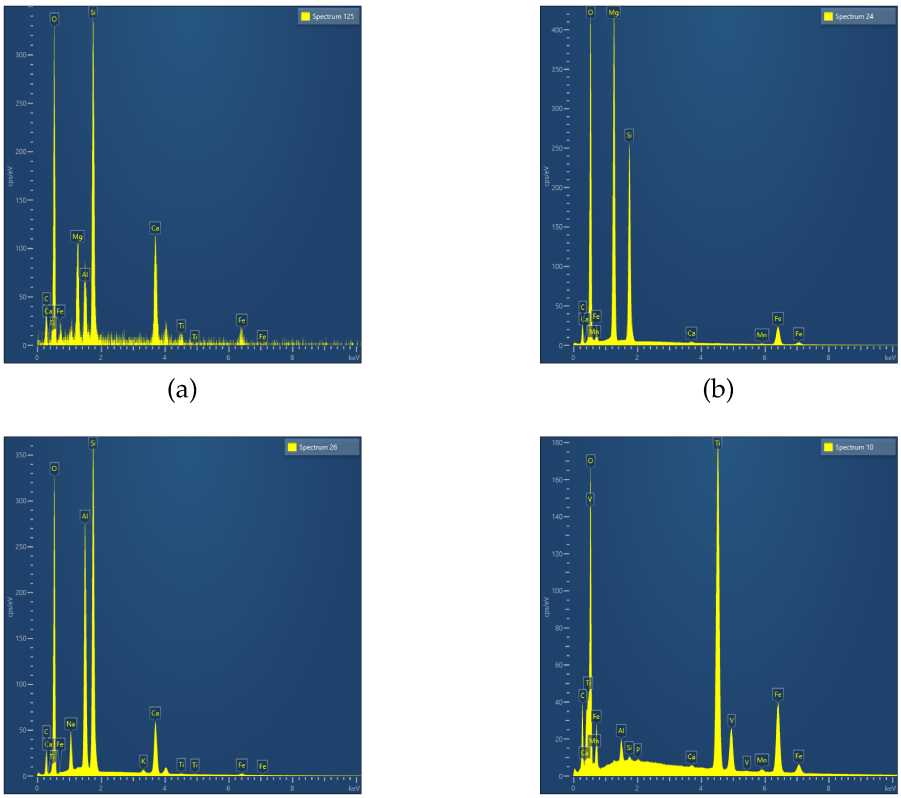

(a) (b)

(c) (d)

Figure 6.5: Spectra measured using energy dispersive x-ray spectroscopy: (a) amphibole, (b) olivine, (c) feldspar, and (d) ilmenite.

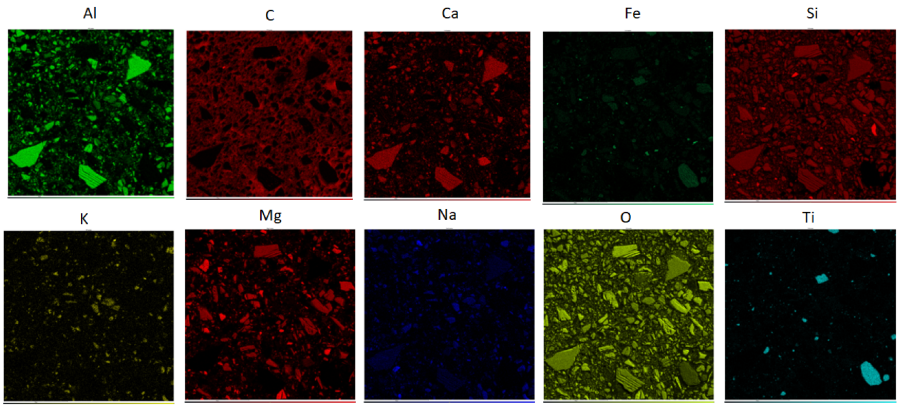

Figure 6.6: Elemental map acquired using energy dispersive X-ray spectroscopy for LMS-1D Lunar regolith site-1.

6.1.3.2 *Site 2*

Figure6.7a shows the mid-angle back scattered electron (BSE) image taken at 5000x magnification. The main mineral phases present are talc (Figure6.8) and feldspar, olivine, ilmenite. Mg, Fe, and Si were assigned to the red, green, and blue bands, respectively, to create a false color map. The map illustrates olivine in reddish, feldspars in blue, talc in purple, and ilmenite in green (Figure6.7b).

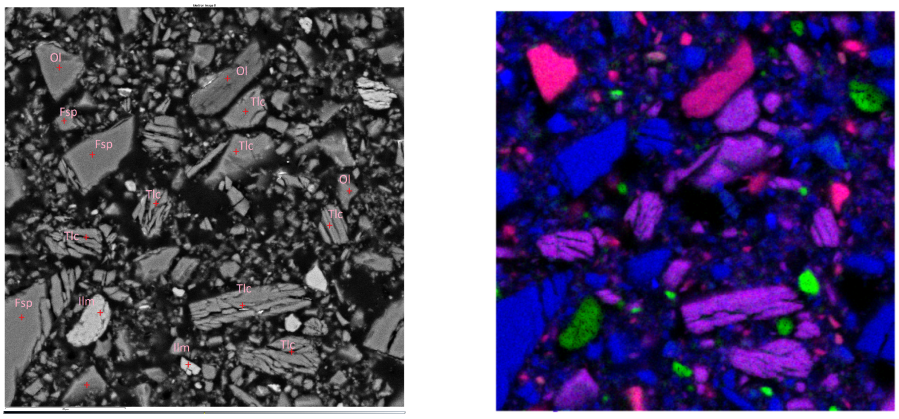

(a) (b)

Figure 6.7: (a) LMS-1D Lunar regolith mineral map Site-2; (b) false-color image of Mg, Fe, and Si in red, green, and blue, respectively.

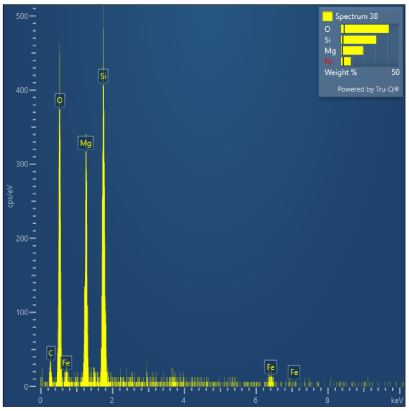

Figure 6.8: Spectra measured using energy dispersive X-ray spectroscopy of a talc mineral.

Signal intensities for the separate elements are color-mapped to distinguish the elemental variation inside the mapped site (Figure 6.9).

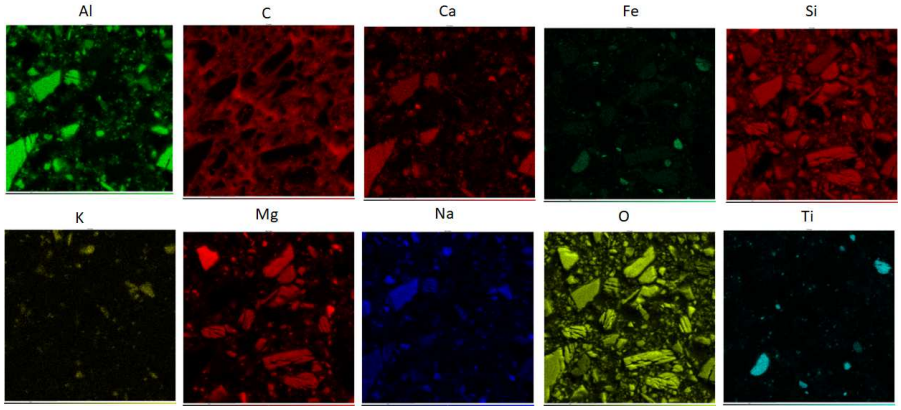

Figure 6.9: Elemental map acquired using energy dispersive X-ray spectroscopy for LMS-1D Lunar regolith site-2.

6.2 DESIGN OF THE EXPERIMENT

In this section, the effect of curing temperature, percentage of the metakaolin, ratios of liquid to solid, and SiO_2/Na_2O have been investigated on the yield stress of the alkali-activated LMS-1D Lunar regolith simulant and the compressive strength of the hardened material. We employed the response surface methodology to design the experiments. The experimental domain was chosen based on comparable works in the literature[45, 88, 89, 120, 125]. We conducted seven preliminary tests using various combinations of independent variables to define the experimental domain (Table 6.5). The lowest range was selected for the liquid-to-solid ratio, below which the paste was not workable, and above which the paste became too liquid. We chose the amount of metakaolin at the lower end, ensuring the least amount possible to measure its influence on the system. An excessive amount of metakaolin led to pastes that were not workable. The curing temperatures of 20, 40, and 60°C were selected to investigate the effect of increasing temperature on the system responses.

6.2.1 *Analysis of variance*

As discussed in the design of the experiment section5.3, 26 experiments were designed, and the yield stress and compressive strength were measured and recorded as the responses of these groups of factors. We use the ANOVA test to compare the mean responses of these different groups and determine their significance. Table6.6 and 6.7 show the results of the analysis

Natural Variables (x_i)	Coded Variables		
	-1	0	1
SiO_2/Na_2O ratio (x_1)	0.8	1.2	1.6
Liquid/Solid ratio (x_2)	0.4	0.42	0.44
Metakaolin % (x_3)	0	7.5	15
Curing temperature (°C)(x_4)	20	40	60

Table 6.5: Experimental domain.

Source	DF	Sum of Squares	Mean Square	F Ratio
Model	14	123315.34	8808.24	6.82
Error	11	14202.30	1291.12	Prob > F
C. Total	25	137517.64		0.0014

Table 6.6: Analysis of variance for the yield stress model.

of variance test on the predicted yield stress and compressive strength, respectively.

There are two source of the variation in the data. The model term has 14 degrees of freedom (DF) and the error term has 11 degrees of freedom. For each source of variation, the sum of squares (SS) shows the sum of squared deviations from the mean. The sum of squares is a measure of the total variance in the data. The mean squared (MS) shows the mean squared deviation from the mean for each source of variation. It is calculated by dividing the sum of squares by the degrees of freedom. The F-Ratio column shows the F-statistic, which is a ratio of the mean squares of the model and the error. The F-statistic is used to test the null hypothesis that the means of all groups are equal. The F-ratios for yield stress and compressive strength are associated with p-values of 0.0014 and <0.0001, respectively. This value is less than the significance level of 0.05, which means

Source	DF	Sum of Squares	Mean Square	F Ratio
Model	14	5137.28	366.94	26.64
Error	11	151.48	13.77	Prob > F
C. Total	25	5288.77		<0.0001*

Table 6.7: Analysis of variance for the compressive strength model.

that we can reject the null hypothesis. The F-ratio is statistically significant, indicating that there is a significant difference between the groups' means in the model. The p-values of 0.0014 and 0.0001 indicate that this difference is unlikely to be caused by chance.

6.2.2 *Parameter estimates*

Since the ANOVA test shows that the model is a good fit for the data, we can use a combination of significant factors to build the predictive models. Table6.8 and Table6.9 shows the results of parameter estimates for the yield stress and compressive strength models, respectively.

Term	Estimate	Std Error	t Ratio	Prob> |t|
Intercept	40.062	14.244	2.810	0.017
Si/Na(0.8,1.6)	-0.129	8.469	-0.020	0.988
Li/So(0.4,0.44)	18.697	8.469	2.210	0.049
Metakaolin(0,15)	32.046	8.469	3.780	0.003
Temp(20,60)	52.160	8.469	6.160	< .0001
Si/Na*Li/So	-2.586	8.983	-0.290	0.779
Si/Na*Metakaolin	-24.926	8.983	-2.770	0.018
Li/So*Metakaolin	24.214	8.983	2.700	0.021
Si/Na*Temp	2.249	8.983	0.250	0.807
Li/So*Temp	16.800	8.983	1.870	0.088
Metakaolin*Temp	32.815	8.983	3.650	0.004
Si/Na*Si/Na	-1.016	22.453	-0.050	0.965
Li/So*Li/So	-17.671	22.453	-0.790	0.448
Metakaolin*Metakaolin	-5.684	22.453	-0.250	0.805
Temp*Temp	50.760	22.453	2.260	0.045

Table 6.8: Yield stress parameter estimates.

For each estimated value, the standard error is shown in the tables. The "t-ratio" shows the t-statistic for each estimate. A t-statistic that is far from zero suggests that the parameter is statistically significant, meaning that it is likely not equal to zero in the population. The "Prob>|t|" column shows the p-value for each t-statistic. A small p-value, typically less than 0.05, indicates the rejection of the null hypothesis and the statistical significance of the parameter.

In the yield stress model, the terms, namely the intercept, liquid-to-solid ratio, amount of metakaolin, temperature, the interaction of the Si/Na ratio with metakaolin, the liquid-to-solid ratio with metakaolin, metakaolin and temperature, and

Term	Estimate	Std Error	t Ratio	Prob> |t|
Intercept	12.407	1.471	8.430	< .0001
Si/Na(0.8,1.6)	4.696	0.875	5.370	0.000
Li/So(0.4,0.44)	-2.134	0.875	-2.440	0.033
Metakaolin(0,15)	15.131	0.875	17.300	< .0001
Temp(20,60)	-1.317	0.875	-1.510	0.160
Si/Na*Li/So	-0.495	0.928	-0.530	0.605
Si/Na*Metakaolin	3.844	0.928	4.140	0.002
Li/So*Metakaolin	-1.905	0.928	-2.050	0.065
Si/Na*Temp	0.424	0.928	0.460	0.657
Li/So*Temp	-0.472	0.928	-0.510	0.621
Metakaolin*Temp	-2.149	0.928	-2.320	0.041
Si/Na*Si/Na	0.702	2.319	0.300	0.768
Li/So*Li/So	-3.554	2.319	-1.530	0.154
Metakaolin*Metakaolin	6.123	2.319	2.640	0.023
Temp*Temp	-0.608	2.319	-0.260	0.798

Table 6.9: Compressive strength parameter estimates.

finally the quadratic term of temperature squared, are significant. Based on the estimates of the significant parameters, the model for the yield stress can be written as Equation6.1.

$$\begin{aligned}\text{Yield stress} = {} & 40.06 + 18.69(Li/So) \\ & + 32.05(\text{Metakaolin}) \\ & + 52.16(\text{Temperature}) \\ & - 24.92(Si/Na \times \text{Metakaolin}) \\ & + 24.21(Li/So \times \text{Metakaolin}) \\ & + 32.81(\text{Metakaolin} \times \text{Temperature}) \\ & + 50.76(\text{Temperature}^2)\end{aligned} \tag{6.1}$$

For the compressive strength model, the terms, namely the intercept, Si/Na and the liquid-to-solid ratio, metakaolin, the interaction of the Si/Na ratio with metakaolin, metakaolin with temperature, and finally the quadratic term metakaolin squared, are significant. Based on the estimates provided and the signifi-

cant parameters, the model for the compressive strength can be written as Equation6.2.

$$\begin{aligned}\text{Compressive strength} =& 12.40 + 4.69(Si/Na) \\ & - 2.13(Li/So) \\ & + 15.13(\text{Metakaolin}) \\ & + 3.84(Si/Na \times \text{Metakaolin}) \\ & - 2.14(\text{Metakaolin} \times \text{Temperature}) \\ & + 6.12(\text{Metakaolin}^2)\end{aligned} \tag{6.2}$$

The liquid-to-solid ratio, the amount of metakaolin, the interaction of the Si/Na ratio with metakaolin, and finally the interaction of metakaolin with temperature are significant in both models. It is important to note that, although the Si/Na ratio is not significant for yield stress, it is important for the compressive strength of the final product. Also, the temperature and the interaction of the liquid-to-solid ratio with metakaolin are significant for the yield stress, but they don't have any effects on the compressive strength. For the yield stress, the quadratic term of temperature (temperature^2) is significant, while for the compressive strength, the quadratic term of metakaolin (metakaolin^2) is significant.

6.2.3 *Model fit*

Figure 6.10 illustrates the actual and the predicted fitted model for the yield stress and compressive strength, respectively. Table6.10 shows the summary of the fit to illustrate how well our models fit the data. The mean values for the yield stress and compressive strength are 58.33 Pa and 14.25 MPa, respectively.

R-square reports the proportion of the response's variation that the model can account for. In other words, this statistic is a measure of how well the variation in the dependent variable is explained by the independent variables in the model. An R-square closer to one indicates a better fit to the data than one closer to zero. An R-square near zero indicates that the model is not a much better predictor of the response than the response mean. The values of R-square for the predicted yield stress and compressive strength are 0.8967 and 0.9713, respectively. In other words, these R-square values mean that 89.67% and 97.13 % of the variation in yield stress and compressive strength

Statistics	Yield stress	Compressive strength
R-Squared	0.8967	0.9713
Adjusted R-Squared	0.7652	0.9349
Root Mean Square Error	35.932	3.7110
Mean of Response	58.33	14.25
Observations	26	26

Table 6.10: Summary of fit for yield stress and compressive strength.

are explained by the model. To facilitate comparisons among models with different numbers of parameters, the R-square adjusted is used. Adjusted R-square fine-tunes the R-square statistic for the number of parameters in the model using degrees of freedom. Adjusted R-square is generally considered a more reliable measure of model fit than R-square. In this table, the adjusted R-squared values for the predicted yield stress and compressive strength are 0.7652 and 0.9349, respectively. These values suggest that the models explain 76.53% and 93.49 % of the variation in yield stress and compressive strength after accounting for the number of predictors in the model. The root mean square error statistic estimates the standard deviation of the random error. This statistic is a measure of how much the predicted values from the model differ from the actual values. For the yield stress and compressive strength models, the RSME values are 35.93 and 3.71, respectively. Overall, this summary of the fit table suggests that the model provides a good fit for the data.

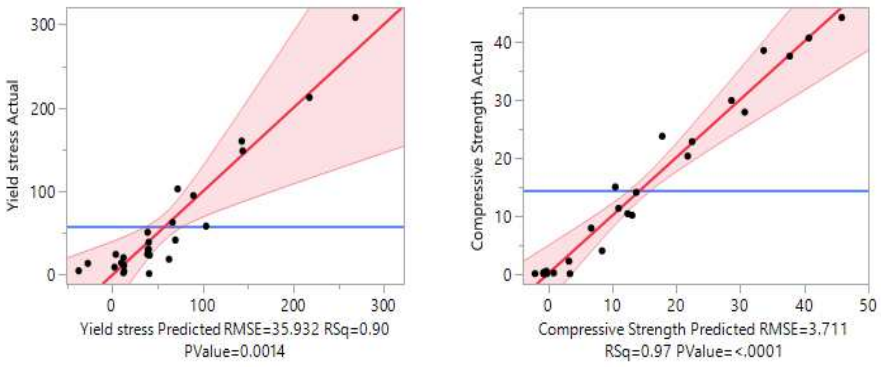

(a) (b)

Figure 6.10: The graph shows the predicted values versus actual values for yield stress and compressive strength.

6.2.4 *Response surface*

Figures 6.11 and 6.12 show the response surfaces for yield stress and compressive strength, respectively.

- Figure6.11a shows that the yield stress increases with the simultaneous increase in the amount of metakolin and liquid-to-solid ratio. At low liquid-to-solid ratios, an increase in the amount of metakaolin has a slight impact on yield stress. In contrast, at higher liquid-to-solid ratios, increasing the amount of metakaolin dramatically increases the yield stress.

- Figures 6.11b and 6.11f show that the yield stress increases with the increase in temperature at different liquid-to-solid ratios and silica-to-sodium ratios. This effect is more pronounced at high liquid-to-solid ratios. At low temperatures, yield stress reaches a maximum at about a 0.41 liquid-to-solid ratio. The same behavior is observed with the silica-to-sodium ratio, while the increase in yield stress is related to the temperature. The change in the silica-to-sodium ratio doesn't affect the behavior of the yield stress versus temperature.

- The increase in yield stress with temperature is accompanied by higher amounts of metakaolin (Figure6.11c). At low or even zero amounts of metakaolin, yield stress starts to increase at temperatures above 40 degrees. In contrast, at higher amounts of metakaolin, the increase in yield stress with temperature is sharper. The maximum yield stress occurs at the highest amount of metakaolin and at the highest temperature. The minimum yield stress is observed at 30–40 °C, with the lowest amount of metakaolin.

- Yield stress shows a maximum about 0.41 liquid-to-solid ratio, which decreases with the increase in the silica-to-sodium ratio (Figure6.11d). As the liquid-to-solid ratio decreases, yield stress decreases. Compared to metakaolin, when the silica-to-sodium ratio is low, like 0.8, the yield stress goes up from a low starting point with the increase of metakaolin. But when the silica to sodium ratio is high, like 1.6, the yield stress stays high at a high starting point and doesn't change with the metakaolin (Figure6.11e).

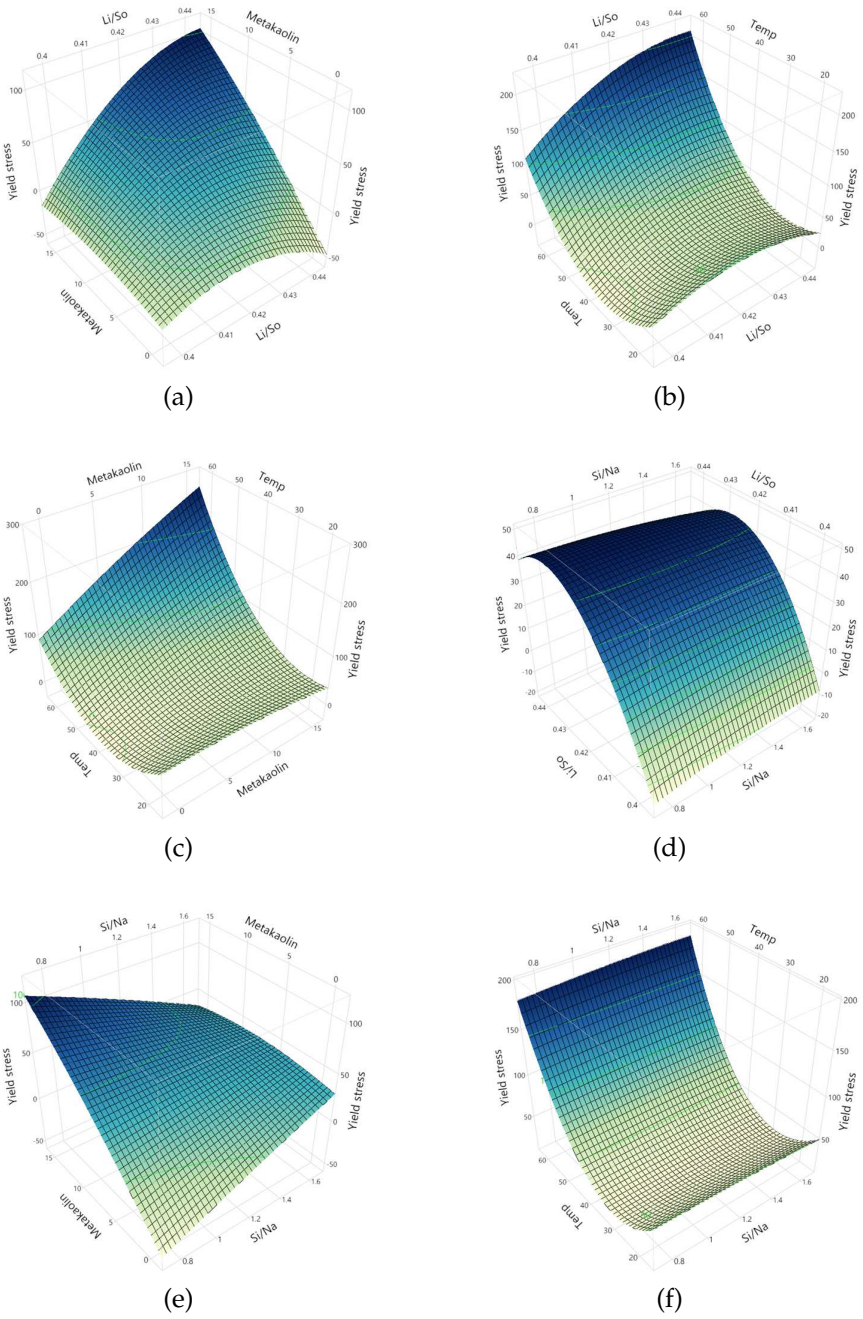

Figure 6.11: Response surfaces for the yield stress.(a) liquid/solid ratio and the amount of metakaolin; (b) liquid/solid ratio and temperature; (c) the amount of metakaolin and temperature; (d) silica/sodium ratio and liquid/solid ratio; (e) silica/sodium ratio and the amount of metakaolin; (f) silica/sodium ratio and temperature.

- At the lowest amount of metakaolin, the compressive strength in Figure 6.12a reaches its maximum at a 0.41 liquid to solid ratio. As the amount of metakaolin increases, compressive strength increases dramatically. This increase is more pronounced at the lowest liquid-to-solid ratio.

- Compressive strength increases as the amount of metakaolin increases at different temperatures (Figure6.12c). At low amounts of metakaolin, the compressive strength is indifferent to changes in temperature. However, at high amounts of metakaolin, compressive strength is highest at lower temperatures.

- Figure 6.12e shows that the silica to sodium ratio has no effect on compressive strength at low metakaolin content, but it has a significant effect at high metakaolin content. The higher the metakaolin and silica-to-sodium ratio, the higher the compressive strength.

- Compressive strength shows a slight maximum at a 0.41 liquid-to-solid ratio, and this effect is indifferent to changes in temperature (Figure 6.12b). But the silica-to-sodium ratio makes this effect of the liquid-to-solid ratio on the compressive strength stronger. This means that the higher the silica-to-sodium ratio, the higher the compressive strength (Figure6.12d). This effect of an increase in the compressive strength due to the increase in the silica-to-sodium ratio is also indifferent to the changes in temperature (Figure 6.12f).

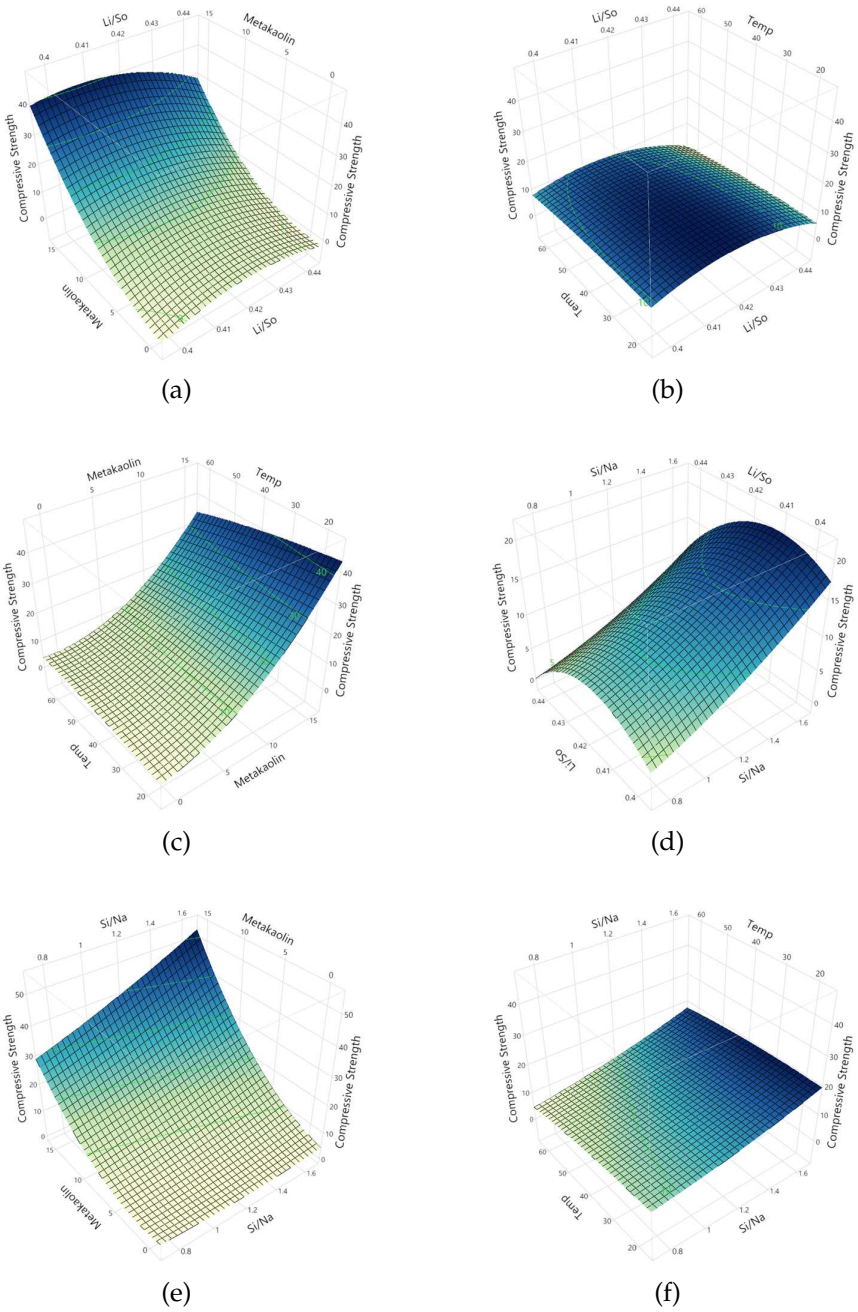

Figure 6.12: Response surfaces for the compressive strength. (a) liquid/solid ratio and the amount of metakaolin; (b) liquid/-solid ratio and temperature; (c) the amount of metakaolin and temperature; (d) silica/sodium ratio and liquid/solid ratio; (e) silica/sodium ratio and the amount of metakaolin; (f) silica/sodium ratio and temperature.

6.3 MODELS VALIDATION

Based on the models developed with the design of the experiment approach, three optimized formulations were selected to validate the models (Table6.11).

Factor	#1	#2	#3
SiO_2/Na_2O ratio	1.40	1.50	1.60
Liquid/Solid ratio	0.41	0.41	0.40
Metakaolin %	12	8.5	5
Curing temperature	20	20	20

Table 6.11: Three optimized formulations selected to validate the models.

Figures 6.13a and 6.13b illustrate three rectangular prisms of three optimized alkali-activated LMS-1D Lunar simulants and 3D printing of alkali-activated material, respectively.

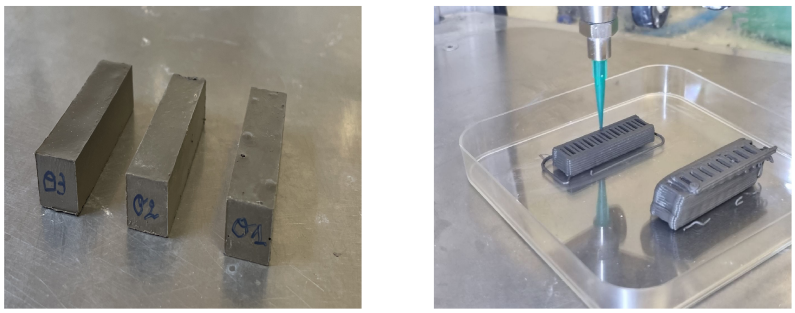

(a) (b)

Figure 6.13: (a) Final products of alkali-activated LMS-1D Lunar regolith simulant after demolding. The samples were prepared in accordance with the validation formulas, and (b) 3D printing in action: printing an intricate structure at the Department of Industrial Engineering, University of Padova.

Figures 6.14, 6.15, and 6.16 illustrate the profile of the yield stress and compressive strength versus the independent variables for the first, second, and third formulations, respectively.

Table6.12 and Figure6.17 illustrate the predicted and mean of the experimental results, their differences, and the box plot for the yield stress, respectively. The predicted yield stress values for optimized formulations 1, 2, and 3 are 15.25, 27.60, and 34.29 Pa, respectively. The experimental results for formulations 1, 2, and

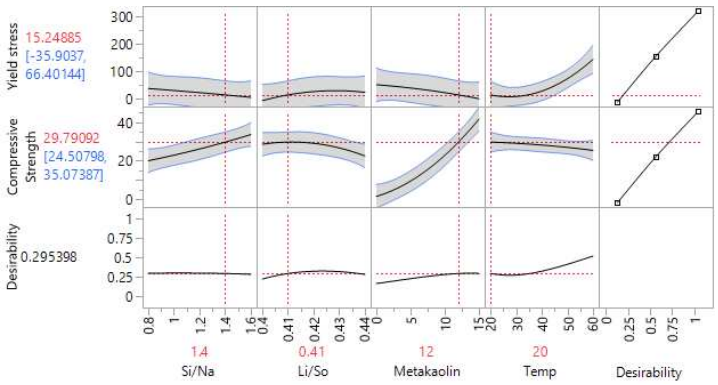

Figure 6.14: The yield stress and compressive strength response profiles versus the independent factors for the first optimized formulation.

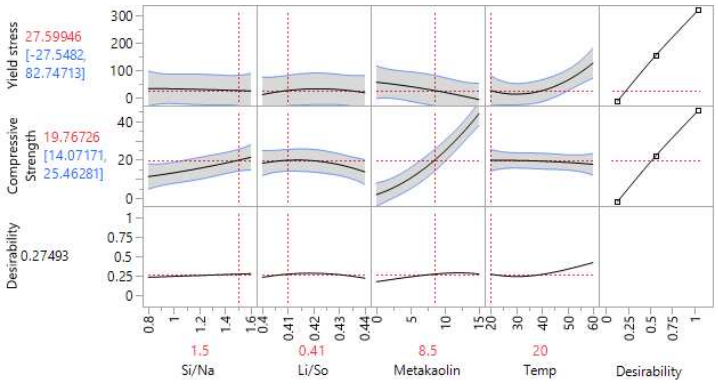

Figure 6.15: The yield stress and compressive strength response profiles versus the independent factors for the second optimized formulation.

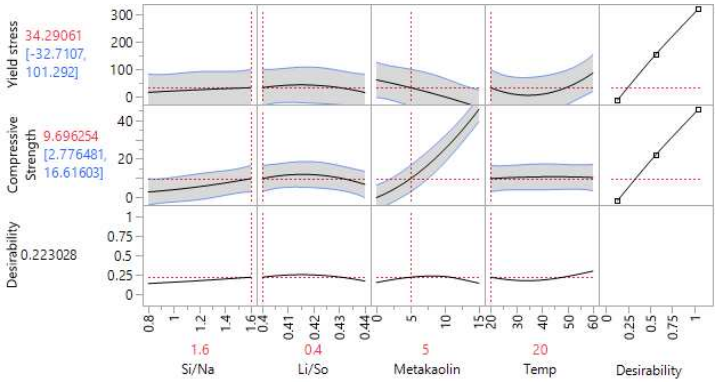

Figure 6.16: The yield stress and compressive strength response profiles versus the independent factors for the third optimized formulation.

3 are 18.72, 23.62, and 15.54 Pa, respectively. All measurements are in the confidence interval of the model.

Optimization	#1	#2	#3
Predicted yield stress (Pa)	15.25	27.60	34.29
Confidence interval (Pa)	[0.0 - 66.4]	[0.0 - 82.7]	[0 - 101.3]
Mean experimental yield stress (Pa)	18.72	23.62	15.54
Difference (Pa)	3.47	-3.97	-18.74

Table 6.12: Difference between predicted yield stress and the experimental results.

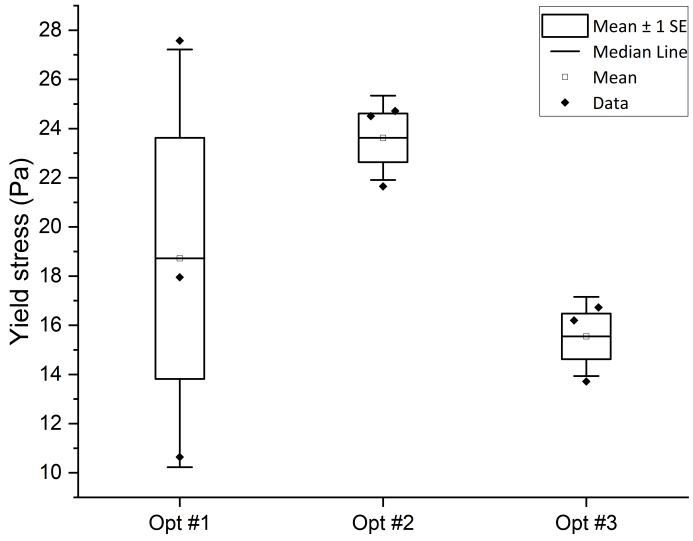

Figure 6.17: Yield stress box plot for the three optimized experiment results.

Table6.13 and Figure6.18 illustrate the predicted and mean of the experimental results, their differences, and the box plot for the compressive strength, respectively. The predicted values for optimized formulations 1, 2, and 3 are 29.79, 19.77, and 9.70 MPa, respectively. The mean experimental results for formulations 1, 2, and 3 are 34.20, 31.14, and 13.8 MPa, respectively. All measurements are in the confidence interval of the model, and they show a similar value to the predicted ones. It must be noted that the low, middle, and high experimental values are in the same order as the prediction order. The confidence intervals

Optimization	#1	#2	#3
Predicted compressive strength (MPa)	29.79	19.77	9.70
Confidence interval (MPa)	[24.5 - 35.1]	[14.0 - 25.5]	[2.8 - 16.6]
Mean experimental compressive strength (MPa)	34.20	31.14	13.8
Difference (MPa)	4.47	11.37	4.10

Table 6.13: Difference between the predicted compressive strength and the experimental results.

for the prediction model of the compressive strength have a smaller range in comparison to the yield stress, and therefore the measurements show a smaller variability (Figure6.18).

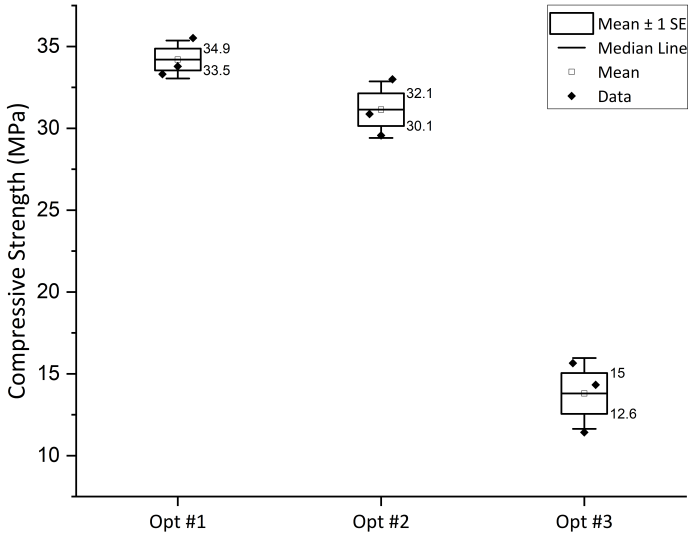

Figure 6.18: Compressive strength box plot for the three optimized experiment results.

6.3.1 *X-ray powder diffraction*

Table 6.14 shows the quantitative phase analysis of the three optimized formulation using the Rietveld method. The first sample primarily consists of plagioclase, pyroxene, and olivine. Minor phases of muscovite, quartz, and talc are also present

(Figure 6.19). We estimate the amorphous content to be around 24%.

Formulation 1			Formulation 2			Formulation 3		
Phase	Wt.%	ESD %	Phase	Wt.%	ESD %	Phase	Wt.%	ESD %
Bytownite	27.8	0.3	Bytownite	27.9	0.3	Bytownite	30.1	0.3
Enstatite	20.9	0.3	Enstatite	20.4	0.3	Enstatite	22.1	0.4
Diopside	10.8	0.2	Diopside	12.9	0.2	Diopside	15.9	0.3
Forsterite	10.5	0.2	Forsterite	11.6	0.2	Forsterite	11.9	0.2
Musc2m1	2.6	0.2	Quartz	1.77	0.05	Musc2m1	2.4	0.2
Talc	1.5	0.1	Talc	1.3	0.2	Quartz	1.35	0.06
Quartz	1.41	0.05	Musc2m1	0.9	0.1	Talc	1.3	0.1
Amorph	24.4	0.6	Amorph	23.2	0.6	Amorph	15	0.7

Table 6.14: Detected mineral phases and estimated standard deviation(ESD) in the three optimized formulation using X-ray powder diffraction analysis.

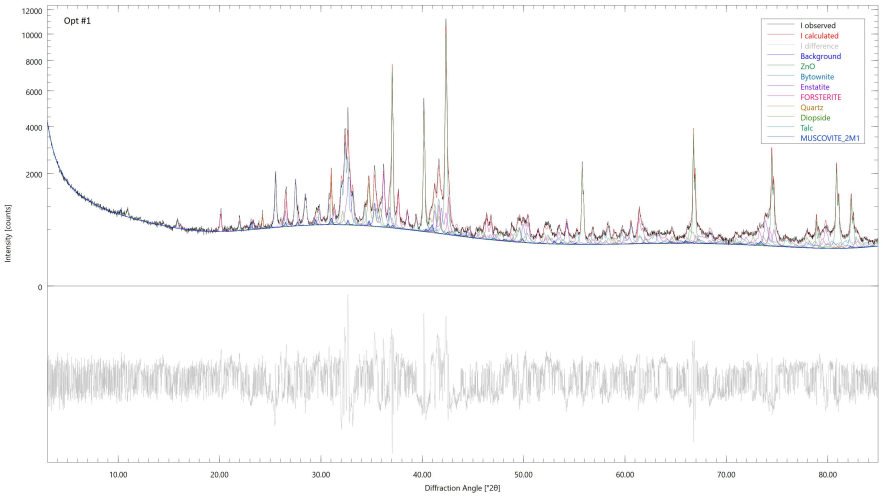

Figure 6.19: First optimized formulation quantitative phase analysis using the X-ray powder diffraction analysis.

Quantitative phase analysis of the second optimized formulation (Figure 6.20) reveals that this sample primarily consists of plagioclase, pyroxene, and olivine. Minor phases of quartz, talc, and muscovite are also present (Table6.14). We estimate the amorphous content to be around 23%.

Quantitative phase analysis of the third optimized formulation (Figure 6.21) reveals that this sample primarily consists of plagioclase, pyroxene, and olivine. Minor phases of muscovite, quartz, and talc are also present (Table6.14). We estimate the amorphous content to be around 15%.

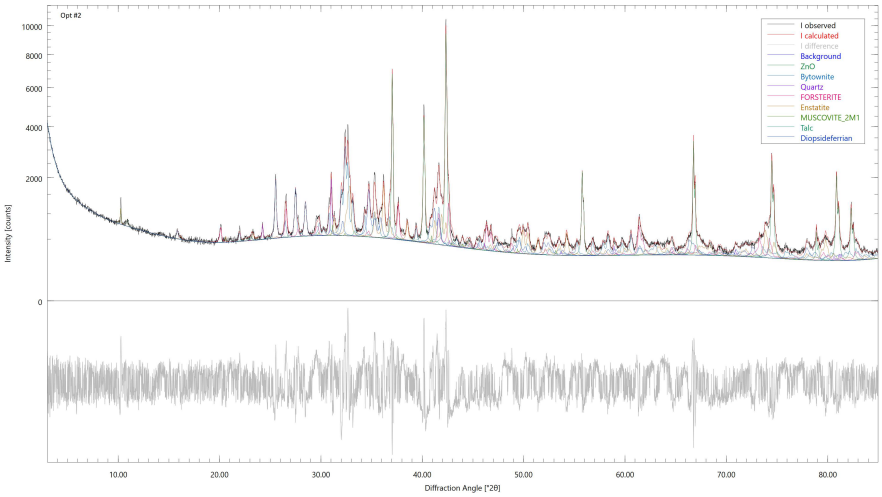

Figure 6.20: Second optimized formulation quantitative phase analysis using the X-ray powder diffraction analysis.

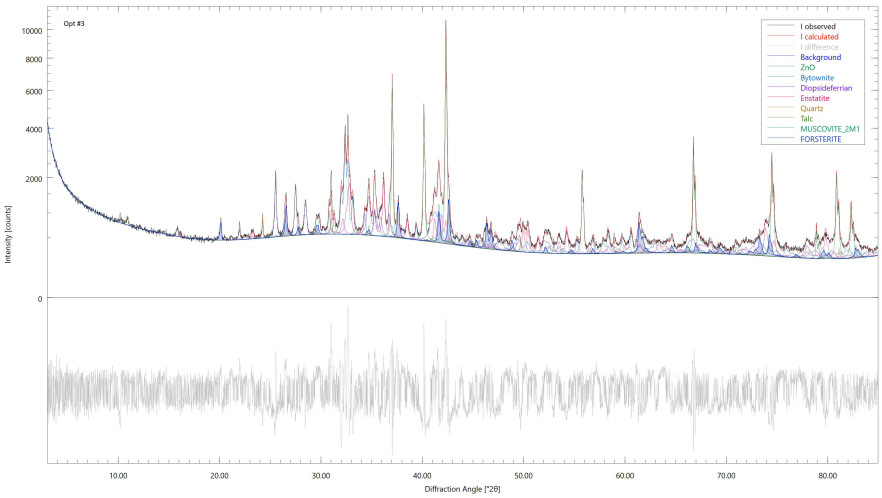

Figure 6.21: Third optimized formulation quantitative phase analysis using the X-ray powder diffraction analysis.

Figures 6.22 show how much of each mineral phase is present in three optimized formulations. This figure shows that in the first, second, and third formulations, the amounts of all mineral phases in LMS-1D decrease depending on the amount of metakaolin that is added to the mixes. The higher the metakaolin fraction, the higher the amorphous content, and the lower the quantity of LMS-1D mineral phases. No extra phases were detected by XRPD analysis.

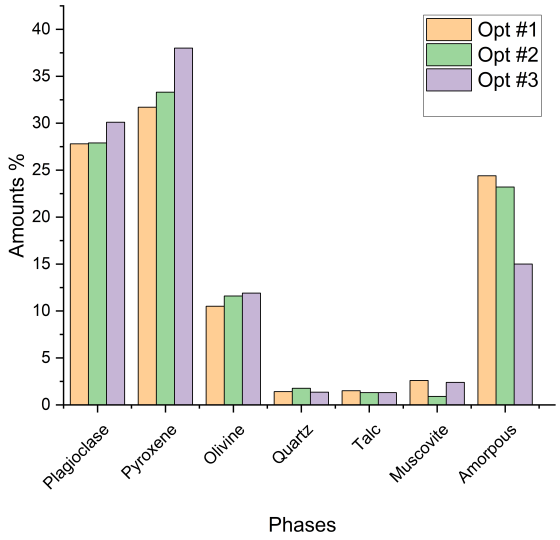

Figure 6.22: Comparison of the mineral content of the three optimized formulations using X-ray powder diffraction analysis.

6.3.2 *Scanning electron microscopy*

Scanning electron microscopy (SEM) and energy dispersive spectroscopy (EDS) were used to gain more information about the microstructure of the three optimized formulations. Figures6.23a, 6.23b, and 6.23c show the results of scanning electron microscopy for optimizations 1, 2, and 3, respectively. In all three samples, grains are dispersed in a dense amorphous matrix; however, the third formulation shows fractures and cracks throughout the matrix structure (Figures6.23c and 6.23d).

Figure 6.24 shows the average chemical composition of the matrix detected using energy dispersive spectroscopy (EDS).

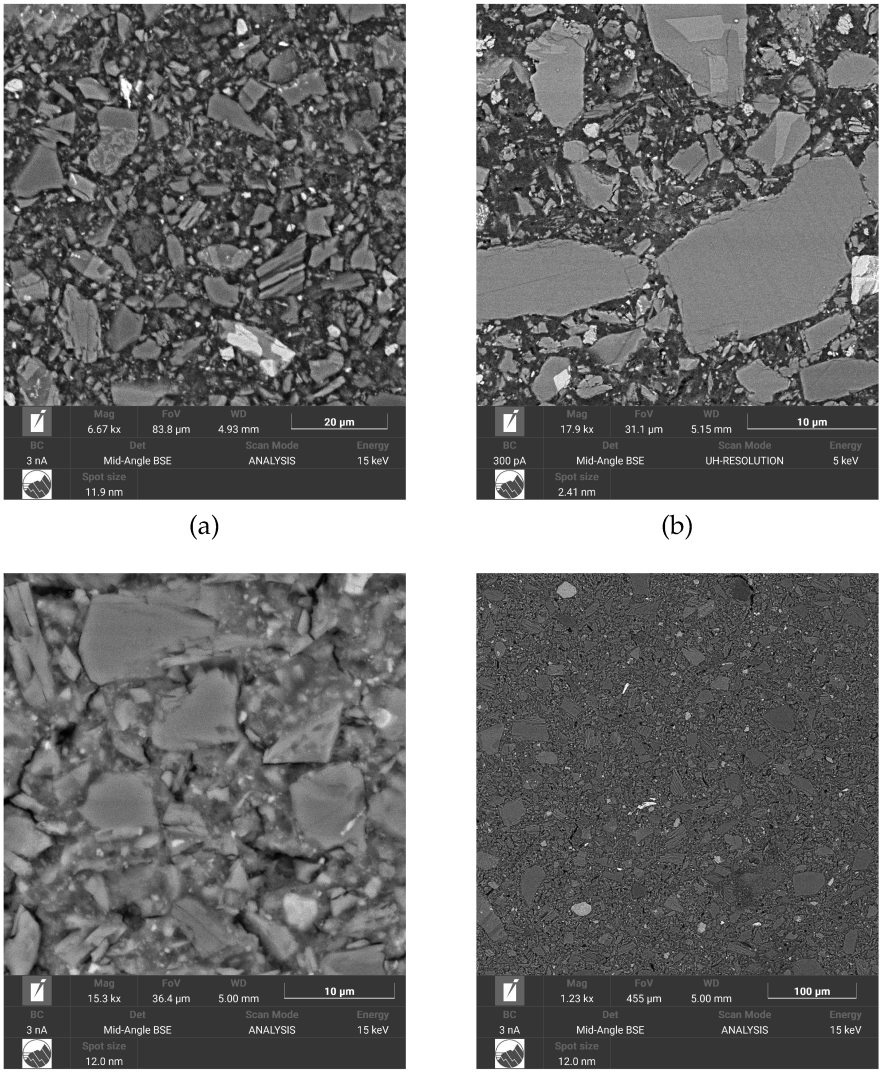

Figure 6.23: Mid-angle back scattered electron (BSE) image of (a) the first optimized formulation with 6670x magnification, (b) the second optimized formulation with 17900x magnification, (c) the third optimized formulation with 15300x magnification, and (d) the third optimized formulation with 1230x magnification.

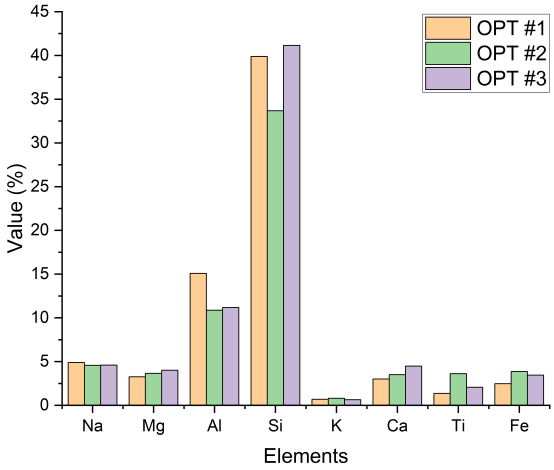

Figure 6.24: The matrix's average amounts of elements were measured using energy dispersive spectroscopy (EDS).

7

DISCUSSION AND CONCLUSION

7.1 DISCUSSION

To prove the fidelity of the Lunar Mare dust regolith simulant (LMS-1D), quantitative X-ray diffraction (XRD), X-ray fluorescence (XRF), scanning electron microscopy (SEM), energy dispersive spectroscopy (EDS), and laser diffraction analysis were applied. The simulant samples were assessed based on their mineral and chemical composition, as well as their particle size. These tests are critical for estimating simulants' behavior in alkali activation using sodium hydroxide and sodium silicate, as well as the anticipated 3D-printing operations as possible components of the ISRU concept. Particle size characteristics of the LMS-1D using the laser diffraction analysis (Table 6.1) illustrate that the median particle size measured is about 3 µm, and 90 % of the particles are below 22 microns, which is consistent with the median size value of 4 µm reported by the producer[72].

Based on the mineral composition of genuine regolith samples (Figure 2.4), variations in mineral quantities are typical for Lunar rock. This variation is present even within samples from the same region. Apollo 11 (sample 10084) and 12 (samples 12001, 12033, and 12044) missions' which landed in the predominantly basaltic Mare region were used as the reference[105]. Since only the amorphous content of the sample reacts in the alkali activation process, the amount of agglutinates and glass is considered as the main source of amorphous content in the Lunar regolith. Agglutinates are the main constituents of Lunar soils and, on average, make up 25–30% of Lunar soils, but their quantity can vary from a rare 5% to 65%. For the Apollo 12 (sample 12044) using X-ray diffraction analysis, Taylor et al. measured the amount of glass content to be around 32% [111]. Due to the continuous micrometeoroid bombardment of the regolith's surface, the amount of agglutinates in Lunar soil grows with time[84]; therefore, it is important to study the alkali activation system with the minimum amount of amorphous content. Using quantitative X-ray diffraction analysis, we measured the amount of amorphous fraction of the LMS-1D sample to be around 10 % (Table 6.2). Metakaolin was added to LMS-1D to increase the

amorphous fraction and reactive aluminum content. Therefore, the alkali activation results with LMS-1D and the genuine Lunar regolith would be comparable. The main constituents of the Lunar Mare regolith, such as plagioclase, pyroxene, and olivine, are present in the LMS-1D. However, minor phases such as talc, amphiboles, quartz, and phyllosilicates are also present, and the peak for ilmenite is not visible (Table 6.2). Our X-ray fluorescence analyses showed that the main oxides in the LMS-1D are SiO_2 (47.24 %), MgO (15.9 %), and Al_2O_3 (13.06 %), respectively (Table6.3), and it is compatible with the reported values by the producers as SiO_2 (46.9 %), MgO (16.8 %), and Al_2O_3 (12.4 %) (Table2.3). The SEM-EDS measurements confirmed the results of X-ray diffraction, as well as the minor presence of ilmenite and talc.

We used the design of the experiment to investigate the effects of curing temperature, percentage of metakaolin, ratios of liquid to solid, and Si/Na on the yield stress and compressive strength of the alkali-activated material. This approach not only reduced the number of experiments compared to the one-factor-at-a-time approach, but it also had the ability to predict the non-linear interaction of factors on the measured responses. According to the analysis of variance (ANOVA), the empirical models were good predictors of system behavior, and 76.53% and 93.49% of the variation in yield stress and compressive strength are explained by the model, respectively.

The yield stress model includes significant terms such as the liquid-to-solid ratio, amount of metakaolin, temperature, the interaction of the Si/Na ratio with metakaolin, the liquid-to-solid ratio with metakaolin, metakaolin and temperature, and finally the quadratic term of temperature squared. In the investigated liquid-to-solid ranges, the variation in yield stress is not significant. Figures6.14-6.16 show a non-monotonic behavior; indeed, it would be difficult to justify conceptually why the yield stress increases with the amount of liquid.

At low liquid-to-solid ratios, an increase in the amount of metakaolin has a slight impact on yield stress. In contrast, at higher liquid-to-solid ratios, increasing the amount of metakaolin dramatically increases the yield stress. Metakaolin particles have a high surface area and can enhance interparticle forces when well-dispersed in high liquid-to-solid ratios. This leads to stronger interparticle bonding and higher yield stress. While at a low liquid-to-solid ratio, the metakaolin particles may not be able to form a network or significantly alter the microstruc-

ture of the soil matrix. This is consistent with the flowability, consistency, and water absorption of modified cement mortars containing metakaolin at different water-to-binder ratios[117]. Yield stress increases with the increase in temperature at different liquid-to-solid ratios and silica-to-sodium ratios. This effect is more pronounced at high liquid-to-solid ratios and higher amounts of metakaolin.

In the compressive strength model, significant terms include the Si/Na ratio, the liquid-to-solid ratio, metakaolin, the interaction between the Si/Na ratio and metakaolin, metakaolin and temperature, and finally the quadratic term metakaolin squared. As the amount of metakaolin increases, compressive strength increases dramatically. This increase is more pronounced at the lowest liquid-to-solid ratio. The alkali activation process involves the dissolution of alumina and silica from metakaolin, followed by polymerization to form the N-A-S-H gel. Higher amounts of metakaolin facilitate a greater extent of this polymerization, leading to a more robust and cohesive microstructure[34, 90]. Having a lower liquid-to-solid ratio results in lower porosity after the chemical reactions and setting process, leading to a denser and stronger matrix.

Compressive strength increases as the amount of metakaolin and the Si/Na ratio increase. A high concentration of the alkaline silicates results in the formation of longer-chain silicate oligomers and Al-O-Si complexes, which promote the strength [66]. Moreover, silicate activation tends to produce products with lower porosity and higher strength[109]. While the effect of metakaolin is sensitive to temperature, the effect of the Si/Na ratio on compressive strength remains independent of temperature.

The liquid-to-solid ratio, the amount of metakaolin, the interaction of the Si/Na ratio with metakaolin, and finally the interaction of metakaolin with temperature are significant in both models. It is important to note that, although the Si/Na ratio is not significant for yield stress, it is important for the compressive strength of the final product. Also, the temperature and the interaction of the liquid-to-solid ratio with metakaolin are significant for the yield stress, but their effect on the compressive strength is minimal. This strong temperature dependence for yield stress is more likely to be attributed to water evaporation.

Based on the predictive models, three validation tests with optimized formulations were selected to have high, medium, and low compressive strengths (Figures 6.14, 6.15, and 6.16). For

the first and second samples, we used the Si/Na ratio of 1.4 and 1.5 and set the liquid-to-solid ratio at the optimum of 0.41. For the third sample, we selected a lower liquid-to-solid ratio of 0.4 to see if we could reduce the amount of liquid in the system. The amounts of metakaolin were decreased from 12 to 8.5 and finally to 5 percent to find the lowest possible amount of metakaolin in this alkali activation system. Considering that temperature doesn't have a significant effect on the compressive strength, we set all the temperatures to 20 °C to maintain the lowest energy consumption. All of the experimental results for yield stress and compressive strength are within the model's confidence interval. However, the third formulation's response to the yield stress is lower than the predicted values. The second formulation could be optimal for 3D printing because it combines high strength with a relatively low amount of metakaolin. Furthermore, the relatively high yield stress is beneficial during extrusion because it prevents the collapse of extruded layers on top of each other.

X-ray diffraction analysis (XRD) of the optimized formulations shows that the amorphous content in the three formulations decreases with a decrease in the amount of metakaolin. Based on the added amount of metakaolin and the initial glass in the LMS-1D simulant, the least amount of amorphous content considering the 100 % efficiency for the three alkali activation samples should be at least 22.8, 19.3, and 15.8 %, respectively. The amorphous content of the first, second, and third optimization is measured to be about 24.4, 23.2, and 15%. This suggests that the efficiency of the third formulation is lower than that of the first and second ones.

Scanning electron microscopy (SEM) reveals a dense amorphous matrix with the LMS-1D minerals serving as aggregates (Figures 6.23a and 6.23b). The first and second formulations show proper mechanical strength, as predicted. The SEM images show that the third formulation has a porous structure with cracks that is compatible with the low compressive strength measurement (Figures 6.23c and 6.23d). Although the sodium alumino-silicate gel's chemical structure is not yet fully defined, it is believed that sodium alumino-silicate hydrate (N-A-S-H) gel consists of a polymeric Si-O-Al framework. The presence of AlO_4 tetrahedron results in a net negative charge for the silicate-aluminate skeleton. Therefore, cations such as Na^+ or K^+ are immobilized for neutralizing the charge[6, 35, 36, 106]. EDS measurement of the matrix chemical composition (Figure6.24) in three formulations shows a high amount of Mg content in

the gel structure. This could be due to the high Mg concentration in the LMS-1D initial composition (Figure6.3), either in its amorphous and glass forms or because Mg was incorporated into the gel structure.

It has been suggested that the Mg^{2+} can be accommodated in alumino-silicate gel as network-modifying cations[86]. ICP and ion chromatography studies in experiments with sulfate attack on fly ash geopolymers indicated a migration of Ca from the inside of the specimen to the surface area and S and Mg from the solution into the aluminosilicate matrix. Also molecular dynamics simulation studies shows that surface hydroxyls provide a non-bridging oxygen site to link with the neighboring Na^{+}/Mg^{2+}, which leads to cationic adsorption on the N-A-S-H surface. When placing the geopolymers in contact with solutions with high sodium and magnesium content, magnesium ions penetrate more deeply into the hydroxyl layer than sodium ions. With the high positive charge and small ionic radius, Mg^{2+} ions are likely to be adsorbed on the N-A-S-H surface and penetrate into the N-A-S-H matrix[123].

From the economical and environmental point of view, using the proposed alkali activation system in this study requires 65% less material transportation than the conventional use of ordinary Portland cement. SpaceX's Falcon 9 offers a cost of 2,720 dollars per kilogram for transportation to the low-Earth orbit [60]. As a result, the cost of transporting the necessary material to produce 1 ton of cement paste with a water-to-cement ratio of 0.41 on the Moon equals 2.72 million dollars, whereas it drops to 0.95 million dollars for the alkali-activated material.

7.2 CONCLUSSION

In this thesis, we investigated the potential of alkali activation as a viable approach for contributing to the feasibility and sustainability of in-situ resource utilization for future space exploration missions. We investigated the design of experiment approach optimizing the formulation parameters and understanding their impact on the rheological and mechanical properties of alkali-activated regolith simulants. In summary, the thesis work has led to the following outcomes:

- Cement-like binders with appropriate cohesive properties can be obtained by alkaline activation of lunar regolith simulants.
- Fine tuning the engineering properties of such binders requires a knowledge-based formulation and rigorous characterization of the reactive powders, including the assessment of the chemical composition of the amorphous fraction. This is a fundamental point, considering the intrinsic variability of lunar soils' compositions.
- Given the relatively low amount of amorphous fraction and reactive aluminium, the addition of limited amounts of metakaolin was necessary to induce the formation of N-A-S-H phases, which convey cohesive properties to low-Ca alkali-activated binders.
- The alkali activation in-situ resource utilization method that has been presented provides several benefits, both economically and environmentally, that contribute to the sustainability in interplanetary exploration programs.

7.2.1 *Future Developments*

It would be highly beneficial to investigate the use of chemical admixtures to further reduce water consumption. Additionally, one might consider investigating the potential to increase the amount of reactive aluminum without the necessity of adding metakaolin. One possibility is substituting sodium aluminate for the sodium silicate activator, potentially enhancing material reactivity and strength. Furthermore, future research could focus on the production of macroporous materials aimed at optimizing thermal properties, which could significantly improve insulation and energy efficiency. Finally, studying the alkali activation process under lunar environmental conditions, particularly in the vacuum of space, could offer invaluable insights for future lunar construction projects, paving the way for advancements in extraterrestrial building technologies.

BIBLIOGRAPHY

[1] *318-02/(318R-02): Building Code Requirements for Structural Concrete and Commentary*. https://www.concrete.org/publications/internationalconcreteabstractsportal/m/details/id/13158. American Concrete Institute (ACI).

[2] Constance M. Adams and Georgi Petrov. "The Surface Endoskeletal Inflatable Module (SEIM)." In: (Apr. 2012), pp. 1–8. DOI: 10.1061/40830(188)59.

[3] Livia B. Agostinho, de C. Pereira Alexandre, Eugênia F. da Silva, and Romildo Dias Toledo Filho. "Rheological Study of Portland Cement Pastes Modified with Superabsorbent Polymer and Nanosilica." In: *Journal of Building Engineering* 34 (Feb. 2021), p. 102024. ISSN: 2352-7102. DOI: 10.1016/j.jobe.2020.102024.

[4] Timothy A Aiken, Wei Sha, Jacek Kwasny, and Marios N Soutsos. "Resistance of Geopolymer and Portland Cement Based Systems to Silage Effluent Attack." In: *Cement and Concrete Research* 92 (Feb. 2017), pp. 56–65. ISSN: 0008-8846. DOI: 10.1016/j.cemconres.2016.11.015.

[5] A. M. Mustafa Al Bakri, H. Kamarudin, M. Binhussain, I. Khairul Nizar, A. R. Rafiza, and Y. Zarina. "Comparison of Geopolymer Fly Ash and Ordinary Portland Cement to the Strength of Concrete." In: *Advanced Science Letters* 19.12 (Dec. 2013), pp. 3592–3595. DOI: 10.1166/asl.2013.5187.

[6] Valeria F. F Barbosa, Kenneth J. D MacKenzie, and Clelio Thaumaturgo. "Synthesis and Characterisation of Materials Based on Inorganic Polymers of Alumina and Silica: Sodium Polysialate Polymers." In: *International Journal of Inorganic Materials* 2.4 (Sept. 2000), pp. 309–317. ISSN: 1466-6049. DOI: 10.1016/S1466-6049(00)00041-6.

[7] Howard A. Barnes, John Fletcher Hutton, and K. Walters. *An Introduction to Rheology*. Elsevier, June 1989. ISBN: 978-0-444-87140-4.

[8] A. Basu and D. S. Mckay. "Chemical Variability and Origin of Agglutinitic Glass." In: *Journal of Geophysical Research, Supplement* 90 (Nov. 1985).

[9] R.L Bates and J.A Jackson. *Glossary of Geology*. 1980.

[10] Jonathan L. Bell, Pankaj Sarin, Patrick E. Driemeyer, Ryan P. Haggerty, Peter J. Chupas, and Waltraud M. Kriven. "X-Ray Pair Distribution Function Analysis of a Metakaolin-Based, KAlSi2O6·5.5H2O Inorganic Polymer (Geopolymer)." In: *Journal of Materials Chemistry* 18.48 (Dec. 2008), pp. 5974–5981. ISSN: 1364-5501. DOI: 10.1039/B808157C.

[11] Jonathan L. Bell, Pankaj Sarin, John L. Provis, Ryan P. Haggerty, Patrick E. Driemeyer, Peter J. Chupas, Jannie S. J. van Deventer, and Waltraud M. Kriven. "Atomic Structure of a Cesium Aluminosilicate Geopolymer: A Pair Distribution Function Study." In: *Chemistry of Materials* 20.14 (July 2008), pp. 4768–4776. ISSN: 0897-4756. DOI: 10.1021/cm703369s.

[12] Haym Benaroya and Leonhard Bernold. "Engineering of Lunar Bases." In: *Acta Astronautica* 62.4 (Feb. 2008), pp. 277–299. ISSN: 0094-5765. DOI: 10.1016/j.actaastro.2007.05.001.

[13] J. Bergmann, P. Friedel, and R. Kleeberg. "Handling of Unusual Instrumental Profiles by the BGMN Rietveld Program." In: *European Powder Diffraction 6*. Vol. 321. Materials Science Forum. Trans Tech Publications Ltd, Jan. 2000, pp. 192–197. DOI: 10.4028/www.scientific.net/MSF.321-324.192.

[14] Susan A. Bernal, Ruby Mejía de Gutiérrez, and John L. Provis. "Engineering and Durability Properties of Concretes Based on Alkali-Activated Granulated Blast Furnace Slag/Metakaolin Blends." In: *Construction and Building Materials* 33 (Aug. 2012), pp. 99–108. ISSN: 0950-0618. DOI: 10.1016/j.conbuildmat.2012.01.017.

[15] Susan Bernal, Ruby De Gutierrez, Silvio Delvasto, and Erich Rodriguez. "Performance of an Alkali-Activated Slag Concrete Reinforced with Steel Fibers." In: *Construction and Building Materials*. Inorganic-Bonded Fiber Composites 24.2 (Feb. 2010), pp. 208–214. ISSN: 0950-0618. DOI: 10.1016/j.conbuildmat.2007.10.027.

[16] Marcos Almeida Bezerra, Ricardo Erthal Santelli, Eliane Padua Oliveira, Leonardo Silveira Villar, and Luciane Amélia Escaleira. "Response Surface Methodology (RSM) as a Tool for Optimization in Analytical Chemistry." In:

Talanta 76.5 (Sept. 2008), pp. 965–977. ISSN: 0039-9140. DOI: 10.1016/j.talanta.2008.05.019.

[17] Dali Bondar, C. Lynsdale, Neil Milestone, Nemat Hassani, and Ali Ramezanianpour. "Engineering Properties of Alkali-Activated Natural Pozzolan Concrete." In: *Aci Materials Journal* (Jan. 2011).

[18] Christoph Buchner, Roland H. Pawelke, Thomas Schlauf, Alexander Reissner, and Advenit Makaya. "A New Planetary Structure Fabrication Process Using Phosphoric Acid." In: *Acta Astronautica* 143 (Feb. 2018), pp. 272–284. ISSN: 0094-5765. DOI: 10.1016/j.actaastro.2017.11.045.

[19] W. D. Carrier, J. K. Mitchell, and A. Mahmood. *The Relative Density of Lunar Soil*. Jan. 1973.

[20] *Cement Technology Roadmap Plots Path to Cutting CO2 Emissions 24% by 2050 - News*. https://www.iea.org/news/cement-technology-roadmap-plots-path-to-cutting-co2-emissions-24-by-2050.

[21] Giovanni Cesaretti, Enrico Dini, Xavier De Kestelier, Valentina Colla, and Laurent Pambaguian. "Building Components for an Outpost on the Lunar Soil by Means of a Novel 3D Printing Technology." In: *Acta Astronautica* 93 (Jan. 2014), pp. 430–450. ISSN: 0094-5765. DOI: 10.1016/j.actaastro.2013.07.034.

[22] *Chang'e-5: 's Sample Return Mission*. https://www.planetary.org/space-missions/change-5.

[23] Jeremy Karl Cockcroft and Andrew N. Fitch. "Experimental Setups." In: *Powder Diffraction: Theory and Practice*. The Royal Society of Chemistry, Mar. 2008. ISBN: 978-0-85404-231-9.

[24] Marc M. Cohen. "Selected Precepts in Lunar Architecture." In: *IAF Abstracts, 34th COSPAR Scientific Assembly*. Jan. 2002, p. 716.

[25] F. G. Collins and J. G. Sanjayan. "Workability and Mechanical Properties of Alkali Activated Slag Concrete." In: *Cement and Concrete Research* 29.3 (Mar. 1999), pp. 455–458. ISSN: 0008-8846. DOI: 10.1016/S0008-8846(98)00236-1.

[26] Michael R. Cooper, Robert L. Kovach, and Joel S. Watkins. "Lunar Near-Surface Structure." In: *Reviews of Geophysics* 12.3 (1974), pp. 291–308. ISSN: 1944-9208. DOI: 10.1029/RG012i003p00291.

[27] Ian A. Crawford. "Lunar Resources: A Review." In: (Oct. 2014). DOI: 10.48550/arXiv.1410.6865. arXiv: 1410.6865 [astro-ph].

[28] J. Davidovits. "Geopolymers." In: *Journal of thermal analysis* 37.8 (Aug. 1991), pp. 1633–1656. ISSN: 1572-8943. DOI: 10.1007/BF01912193.

[29] George Derringer and Ronald Suich. "Simultaneous Optimization of Several Response Variables." In: *Journal of Quality Technology* (Oct. 1980). ISSN: 0022-4065.

[30] J. M. Devine, D. S. McKay, and J. J. Papike. "Lunar Regolith: Petrology of the <10 *M*m Fraction." In: *Lunar and Planetary Science Conference Proceedings* 87 (Jan. 1982), 260–A268. DOI: 10.1029/JB087iS01p0A260.

[31] N. Doebelin and R. Kleeberg. "Profex: A Graphical User Interface for the Rietveld Refinement Program BGMN." In: *Journal of Applied Crystallography* 48.5 (Oct. 2015), pp. 1573–1580. ISSN: 1600-5767. DOI: 10.1107/S1600576715014685.

[32] E. Douglas, A. Bilodeau, J. Brandstetr, and V. M. Malhotra. "Alkali Activated Ground Granulated Blast-Furnace Slag Concrete: Preliminary Investigation." In: *Cement and Concrete Research* 21.1 (Jan. 1991), pp. 101–108. ISSN: 0008-8846. DOI: 10.1016/0008-8846(91)90036-H.

[33] Frederick Duennebier and George H. Sutton. "Thermal Moonquakes." In: *Journal of Geophysical Research (1896-1977)* 79.29 (1974), pp. 4351–4363. ISSN: 2156-2202. DOI: 10.1029/JB079i029p04351.

[34] P. Duxson, A. Fernández-Jiménez, J. L. Provis, G. C. Lukey, A. Palomo, and J. S. J. van Deventer. "Geopolymer Technology: The Current State of the Art." In: *Journal of Materials Science* 42.9 (May 2007), pp. 2917–2933. ISSN: 1573-4803. DOI: 10.1007/s10853-006-0637-z.

[35] P. Duxson, G. C. Lukey, F. Separovic, and J. S. J. van Deventer. "Effect of Alkali Cations on Aluminum Incorporation in Geopolymeric Gels." In: *Industrial & Engineering Chemistry Research* 44.4 (Feb. 2005), pp. 832–839. ISSN: 0888-5885. DOI: 10.1021/ie0494216.

[36] Peter Duxson, Grant C. Lukey, and Jannie S. J. van Deventer. "Physical Evolution of Na-geopolymer Derived from Metakaolin up to 1000 °C." In: *Journal of Materials Science* 42.9 (May 2007), pp. 3044–3054. ISSN: 1573-4803. DOI: 10.1007/s10853-006-0535-4.

[37] Peter Duxson, John L. Provis, Grant C. Lukey, and Jannie S. J. van Deventer. "The Role of Inorganic Polymer Technology in the Development of 'Green Concrete'." In: *Cement and Concrete Research* 37.12 (Dec. 2007), pp. 1590–1597. ISSN: 0008-8846. DOI: 10.1016/j.cemconres.2007.08.018.

[38] Heshmatollah Ebrahimi-Najafabadi, Riccardo Leardi, and Mehdi Jalali-Heravi. "Experimental Design in Analytical Chemistry—Part I: Theory." In: *Journal of AOAC INTERNATIONAL* 97.1 (Jan. 2014), pp. 3–11. ISSN: 1060-3271. DOI: 10.5740/jaoacint.SGEEbrahimi1.

[39] A. Elimbi, H. K. Tchakoute, and D. Njopwouo. "Effects of Calcination Temperature of Kaolinite Clays on the Properties of Geopolymer Cements." In: *Construction and Building Materials* 25.6 (June 2011), pp. 2805–2812. ISSN: 0950-0618. DOI: 10.1016/j.conbuildmat.2010.12.055.

[40] W. C. Feldman, S. Maurice, A. B. Binder, B. L. Barraclough, R. C. Elphic, and D. J. Lawrence. "Fluxes of Fast and Epithermal Neutrons from Lunar Prospector: Evidence for Water Ice at the Lunar Poles." In: *Science* 281.5382 (Sept. 1998), pp. 1496–1500. DOI: 10.1126/science.281.5382.1496.

[41] S. L. C. Ferreira et al. "Box-Behnken Design: An Alternative for the Optimization of Analytical Methods." In: *Analytica Chimica Acta* 597.2 (Aug. 2007), pp. 179–186. ISSN: 0003-2670. DOI: 10.1016/j.aca.2007.07.011.

[42] K. L. Ferrone, A. B. Taylor, and H. Helvajian. "*In Situ* Resource Utilization of Structural Material from Planetary Regolith." In: *Advances in Space Research* 69.5 (Mar. 2022), pp. 2268–2282. ISSN: 0273-1177. DOI: 10.1016/j.asr.2021.12.025.

[43] Huan Gao, Libing Liao, Hao Liu, Lefu Mei, Zejie Wang, Danlan Huang, Guocheng Lv, Guodian Zhu, and Chuxuan Wang. "Optimization of Thermal Insulation Performance of Porous Geopolymers under the Guidance of Thermal Conductivity Calculation." In: *Ceramics Inter-*

national 46.10, Part B (July 2020), pp. 16537–16547. ISSN: 0272-8842. DOI: 10.1016/j.ceramint.2020.03.221.

[44] Zifan Geng, Lizhi Zhang, Hao Pan, Wei She, Cheng Zhou, Hao Zhou, Zhenglei Yu, and Zhaodong Xu. "In-Situ Solidification of Alkali-Activated Lunar Regolith: Insights into the Chemical and Physical Origins." In: *Journal of Cleaner Production* 391 (Mar. 2023), p. 136147. ISSN: 0959-6526. DOI: 10.1016/j.jclepro.2023.136147.

[45] Zifan Geng, Lizhi Zhang, Hao Pan, Wei She, Cheng Zhou, Hao Zhou, Zhenglei Yu, and Zhaodong Xu. "In-Situ Solidification of Alkali-Activated Lunar Regolith: Insights into the Chemical and Physical Origins." In: *Journal of Cleaner Production* 391 (Mar. 2023), p. 136147. ISSN: 0959-6526. DOI: 10.1016/j.jclepro.2023.136147.

[46] L. V. Gurvich, G. A. Bergman, L. N. Gorokhov, V. S. Iorish, V. Ya. Leonidov, and V. S. Yungman. "Thermodynamic Properties of Alkali Metal Hydroxides. Part 1. Lithium and Sodium Hydroxides." In: *Journal of Physical and Chemical Reference Data* 25.4 (July 1996), pp. 1211–1276. ISSN: 0047-2689, 1529-7845. DOI: 10.1063/1.555982.

[47] L. V. Gurvich, G. A. Bergman, L. N. Gorokhov, V. S. Iorish, V. Ya. Leonidov, and V. S. Yungman. "Thermodynamic Properties of Alkali Metal Hydroxides. Part II. Potassium, Rubidium, and Cesium Hydroxides." In: *Journal of Physical and Chemical Reference Data* 26.4 (July 1997), pp. 1031–1110. ISSN: 0047-2689. DOI: 10.1063/1.555996.

[48] Tarja Häkkinen. "The Influence of Slag Content on the Microstructure, Permeability and Mechanical Properties of Concrete: Part 2 Technical Properties and Theoretical Examinations." In: *Cement and Concrete Research* 23.3 (May 1993), pp. 518–530. ISSN: 0008-8846. DOI: 10.1016/0008-8846(93)90002-Q.

[49] Djwantoro Hardjito and B. Rangan. "Development and Properties of Low-calcium Fly Ash Based Geopolymer Concrete." In: (Jan. 2005).

[50] Grant H. Heiken, David T. Vaniman, and Bevan M. French. *Lunar Sourcebook, A User's Guide to the Moon*. Jan. 1991.

[51] C. Hirt and W. E. Featherstone. "A 1.5 Km-Resolution Gravity Field Model of the Moon." In: *Earth and Planetary Science Letters* 329–330 (May 2012), pp. 22–30. ISSN: 0012-821X. DOI: 10.1016/j.epsl.2012.02.012.

[52] Sk S. Hossain, P. K. Roy, and Chang-Jun Bae. "Utilization of Waste Rice Husk Ash for Sustainable Geopolymer: A Review." In: *Construction and Building Materials* 310 (Dec. 2021), p. 125218. ISSN: 0950-0618. DOI: 10.1016/j.conbuildmat.2021.125218.

[53] Julie Hot, Hela Bessaies-Bey, Coralie Brumaud, Myriam Duc, Charlène Castella, and Nicolas Roussel. "Adsorbing Polymers and Viscosity of Cement Pastes." In: *Cement and Concrete Research* 63 (Sept. 2014), pp. 12–19. ISSN: 0008-8846. DOI: 10.1016/j.cemconres.2014.04.005.

[54] *Human Landing Systems - NASA*.

[55] Tony B. Husbands, P. G. Malone, and Lillian D. Wakeley. *Performance of Concretes Proportioned with Pyrament Blended Cement*. Report. U.S. Army Engineer Waterways Experiment Station, Apr. 1994.

[56] *International Space Exploration Coordination Group - NASA*. https://www.nasa.gov/humans-in-space/international-space-exploration-coordination-group/.

[57] Maxim Isachenkov, Svyatoslav Chugunov, Zoe Landsman, Iskander Akhatov, Anna Metke, Andrey Tikhonov, and Igor Shishkovsky. "Characterization of Novel Lunar Highland and Mare Simulants for ISRU Research Applications." In: *Icarus* 376 (Apr. 2022), p. 114873. ISSN: 0019-1035. DOI: 10.1016/j.icarus.2021.114873.

[58] M. Rafiqul Islam and M. Enamul Hossain. "Chapter 2 - State-of-the-art of Drilling." In: *Drilling Engineering*. Ed. by M. Rafiqul Islam and M. Enamul Hossain. Sustainable Oil and Gas Development Series. Gulf Professional Publishing, Jan. 2021, pp. 17–178. ISBN: 978-0-12-820193-0. DOI: 10.1016/B978-0-12-820193-0.00002-2.

[59] A.M. Jablonski and K.A. Ogden. "Technical Requirements for Lunar Structures." In: *Journal of Aerospace Engineering* 21.2 (2008), pp. 72–90. ISSN: 0893-1321. DOI: 10.1061/(ASCE)0893-1321(2008)21:2(72).

[60] Harry W. Jones. "The Recent Large Reduction in Space Launch Cost." In: *International Conference on Environmental Systems (ICES)*. Albuquerque, NM, July 2018.

[61] Nicos Kalapodis, Georgios Kampas, and Olga-Joan Ktenidou. "A Review towards the Design of Extraterrestrial Structures: From Regolith to Human Outposts." In: *Acta Astronautica* 175 (Oct. 2020), pp. 540–569. ISSN: 0094-5765. DOI: 10.1016/j.actaastro.2020.05.038.

[62] Hiroshi Kanamori, Satoru Udagawa, Tetsuji Yoshida, Shinji Matsumoto, and Kenji Takagi. "Properties of Lunar Soil Simulant Manufactured in Japan." In: (Apr. 2012), pp. 462–468. DOI: 10.1061/40339(206)53.

[63] Kriss Kennedy and Constance Adams. "International Space Station (ISS) TransHab: An Inflatable Habitat." In: (Jan. 2000).

[64] Behrokh Khoshnevis, Anders Carlson, and Madhu Thangavelu. *ISRU-Based Robotic Construction Technologies For Lunar And Martian Infrastructures*. Apr. 2017.

[65] Behrokh Khoshnevis and Jing Zhang. "Extraterrestrial Construction Using Contour Crafting." In: (Aug. 2012).

[66] Kostas Komnitsas and Dimitra Zaharaki. "Geopolymerisation: A Review and Prospects for the Minerals Industry." In: *Minerals Engineering* 20.14 (Nov. 2007), pp. 1261–1277. ISSN: 0892-6875. DOI: 10.1016/j.mineng.2007.07.011.

[67] Hans Kuehl. "Slag Cement and Process of Making the Same." Pat. US900939A. Oct. 1908.

[68] David R. Lammlein. "Lunar Seismicity and Tectonics." In: *Physics of the Earth and Planetary Interiors* 14.3 (June 1977), pp. 224–273. ISSN: 0031-9201. DOI: 10.1016/0031-9201(77)90175-3.

[69] Riccardo Leardi. "Experimental Design in Chemistry: A Tutorial." In: *Analytica Chimica Acta*. Fundamental and Applied Analytical Science. A Special Issue In Honour of Alan Townshend. 652.1 (Oct. 2009), pp. 161–172. ISSN: 0003-2670. DOI: 10.1016/j.aca.2009.06.015.

[70] Aida Margarita Ley-Hernández and Dimitri Feys. "Challenges in Rheological Characterization of Cement Pastes Using a Parallel-Plates Geometry." In: *Rheology and Processing of Construction Materials*. Ed. by Viktor Mechtcherine, Kamal Khayat, and Egor Secrieru. Cham: Springer International Publishing, 2020, pp. 228–236. ISBN: 978-3-030-22566-7. DOI: 10.1007/978-3-030-22566-7_27.

[71] Shanhong Liu, Jianguo Yan, Jianfeng Cao, Mao Ye, Xie Li, Fei Li, and Jean-Pierre Barriot. "Review of the Precise Orbit Determination for Chinese Lunar Exploration Projects." In: *Earth and Space Science* 8.4 (2021), e2020EA001361. ISSN: 2333-5084. DOI: 10.1029/2020EA001361.

[72] *Lunar Mare Dust (LMS-1D) Moon Dust Simulant*. https://spaceresourcetech.com/products/lms-1d.

[73] *Lunar Rocks and Soils from Apollo Missions*.

[74] Torbjörn Lundstedt, Elisabeth Seifert, Lisbeth Abramo, Bernt Thelin, Åsa Nyström, Jarle Pettersen, and Rolf Bergman. "Experimental Design and Optimization." In: *Chemometrics and Intelligent Laboratory Systems* 42.1 (Aug. 1998), pp. 3–40. ISSN: 0169-7439. DOI: 10.1016/S0169-7439(98)00065-3.

[75] Carole McLemore, John Fikes, Kevin McCarley, Charles Darby, Peter Curreri, James Kennedy, James Good, and Scott Gilley. "Sustainable Human Presence on the Moon Using in Situ Resources." In: *AIAA SPACE 2008 Conference & Exposition*. AIAA SPACE Forum. American Institute of Aeronautics and Astronautics, Sept. 2008. DOI: 10.2514/6.2008-7855.

[76] E. Medzmariashvili, Sh Tserodze, N. Tsignadze, M. Sanikidze, L. Datashvili, A. Sarchimelia, K. Chkhikvadze, N. Siradze, and G. Bedukadze. "A New Design Variant of the Large Deployable Space Reflector." In: (Apr. 2012), pp. 1–8. DOI: 10.1061/40830(188)6.

[77] "Mineral Commodity Summaries 2024." In: ().

[78] Denis Mitchell and Patrick Paultre. "Code Provisions for High-Strength Concrete – an International Perspective." In: *ACI Concrete International* 25 (Jan. 2003), pp. 76–90.

[79] Carlos Montes, Kaylin Broussard, Matthew Gongre, Neven Simicevic, Johanna Mejia, Jessica Tham, Erez Allouche, and Gabrielle Davis. "Evaluation of Lunar Regolith Geopolymer Binder as a Radioactive Shielding Material for Space Exploration Applications." In: *Advances in Space Research* 56.6 (Sept. 2015), pp. 1212–1221. ISSN: 0273-1177. DOI: 10.1016/j.asr.2015.05.044.

[80] Douglas C. Montgomery. *Design and Analysis of Experiments*. 8th edition. Hoboken, NJ: Wiley, Apr. 2012. ISBN: 978-1-118-14692-7.

[81] M. Z. Naser. "Extraterrestrial Construction Materials." In: *Progress in Materials Science* 105 (Aug. 2019), p. 100577. ISSN: 0079-6425. DOI: 10.1016/j.pmatsci.2019.100577.

[82] Ahmed K. Noor and John B. Malone. *Government-Sponsored Programs on Structures Technology*. Nov. 1997.

[83] D. A. Paige et al. "The Lunar Reconnaissance Orbiter Diviner Lunar Radiometer Experiment." In: *Space Science Reviews* 150.1 (Jan. 2010), pp. 125–160. ISSN: 1572-9672. DOI: 10.1007/s11214-009-9529-2.

[84] J. J. Papike, S. B. Simon, and J. C. Laul. "The Lunar Regolith: Chemistry, Mineralogy, and Petrology." In: *Reviews of Geophysics* 20.4 (1982), pp. 761–826. ISSN: 1944-9208. DOI: 10.1029/RG020i004p00761.

[85] Thomas A. Parnell, Jr Watts, and Tony W. Armstrong. "Radiation Effects and Protection for Moon and Mars Missions." In: (Apr. 2012), pp. 232–244. DOI: 10.1061/40339(206)28.

[86] D. S. Perera, M. G. Blackford, E. R. Vance, J. V. Hanna, K. S. Finnie, and C. L. Nicholson. "Geopolymers for the Immobilization of Radioactive Waste." In: *MRS Online Proceedings Library* 824.1 (Dec. 2004), pp. 432–437. ISSN: 1946-4274. DOI: 10.1557/PROC-824-CC8.35.

[87] Arnaud Perrot and Sofiane Amziane. "Concrete Rheometers." In: *Measuring Rheological Properties of Cement-based Materials: State-of-the-Art Report of the RILEM Technical Committee 266-MRP*. Ed. by Mohammed Sonebi and Dimitri Feys. RILEM State-of-the-Art Reports. Cham: Springer Nature Switzerland, 2024, pp. 33–71. ISBN: 978-3-031-36743-4. DOI: 10.1007/978-3-031-36743-4_3.

[88] Shima Pilehvar, Marlies Arnhof, Andreas Erichsen, Luca Valentini, and Anna-Lena Kjøniksen. "Investigation of Severe Lunar Environmental Conditions on the Physical and Mechanical Properties of Lunar Regolith Geopolymers." In: *Journal of Materials Research and Technology* 11 (Mar. 2021), pp. 1506–1516. ISSN: 2238-7854. DOI: 10.1016/j.jmrt.2021.01.124.

[89] Shima Pilehvar, Marlies Arnhof, Ramón Pamies, Luca Valentini, and Anna-Lena Kjøniksen. "Utilization of Urea as an Accessible Superplasticizer on the Moon for Lunar Geopolymer Mixtures." In: *Journal of Cleaner Production*

247 (Feb. 2020), p. 119177. ISSN: 0959-6526. DOI: 10.1016/j.jclepro.2019.119177.

[90] J. L. Provis, J. S. J. van Deventer, J. L. Provis, and J. S. J. van Deventer. *Geopolymers: Structures, Processing, Properties and Industrial Applications*. Woodhead Publishing, June 2009. ISBN: 978-1-84569-638-2.

[91] John L. Provis. "Introduction and Scope." In: *Alkali Activated Materials: State-of-the-Art Report, RILEM TC 224-AAM*. Ed. by John L. Provis and Jannie S. J. van Deventer. Dordrecht: Springer Netherlands, 2014, pp. 1–9. ISBN: 978-94-007-7672-2. DOI: 10.1007/978-94-007-7672-2_1.

[92] John L. Provis, Vlastimil Bílek, Anja Buchwald, Katja Dombrowski-Daube, and Benjamin Varela. "Durability and Testing – Physical Processes." In: *Alkali Activated Materials: State-of-the-Art Report, RILEM TC 224-AAM*. Ed. by John L. Provis and Jannie S. J. van Deventer. Dordrecht: Springer Netherlands, 2014, pp. 277–307. ISBN: 978-94-007-7672-2. DOI: 10.1007/978-94-007-7672-2_10.

[93] John L. Provis, Peter Duxson, Elena Kavalerova, Pavel V. Krivenko, Zhihua Pan, Francisca Puertas, and Jannie S. J. van Deventer. "Historical Aspects and Overview." In: *Alkali Activated Materials: State-of-the-Art Report, RILEM TC 224-AAM*. Ed. by John L. Provis and Jannie S. J. van Deventer. Dordrecht: Springer Netherlands, 2014, pp. 11–57. ISBN: 978-94-007-7672-2. DOI: 10.1007/978-94-007-7672-2_2.

[94] John L. Provis, Ana Fernández-Jiménez, Elie Kamseu, Cristina Leonelli, and Angel Palomo. "Binder Chemistry – Low-Calcium Alkali-Activated Materials." In: *Alkali Activated Materials: State-of-the-Art Report, RILEM TC 224-AAM*. Ed. by John L. Provis and Jannie S. J. van Deventer. Dordrecht: Springer Netherlands, 2014, pp. 93–123. ISBN: 978-94-007-7672-2. DOI: 10.1007/978-94-007-7672-2_4.

[95] John L. Provis, Grant C. Lukey, and Jannie S. J. van Deventer. "Do Geopolymers Actually Contain Nanocrystalline Zeolites? A Reexamination of Existing Results." In: *Chemistry of Materials* 17.12 (June 2005), pp. 3075–3085. ISSN: 0897-4756. DOI: 10.1021/cm050230i.

[96] S. J. B. Reed. *Electron Microprobe Analysis and Scanning Electron Microscopy in Geology*. 2nd ed. Cambridge: Cambridge University Press, 2005. ISBN: 978-0-521-84875-6. DOI: 10.1017/CBO9780511610561.

[97] Nicolas Roussel, Anael Lemaître, Robert J. Flatt, and Philippe Coussot. "Steady State Flow of Cement Suspensions: A Micromechanical State of the Art." In: *Cement and Concrete Research* 40.1 (Jan. 2010), pp. 77–84. ISSN: 0008-8846. DOI: 10.1016/j.cemconres.2009.08.026.

[98] Gum Sung Ryu, Young Bok Lee, Kyung Taek Koh, and Young Soo Chung. "The Mechanical Properties of Fly Ash-Based Geopolymer Concrete with Alkaline Activators." In: *Construction and Building Materials* 47 (Oct. 2013), pp. 409–418. ISSN: 0950-0618. DOI: 10.1016/j.conbuildmat.2013.05.069.

[99] Prabir Kumar Sarker and Simon Mcbeath. "Fire Endurance of Steel Reinforced Fly Ash Geopolymer Concrete Elements." In: *Construction and Building Materials* 90 (Aug. 2015), pp. 91–98. ISSN: 0950-0618. DOI: 10.1016/j.conbuildmat.2015.04.054.

[100] W Wolfram Schmidt. "Design Concepts for the Robustness Improvement of Self-Compacting Concrete : Effects of Admixtures and Mixture Components on the Rheology and Early Hydration at Varying Temperatures." In: [object Object], 2014. DOI: 10.6100/IR771936.

[101] Wolfram Schmidt and Julian Link. "Rheological Properties." In: *Measuring Rheological Properties of Cement-based Materials: State-of-the-Art Report of the RILEM Technical Committee 266-MRP*. Ed. by Mohammed Sonebi and Dimitri Feys. RILEM State-of-the-Art Reports. Cham: Springer Nature Switzerland, 2024, pp. 7–31. ISBN: 978-3-031-36743-4. DOI: 10.1007/978-3-031-36743-4_2.

[102] Wolfram Schmidt, Christiane Weimann, and Luciana Weba. "Influences of of Hydration Effects on the Flow Phenomena of Concrete with Admixtures." In: Jan. 2016.

[103] Carsten Schwandt, James A. Hamilton, Derek J. Fray, and Ian A. Crawford. "The Production of Oxygen and Metal from Lunar Regolith." In: *Planetary and Space Science*. Scientific Preparations For Lunar Exploration 74.1 (Dec. 2012), pp. 49–56. ISSN: 0032-0633. DOI: 10.1016/j.pss.2012.06.011.

[104] Caijun Shi, Della Roy, and Pavel Krivenko. *Alkali-Activated Cements and Concretes*. London: CRC Press, Apr. 2014. ISBN: 978-0-429-18071-2. DOI: 10.1201/9781482266900.

[105] S. B. Simon, J. J. Papike, and J. C. Laul. "The Lunar Regolith: Comparative Studies of the Apollo and Luna Sites. Petrology of Soils from Apollo 17, Luna 16, 20, and 24." In: *Lunar and Planetary Science Conference Proceedings* 12 (Jan. 1982), pp. 371–388.

[106] Puyam S. Singh, Mark Trigg, Iko Burgar, and Timothy Bastow. "Geopolymer Formation Processes at Room Temperature Studied by 29Si and 27Al MAS-NMR." In: *Materials Science and Engineering: A* 396.1 (Apr. 2005), pp. 392–402. ISSN: 0921-5093. DOI: 10.1016/j.msea.2005.02.002.

[107] M. Sofi, J. S. J. van Deventer, P. A. Mendis, and G. C. Lukey. "Engineering Properties of Inorganic Polymer Concretes (IPCs)." In: *Cement and Concrete Research* 37.2 (Feb. 2007), pp. 251–257. ISSN: 0008-8846. DOI: 10.1016/j.cemconres.2006.10.008.

[108] Shani Sperinck, Paolo Raiteri, Nigel Marks, and Kate Wright. "Dehydroxylation of Kaolinite to Metakaolin—a Molecular Dynamics Study." In: *Journal of Materials Chemistry* 21.7 (Feb. 2011), pp. 2118–2125. ISSN: 1364-5501. DOI: 10.1039/C0JM01748E.

[109] M. Steveson and K. Sagoe-Crentsil. "Relationships between Composition, Structure and Strength of Inorganic Polymers." In: *Journal of Materials Science* 40.8 (Apr. 2005), pp. 2023–2036. ISSN: 1573-4803. DOI: 10.1007/s10853-005-1226-2.

[110] Peijiang Sun and Hwai-Chung Wu. "Chemical and Freeze–Thaw Resistance of Fly Ash-Based Inorganic Mortars." In: *Fuel* 111 (Sept. 2013), pp. 740–745. ISSN: 0016-2361. DOI: 10.1016/j.fuel.2013.04.070.

[111] G. Jeffrey Taylor, Linda M. V. Martel, Paul G. Lucey, Jeffrey J. Gillis-Davis, David F. Blake, and Philippe Sarrazin. "Modal Analyses of Lunar Soils by Quantitative X-ray Diffraction Analysis." In: *Geochimica et Cosmochimica Acta* 266 (Dec. 2019), pp. 17–28. ISSN: 0016-7037. DOI: 10.1016/j.gca.2019.07.046.

[112] Lawrence A. Taylor and Thomas T. Meek. "Microwave Sintering of Lunar Soil: Properties, Theory, and Practice." In: *Journal of Aerospace Engineering* 18.3 (July 2005), pp. 188–196. ISSN: 0893-1321. DOI: 10.1061/(ASCE)0893-1321(2005)18:3(188).

[113] "The Principles of Diffraction Analysis." In: *Industrial Applications of X-Ray Diffraction*. CRC Press, 1999. ISBN: 978-0-429-17771-2.

[114] Louise K. Turner and Frank G. Collins. "Carbon Dioxide Equivalent (CO2-e) Emissions: A Comparison between Geopolymer and OPC Cement Concrete." In: *Construction and Building Materials* 43 (June 2013), pp. 125–130. ISSN: 0950-0618. DOI: 10.1016/j.conbuildmat.2013.01.023.

[115] J. G. S. VAN JAARSVELD, J. S. J. VAN DEVENTER, and G. C. LUKEY. "A Comparative Study of Kaolinite Versus Metakaolinite in Fly Ash Based Geopolymers Containing Immobilized Metals." In: *Chemical Engineering Communications* 191.4 (Apr. 2004), pp. 531–549. ISSN: 0098-6445. DOI: 10.1080/00986440490277974.

[116] Kai-tuo Wang, Patrick N Lemougna, Qing Tang, Wei Li, and Xue-min Cui. "Lunar Regolith Can Allow the Synthesis of Cement Materials with Near-Zero Water Consumption." In: *Gondwana Research* 44 (Apr. 2017), pp. 1–6. ISSN: 1342-937X. DOI: 10.1016/j.gr.2016.11.001.

[117] Jing Wei, Jiesheng Liu, Tongtong Zhang, Bowen Feng, Yaohua Chen, Yidi Zhang, Wanwan Fu, and Xiaoming Tan. "Effect of Metakaolin Content and Water/Binder Ratio on Strength and Durability Properties of Modified Cement Mortar." In: *Journal of Testing and Evaluation* 51.2 (Mar. 2023), pp. 1166–1180. ISSN: 0090-3973. DOI: 10.1520/JTE20220217.

[118] Yong Gen Wu, Liang Cai Cai, and Ya Wei Fu. "Durability of Green High Performance Alkali-Activated Slag Pavement Concrete." In: *Applied Mechanics and Materials* 99–100 (2011), pp. 158–161. ISSN: 1662-7482. DOI: 10.4028/www.scientific.net/AMM.99-100.158.

[119] Long Xiao, Yuqi Qian, Qian Wang, and Qiong Wang. "CHAPTER 9 - The Chang'e-5 Mission." In: *Sample Return Missions*. Ed. by Andrea Longobardo. Elsevier, Jan. 2021, pp. 195–206. ISBN: 978-0-12-818330-4. DOI: 10.1016/B978-0-12-818330-4.00009-4.

[120] Guiyan Xiong, Xiaolu Guo, Shuting Yuan, Ming Xia, and Zhihao Wang. "The Mechanical and Structural Properties of Lunar Regolith Simulant Based Geopolymer under Extreme Temperature Environment on the Moon through Experimental and Simulation Methods." In: *Construction and Building Materials* 325 (Mar. 2022), p. 126679. ISSN: 0950-0618. DOI: 10.1016/j.conbuildmat.2022.126679.

[121] Ammar Yahia and Arnaud Perrot. "Measuring Procedures." In: *Measuring Rheological Properties of Cement-based Materials: State-of-the-Art Report of the RILEM Technical Committee 266-MRP*. Ed. by Mohammed Sonebi and Dimitri Feys. RILEM State-of-the-Art Reports. Cham: Springer Nature Switzerland, 2024, pp. 73–95. ISBN: 978-3-031-36743-4. DOI: 10.1007/978-3-031-36743-4_4.

[122] Bo Zhang, Kenneth J. D. MacKenzie, and Ian W. M. Brown. "Crystalline Phase Formation in Metakaolinite Geopolymers Activated with NaOH and Sodium Silicate." In: *Journal of Materials Science* 44.17 (Sept. 2009), pp. 4668–4676. ISSN: 1573-4803. DOI: 10.1007/s10853-009-3715-1.

[123] Yu Zhang, Tao Li, Dongshuai Hou, Jinglin Zhang, and Jinyang Jiang. "Insights on Magnesium and Sulfate Ions' Adsorption on the Surface of Sodium Alumino-Silicate Hydrate (NASH) Gel: A Molecular Dynamics Study." In: *Physical Chemistry Chemical Physics* 20.27 (July 2018), pp. 18297–18310. ISSN: 1463-9084. DOI: 10.1039/C8CP02469C.

[124] Qingyu Zhong, Xiang Tian, Guolun Xie, Xi Luo, and Hui Peng. "Investigation of Setting Time and Microstructural and Mechanical Properties of MK/GGBFS-Blended Geopolymer Pastes." In: *Materials* 15.23 (Dec. 2022). DOI: 10.3390/ma15238431.

[125] Siqi Zhou, Chenghong Lu, Xingyi Zhu, and Feng Li. "Preparation and Characterization of High-Strength Geopolymer Based on BH-1 Lunar Soil Simulant with Low Alkali Content." In: *Engineering* 7.11 (Nov. 2021), pp. 1631–1645. ISSN: 2095-8099. DOI: 10.1016/j.eng.2020.10.016.

[126] Keqing Zong et al. "Bulk Compositions of the Chang'E-5 Lunar Soil: Insights into Chemical Homogeneity, Exotic Addition, and Origin of Landing Site Basalts." In: *Geochimica et Cosmochimica Acta* 335 (Oct. 2022), pp. 284–296. ISSN: 0016-7037. DOI: 10.1016/j.gca.2022.06.037.

[127] F. de Larrard, C. F. Ferraris, and T. Sedran. "Fresh Concrete: A Herschel-Bulkley Material." In: *Materials and Structures* 31.7 (Aug. 1998), pp. 494–498. ISSN: 1871-6873. DOI: 10.1007/BF02480474.